# InGaAs-AlAs and InGaAs-InGaP Strain-Compensated Heterostructures for Short-Wavelength Intersubband Transitions and Lasers

Dissertation
zur Erlangung des akademischen Grades
doctor rerum naturalium
(Dr. rer. nat.)
im Fach Physik
eingereicht an der
Mathematisch-Naturwissenschaftlichen Fakultät I
der Humboldt-Universität zu Berlin
von
**Diplom-Physiker Mykhaylo Semtsiv**
geboren am 01.04.1973 in Laskiwzi (Ukraine)

Präsident der Humboldt-Universität zu Berlin
Prof. Dr. J. Mlynek

Dekan der Mathematisch-Naturwissenschaftlichen Fakultät I
Prof. Thomas Buckhout PhD

Gutachterinnen und Gutachter:
1. Prof. Dr. K. Ploog
2. Prof. Dr. W. T. Masselink
3. Prof. Dr. C. Gmachl

Tag der mündlichen Prüfung: 08. September 2004

# InGaAs-AlAs and InGaAs-InGaP Strain-Compensated Heterostructures for Short-Wavelength Intersubband Transitions and Lasers

Mykhaylo Semtsiv

September 21, 2004

# Contents

# Zusammenfassung

Der Quantenkaskadenlaser (QCL) ist ein unipolares Intersubbandbauelement dessen Funktionsweise auf Übergängen zwischen dem ersten angeregten Zustand und dem Grundzustand in einem Quantentopf (quantum well, QW) beruht. Er wurde im Jahre 1974 von Kazarinov und Suris theoretisch vorhergesagt (1) und erstmals 1994 von Faist *et al.* experimentell realisiert (2). Das Elektron verlässt nach dem Laserübergang nicht das Leitungsband und kann somit durch ein angelegtes elektrisches Feld in die nächste aktive Zone transferiert werden, wo es wiederum einem Laserübergang untergehen kann. Schliesslich, nach einer Reihe solcher Kaskadenprozesse, emittiert ein einzelnes Elektron viele Photonen; dies definiert die hohe Quanteneffizienz der QCLs.

Das Hauptproblem bei der kaskadierten Benutzung von aktiven Regionen ist ein schneller Elektronentransport zwischen den emittierenden QWs mithilfe des sogenannten Injektors. Ein schneller Transport der Ladungsträger ist notwendig um das obere Laserniveau zu populieren und das untere zu depopulieren, womit die für die stimulierte Emission notwendige Besetzungsinversion erreicht werden kann. Zur Gewährleistung des schnellen Transports im Injektor ist die Verwendung von Materialien mit einer geringen effektiven Masse naheliegend. Unter den technologisch wichtigen III-V Verbindungen besitzt InAs die geringste elektronische effektive Masse von $0.023m_0$ (wobei $m_0$ die Masse des freien Elektrons ist). Die binäre Verbindung mit der nächst grösseren effektiven Masse ist GaAs mit $m_e^*$=$0.067m_0$. Bisher wurden QCLs in beiden, InAs und GaAs und weiterhin im ternären InGaAs basierten QW Materialsystem realisiert (2; 3; 4). Gegenwärtig zeigen QCLs einen hohen Grad der Reife; hohe Lichtleistung, Dauerstrichbetrieb und Betrieb bei Raumtemperatur sowie Oberflächenemission wurden erzielt. Der von den QCLs abgedeckte spektrale Bereich erstreckt sich von 3.5 $\mu$m bis zu 87 $\mu$m (5; 6).

Trotz des hohen Reifegrades ist der Quantenkaskadenlaser immernoch in der Entwicklung. Speziell die Erweiterung des spektralen Bereichs ist für viele Anwendungen essentiell. Enorme Fortschritte bei der Erweiterung hin zu grösseren Wellenlängen wurden in den letzten Jahren erzielt, dennoch ist der kurzwellige Rekord von 3.5 $\mu$m aus dem Jahre

1998 (5) bisher ungebrochen. Nichtsdestotrotz besitzt der QCL auch im nahen Infrarot das Potential den konventionellen Interbandlaser zu übertreffen. Neben dem Wettstreit um Schwellströme und Ausgangsleistungen, ist aufgrund der andersartigen Physik des Laserüberganges eine verbesserte Anwendungsmöglichkeit im Bereich des schnellen optischen Schaltens zu erwarten.

Die Herausforderung im Bereich der kurzwelligen QCLs liegt in der beschränkten Leitungsbanddiskontinuität (CBO) zwischen Quantentopf- und Quantenbarrierenmaterial. Um zwei gebundene elektronische Eigenzustände innerhalb der Quantentöpfe der aktiven Zone zu gewährleisten, wird eine grosse Leitungsbanddiskontinuität benötigt. Weiterhin kann nur so eine ausreichend hohe Barriere zwischen den angeregten Zuständen und dem klassischen Zustandskontinuum bei angelegtem elektrischen Feld erreicht werden. Neben der Notwendigkeit des grossen CBO sollte das Barrierenmaterial eine direkte Bandlücke aufweisen oder zumindest der angeregte Zustand in der aktiven Zone unterhalb des niedrigsten Leitungsbandes des Barrierenmaterials liegen. Mit der Einschränkung bezüglich der Gitterkonstanten von Quantentopf und -barrierenmaterial für ein kohärentes Wachstum auf einem bestimmten Substrat, endet man bei nur einer Hand voll vielversprechender Materialkombinationen für die Anwendung in QCLs. Das grösste CBO für Materialien mit direkter Bandlücke findet man bei InGaAs/InAlAs. Wir erzielen 520 meV für die ternäre an InP gitterangepasste und 740 meV für die spannungskompensierte $In_{0.70}Ga_{0.30}As/In_{0.40}Al_{0.60}As$ Kombination. Unter den Barrierenmaterialien mit indirekter Bandlücke ist die Kombination InAs/AlSb auf GaSb oder InAs mit 2.1 eV CBO im $\Gamma$-valley (7) sehr vielversprechend. Quantenkaskadenlaser basierend auf diesem Materialsystem mit Emission bei 10 $\mu$m wurden kürzlich von Ohtani and Ohno (4; 8) realisiert. Jedoch wurde im kurzwelligen Bereich um 4 und 3 $\mu$m in diesem System bisher nur spontane Emission (9) beobachtet. Damit ist es bis heute ein offene Frage, welches Materialsystem tatsächlich das geeignetste für die Anwendung in kurzwelligen QCLs sein wird und ob es überhaupt möglich sein wird, ihren Wellenlängenbereich auf die Telekommunikationswellenlänge von 1.55 $\mu$m auszuweiten, was zweifellos die grösste Herausforderung darstellt.

Oberflächenemission von QCLs ist bisher mittels der Aufbringung einer Rippenstruktur mit kurzer Periode auf der Oberfläche der Laserstreifen erreicht worden (10; 11). Die Möglichkeit einer Polarisation in der Fläche mithilfe selbstorganisierter Quantenpunktstrukturen innerhalb der aktiven Zone ist ein aktuelles Thema innerhalb der QCL-Gemeinschaft, aber bisher noch unerreicht. Die Kombination aus feldinduzierten Minibändern aus elektronischen Zuständen in konventionellen QCLs und diskreten atomartigen Zuständen in Quantenpunkten ist eine kreative und gleichzeitig widersprüchliche Idee. Dennoch vereint dieses Thema ein gewaltiges Interesse sowohl von theoretischer als auch experimenteller Seite innerhalb der QCL-Gemeinschaft (12; 13).

Diese Arbeit ist der Erweiterung der Materialvielfalt für die Herstellung von Quantenkaskadenlasern gewidmet. Die Mission dieser Forschungsarbeit ist

- die Grenzen im Gebrauch des spannungskompensierten Designs des klassischen InGaAs/InAlAs Materialsystems auf InP für kurzwellige Emission auszuloten;

- die Möglichkeiten kurzwelliger Intersubbandemission in einer der extraordinären Materialkombinationen für die QCL-Anwendung zu erforschen: spannungskompensiertes InGaAs/InGaP auf GaAs;

Die Quintessenz der gesamten Forschungsarbeit besteht in der spannungskompensierten Herangehensweise und den InGaAs enthaltenden Materialsystemen für die Anwendung in Quantenkaskadenlasern. Die Arbeit ist wie folgt strukturiert:

**Kapitel 1** Die vorliegende Einführung.

**Kapitel 2** Kurzer Überblick der Eigenschaften von Intersubbandübergängen und der Grundlagen der QCL-Funktionsweise. In diesem Kapitel wird eine Einführung in die Eigenschaften von Intersubbandübergängen und den Minibandtransport gegeben. Dieses Kapitel unterstreicht den physikalischen Unterschied von Intersubbandübergängen und Transport zum Fall der Interbandübergnge und gibt eine Einführung in die vorteilhaften Eigenschaften der Intersubbandbauelemente. Weiterhin wird eine Einführung in die Physik des Quantenkaskadenlasers und eine Übersicht der Designvielfalt der aktiven Zone gegeben. Im Speziellen wird auf die unterschiedlichen Strategien bei der Erzielung der Besetzungsinversion eingegangen.

**Kapitel 3** Experimentelles Kapitel. Das 3. Kapitel fasst die erzielten eigenen Ergebnisse innerhalb des InGaAs/InAlAs Materialsystems auf InP zusammen. Dabei konzentriert es sich auf extreme Fälle des spannungskompensierten Designs welche die Realisierung kurzwelliger Übergänge zum Ziel haben.

**Kapitel 4** Experimentelles Kapitel. Im 4. Kapitel werden die erzielten eigenen Ergebnisse innerhalb des InGaAs/InGaP Materialsystems dargestellt. Das InGaAs/InGaP Materialsystem auf GaAs wurde unseres Wissens zuvor füür Intersubbandbauelemente weder benutzt noch vorgeschlagen. Das Kapitel beschreibt den gesamten Verlauf, beginnend mit dem Probenwachstum über grundlegende Materialstudien, bis hin zum Design der QC-Teststruktur und deren Fabrikation.

**Kapitel 5** Hierin wird die Zusammenfassung der erzielten eigenen Ergebnisse und daraus resultierenden Schlussfolgerungen gegeben.

# Chapter 1

# Introduction

Quantum cascade lasers, QCL, are unipolar intersubband devices, which work on transitions between the first excited and the ground state in quantum wells, QW. They where predicted theoretically by Kazarinov and Suris (1) 1974, and realized experimentally for the first time by Faist *et al.* (2) 1994. Electron does not leave the conduction band after the lasing transition in QCL. And therefore it can be used again in the next active region, where it can be transferred due to applied electric field. Finally, after a number of such cascade processes, single electron emits many photons, which defines a high quantum efficiency of QCLs.

The key issue in use of cascaded active regions is a fast electron transport in between the emitting QWs (so called, injector region). Fast carrier transfer is needed on the one hand to effectively populate the upper lasing state in active region QW and on the other hand to quickly depopulate the lower lasing state. So that population inversion, necessary for stimulated emission, is achieved. To provide the fast transport in injector region it is likely to deal with materials with a low effective mass. Among the variety of technologically important III-V compounds InAs has the lowest electron effective mass of $0.023m_0$ (where $m_0$ is the free electron mass). Next low effective mass binary material after InAs is GaAs with $m_e^*$=$0.067m_0$. Up to now QCLs are realized on both, InAs- and GaAs- as well as ternary InGaAs-based-QW material systems (2; 3; 4). Currently QCLs show a high level of maturity. High power, cw-operation and room temperature operation as well as surface emission are achieved. Spectral range, covered by QCLs, extends from 3.5 $\mu$m up to 87 $\mu$m (5; 6).

Despite of the high level of maturity, QCLs are still under development. In particular, extension of the spectral range of operation is likely for many applications. Tremendous progress was achieved last years in long wavelength range extension of QCLs. However, the short wavelength record of 3.5 $\mu$m has not been beaten since 1998 (5). Nevertheless, QCLs has a potential to outperform conventional interband lasers also in near infrared spectral range. Apart from competition in threshold current densities and output power, QCLs are expected to be better in fast optical switching operation due to different physics of lasing transitions.

The challenge of short wavelength QCLs is a limited conduction band edge offset, CBO, between the quantum well and barrier material. High CBO is needed to confine two quantized electron states in active region QW and to provide sufficient barrier between the excited state and classical continuum of states above the barrier material conduction band edge under applied electric field. More over, despite of high CBO demand, barrier should be the direct band gap material, or at least, the upper lasing state in active region should lay below the lowest conduction band valley in the barrier material. Together with restriction on the lattice constant of both, well and barrier materials, for coherent growth on a certain substrate, we end up with very few promising material combinations for QCL application. The highest CBO for direct band gap materials combination we find in InGaAs/InAlAs. We obtain 520 meV for lattice matched to InP ternaries and about 740 meV for strain-compensated $In_{0.70}Ga_{0.30}As/In_{0.40}Al_{0.60}As$ combination. Among the indirect barrier material combinations, very promising is InAs/AlSb on GaSb or InAs with 2.1 eV CBO in Γ-valley (7). QCL emitting at 10 $\mu$m has been recently realized on this material system by Ohtani and Ohno (4; 8). However, at short wavelength, 4 and 3 $\mu$m, only spontaneous emission is obtained (9) in this material system up to now experimentally. So up to now, it is still an open question, which material system is going to be most suitable for short wavelength QCL application. And it is still an open question, if it is possible at all to extend the operation wavelength of QCLs to the most challenging 1.55 $\mu$m telecommunication wavelength.

Surface emission is achieved in QCLs up to now by manufacturing of the short period grating on the top of the planar laser strip (10; 11). The possibility of in-plane polarized emission involving self organized quantum dot structures into the QCL active region is a hot topic in QCL community, but it is not achieved experimentally up to now. Combining the field induced minibands of electron states in conventional QCLs together with discrete atom-like states in QDs is a creative and at the same time contradictive idea. Nevertheless, this topic attracts a huge interest from both, theoretical and experimental, side of QCL community (12; 13).

This work is dedicated to make a step forward in extension of material variety used for QCL fabrication. The mission of this research is

- to find out the limits of use of strain-compensated designs on classical InGaAs/InAlAs material system on InP to achieve the short wavelength generation;

- to discover the possibilities of short wavelength intersubband generation in one of extraordinary material combinations for QCL application: strain-compensated InGaAs/InGaP on GaAs;

The bottom line of the whole research is strain compensation approach and InGaAs containing material systems for QCL application.

Present work consist of:

**Chapter 1** The current introduction.

**Chapter 2** Brief overview of intersubband transitions properties and the basics of QCL action. In the overview-chapter an introduction into the properties of intersubband transitions and miniband transport is given. This chapter underlines the difference in physics of intersubband transitions and transport comparing to the case of interband transitions; and gives an introduction into the advantageous properties of intersubband devices. This chapter gives an introduction into the quantum cascade laser physics and overview on variety of active region designs. This chapter is, specially, dedicated to point out different ways of achieving the population inversion in each QCL active region approach.

**Chapter 3** Experimental chapter. Third chapter describes obtained original results on InGaAs/InAlAs material system on InP during the present work. It concentrates on extreme cases of strain-compensated designs for achieving the short wavelength transitions.

**Chapter 4** Experimental chapter. Forth chapter describes obtained original results on InGaAs/InGaP material system. InGaAs/InGaP material system on GaAs was never before, up to our knowledge, proposed or used for intersubband devices. So, the chapter describes all the way from the sample growth issues and basic study of this material up to QC test-structure design and fabrication.

**Chapter 5** Here, the summary of obtained original results and conclusions are given.

# Chapter 2

# Introduction into physics of intersubband devices

## 2.1 Theoretical modelling of intersubband transitions in semiconductor quantum wells

### 2.1.1 Envelope function approximation

Semiconductor crystal can be imagined as a set of ions located in the periodically arranged sites. In order to describe an electron within the semiconductor, let us represent the crystal by the periodical potential $V(\mathbf{r})$. Then following Bloch (14), the electron states $f$ in spatially periodic potential $V(\mathbf{r})$ can be written as

$$f_{n,\mathbf{k}}(\mathbf{r}) = e^{i\mathbf{k}\cdot\mathbf{r}} U_{n,\mathbf{k}}(\mathbf{r}), \tag{2.1}$$

where $U_{n,\mathbf{k}}(\mathbf{r})$ retains the periodicity of the potential. The index $n$ is denoted as the band index, and the associated collection of energy eigenvalues $E_n(\mathbf{k})$ is referred to as the band structure of the material ($\mathbf{k}$ is the wavevector). The calculation of these eigenvalues is greatly simplified by looking for the solutions of the form of Bloch functions 2.1. The band structure determines the density of states in material, and the wave functions play a part in determining the strength of various scattering processes. Any quantum mechanical study of solids must begin with the band structure, and in principle, any material property can be calculated directly from the bands. Many methods of varying complexity are used to calculate the energies and wave functions of solids. Fortunately, we do not generally need the band structure for all values of k in the Brillouin zone. Most of the electronic and optical properties of direct gap type I semiconductor heterostructures are determined by the conduction and valence band edges. Hence, to calculate these properties we require only the band structure for small values of $\mathbf{k}$ near $\mathbf{k} = 0$. Once the bulk band structure has been obtained, the effect of strain, free carriers, electric field, and heterointerfaces can be additionally included within the effective mass approximation. The effective mass equation (or envelope function approximation) was first suggested by Wannier (15) and elaborated by Slater (16). It forms the foundation for much of semiconductor and device analysis. Later, a rigorous verification of the equation and its extension to multiple bands was given by Luttinger and Kohn (17). A particular readable account, directed toward heterostructure application, was done by Bastard (18; 19; 20). The approach, which is rather general, allows one to treat easily the problem of a crystal in a slowly varying "external" potential $V_{ext}(\mathbf{r})$. Instead of solving the total Hamiltonian, including the ion cores, the valence and core electrons, and the external potential, we can solve a reduced Hamiltonian that includes only the band structure $E_n(\mathbf{k})$ and the external potential. The most common example occurs when only a single nondegenerate band $n$, such as the conduction band in the most of III-V compounds, is considered. In this case, the wave function can be expressed as

$$f(\mathbf{r}) = F(\mathbf{r})U_{n,0}(\mathbf{r}), \tag{2.2}$$

where the envelope function $F(\mathbf{r})$ and the energy eigenvalue $E$ satisfy the effective mass equation:

$$[E_n(-i\nabla) + V_{ext}(\mathbf{r})]F(\mathbf{r}) = EF(\mathbf{r}). \tag{2.3}$$

Here $E_n(-i\nabla)$ is obtained by evaluating at $\mathbf{k} = -i\nabla$ the second-order Taylor polynomial in $\mathbf{k}$ of $E_n(\mathbf{k})$. Note that the periodic potential has disappeared, and we are left with only the external potential $V_{ext}(\mathbf{r})$. Of course, the information on the lattice structure has been incorporated via the kinetic term $E_n(-i\nabla)$. It is also important to remember that the full wave function is given by equation 2.2, the product of the envelope function and the zone center Bloch function. The simplest case of eq. 2.3 occurs when there is no external potential and the band is spherical; that is,

$$E_n(\mathbf{k}) = \frac{\hbar^2 k^2}{2m_e}. \tag{2.4}$$

In this case the effective mass equation reduces to the Schrödinger equation for the free particle,

$$-\frac{\hbar^2}{2m_e}\nabla^2 F(\mathbf{r}) = EF(\mathbf{r}), \tag{2.5}$$

With the familiar solution

$$F(\mathbf{r}) = e^{i\mathbf{kr}}, \tag{2.6}$$

$$E(\mathbf{k}) = \frac{\hbar^2 \mathbf{k}^2}{2m_e}. \tag{2.7}$$

Hence, the conduction band electron is described like a free particle with an "effective mass" $m_e$ given by

$$\frac{\hbar^2}{m_e} = \frac{\partial^2 E_n(0)}{\partial k^2} \tag{2.8}$$

The effective mass $m_e$ appears in an equation that is mathematically identical to the Schrödinger equation for a spinless particle in a scalar potential. It is the best to think of $m_e$ as a material property. The effective mass simplifies the problem of electron motion in a periodic potential of ion cores. Naturally, such an approximation will break down when the wavelength of the particle (photon or electron) is on the scale of atomic fluctuations (X-ray diffraction, short-wavelength electrons). Fortunately, in direct band gap III-V semiconductors most of the carriers reside in the low-energy band-edge states. And these are represented quite well by the effective mass theory. This is the justification for applying many of the formulas derived for the quantum mechanics of free particles directly to the conduction band electrons by making the simple replacement of the free electron mass $m_0$ by the effective conduction band electron mass $m_e$.

### 2.1.2 Conduction band states in quantum wells

Now we proceed to the quantum well case. Modern epitaxial techniques permit us to fabricate structures with extremely sharp interfaces. Because the composition of each monolayer can be controlled, it is possible to grow materials of widely different bandgaps (classical example is GaAs and $\mathrm{Al}_x\mathrm{Ga}_{1-x}\mathrm{As}$) next to each other, thus creating the so-called heterostructure. This produces a very sharp band gap discontinuity and dramatically affects the carrier behavior. One of the most interesting heterostructures to study is the quantum well, in which a thin layer (or well) of a narrow band gap material is sandwiched between two thicker layers (or barriers) of a wider band gap material (see fig. 2.1). If the well width is less than the de Broglie wavelength of the carriers in the well material ( 10 nm in most III-V compounds), the carrier is "quantum" confined. The envelope wave function $F(z)$, and so the full wave function $f(z)$ are mostly localized in material $A$ (see fig. 2.2) and do not propagate along the $Z$-axis. Such structures should properly be regarded as completely new materials, with properties wholly distinct from either well or barrier bulk materials. Because the well width is smaller than the wavelength of the carrier, quantum wells are not truly tree-dimensional structures,

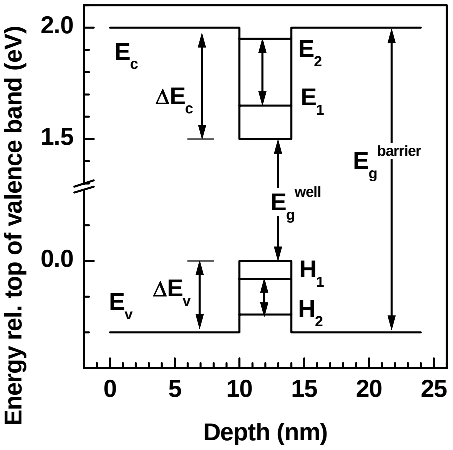

Figure 2.1: Quantum confined states, subbands, of electrons, $E_1$ and $E_2$, and holes $H_1$ and $H_2$ in 4 nm thick quantum well in energy-real space coordinates.

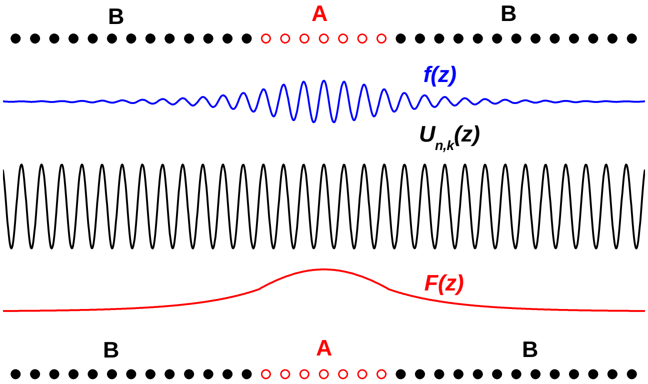

Figure 2.2: Illustration of the wave function localization in a quantum well. $F(z)$ is the $z$-direction localized envelope function. $f(z)$ is the full wave function in QW. $U_{n,k}(z)$ represents Bloch function. Lattice constant of materials $A$ and $B$ assumed to be the same.

but are instead quasi-two-dimensional. The change in the dimensionality of the system results in dramatic variation in many of the material properties of these structures (such as carrier masses, bandgaps, densities of states) and even suggests device concepts that are not possible with simple bulk materials (QWIPs, QCLs, so on). The band structure of these quantum wells may easily be addressed within the effective mass equation. If we take the $z$-axis to be the growth direction, assuming that the material composition will vary in the $z$ direction but will be uniform in the $x - y$ plane, we can again use eq. 2.3, but we must allow the band structure $E_n(k)$ to be dependent on $z$ as well. Taking the arbitrary reference for $E_n(k) = 0$, we can compose two materials $A$ and $B$ with different dispersion relations and form a quantum well of width $L$ by arranging them as

$$E_n(k) = E_A(k) = E_A + \frac{\hbar^2 k^2}{2m_A} \quad at \quad |z| < \frac{L}{2}, \tag{2.9}$$

$$E_n(k) = E_B(k) = E_B + \frac{\hbar^2 k^2}{2m_B} \quad at \quad |z| > \frac{L}{2}. \tag{2.10}$$

Thus, when $E_A < E_B$ the electrons see an effective z-dependent "potential" well given by

$$V_0(z) = E_A \qquad at \qquad |z| < \frac{L}{2}, \quad and \tag{2.11}$$

$$V_0(z) = E_B \qquad at \qquad |z| > \frac{L}{2}. \tag{2.12}$$

Let us address now the issue of interpretation of the kinetic energy operator $E(-i\nabla)$ when the material parameters, and hence the band structure $E_n(k)$, depend on $z$. The problem arises because $\frac{d}{dz}$ and $\frac{1}{m(z)}$ do not commute; hence, the ordering is important. Generally, for a single spherical band, the order is taken as

$$E_n(-i\nabla, z) \rightarrow -h2\nabla \cdot \left[\frac{1}{2m_e(z)}\nabla\right]. \tag{2.13}$$

It must be admitted that this operator cannot be derived, but this is the preferred quadratic form for a number of reasons. First, the operator is Hermitian, which ensures real energy eigenvalues and conservation of probability for the envelope functions. Second, the operator conserves the probability current across the heterointerface, as can be seen by examining the form of the current operator (21). Thomsen *et al.* (22) and Morrow (23) have shown, that this is the only physically acceptable quadratic form for a kinetic energy operator with spatially varying mass under very general conditions. Hence, we assume that eq. 2.13 and the effective mass equation for electrons in a quantum well reduces to

$$\left[-\frac{\hbar^2}{2m_e(z)}\left(\frac{d^2}{dx^2}+\frac{d^2}{dy^2}\right)-\frac{\hbar^2}{2}\frac{d}{dz}\frac{1}{m_e(z)}\frac{d}{dz}+V_0(z)\right]F(r)=EF(r). \tag{2.14}$$

This can be solved in the usual manner; that is,

$$F(r)=1/\sqrt{A}e^{i(k_x x+k_y y)}f_m(k_{||},z), \tag{2.15}$$

where $f_m(k_{||},z)$ satisfies

$$\left[-\frac{\hbar^2}{2}\frac{d}{dz}\frac{1}{m_e(z)}\frac{d}{dz}+V_0(z)+\frac{\hbar^2 k_{||}^2}{2m_e(z)}\right]f_m(k_{||},z)=E_m(k_{||})f_m(k_{||},z), \tag{2.16}$$

where $\hat{k}_{||}\equiv\hat{k}_x+\hat{k}_y$, $m$ is a subband index (see Fig. 2.1), and $A$ is an arbitrary normalization area. Note that the spatially dependent electron mass introduces a $k_{||}$-dependent potential term, so that the in-plane and perpendicular motions are not entirely decoupled. This introduces nonparabolicity to the conduction subbands that broadens the intersubband absorption spectrum. If this effect is ignored, eq. 2.16 becomes the Schrödinger equation for a particle in a finite square well with varying mass. Such an equation can be solved by the usual method of matching solutions in each region with the appropriate current conserving boundary conditions. Some examples of this technique can be found in any textbook on quantum mechanics. Of course, this technique works only when the solutions are known in each region, restricting its application to square quantum wells, perhaps with applied electric fields.

When a substantial number of free carriers are present in the well, they will induce band bending. In this case, the effective mass equation will not take the simple form 2.16, but will contain a space-charge potential. If the analytic solutions in each region are not known, one needs to employ numerical calculation techniques.

### 2.1.3 Conduction band states in quantum well superlattices

Let us consider a sequence of the same quantum wells (material $A$, thickness $l_A$, lattice constant $a_A$) spaced by the equal quantum barriers (material $B$, thickness $l_B$, lattice constant $a_B$=$a_A$). Such a heterostructure reveals an additional to the elemental crystalline cell of a bulk material periodicity along the growth direction $z$. Since that, the size of an elemental cell in such a heterostructure along $z$ is not an $a_B$ anymore, but $d\equiv l_A+l_B$. In another words, such a heterostructure becomes to

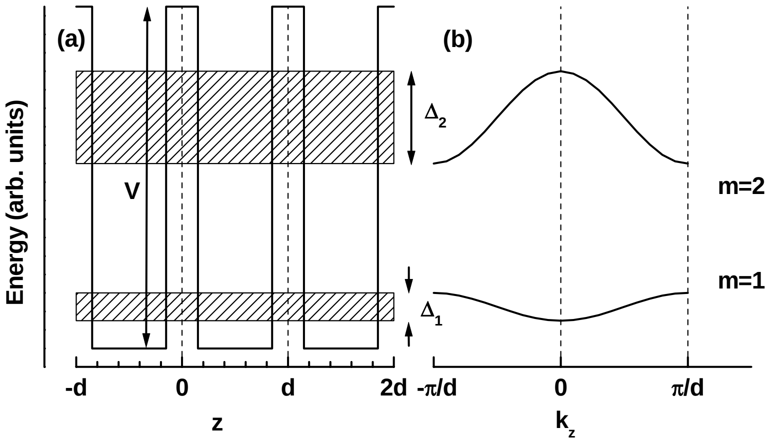

Figure 2.3: Miniband structure of a superlattice in energy–real space coordinates (a) and energy–$k$-space (b).

be an artificial anisotropic crystal. The size of elemental cell of such a superlattice can vary from the infinity down to $a_B$ scale. In the upper limit case, we will basically deal with the macroscopic pieces of individual materials, attached to each other, where each of them reveals individual three-dimensional properties. In the lower limit case we obtain a homogeneous alloy of materials A and B with isotropic three-dimensional properties. Highly anisotropic properties of a superlattice one obtains when the period $d$ is on the scale of the de Broglie wavelength in individual materials. Particular properties of energy bands of such short period superlattices we are going to consider in current subsection.

To describe qualitatively the new specific features of superlattices, let us ignore the spatial dependence of effective mass $m_e(z)$ in the effective mass equation 2.14, and consider the Schrödinger equation for the envelope function $F(r)$

$$[-\frac{\hbar^2}{2m_e}(\frac{d^2}{dx^2}+\frac{d^2}{dy^2}+\frac{d^2}{dz^2})+V_{SL}(z)]F(r)=EF(r), \qquad (2.17)$$

where $V_{SL}(z)$ is the periodic superlattice confinement potential, as depicted on fig. 2.3a. We consider a space independent effective mass separately for well and for barrier material. The lateral and perpendicular motions of electron in such a case are decoupled. And one looks for solution in simplified form of eq. 2.15:

$$F(r)=\frac{1}{\sqrt{A}}e^{i(k_x x+k_y y)}f_m(z). \qquad (2.18)$$

Let us consider a single electronic band and, hence, ignore the index $m$. Applying the periodical Bastard's boundary conditions (19) on the heterointerfaces

$$f(A,z) = f(B,z+jd), \qquad j = 0, \pm1, \pm2, \dots \tag{2.19}$$

$$\frac{1}{m_A}\frac{d}{dz}f(A,z) = \frac{1}{m_B}\frac{d}{dz}f(B,z+jd), \qquad j = 0, \pm1, \pm2, \dots \tag{2.20}$$

one obtains the transcendental equation

$$\cos(k_z d) = \cos(k_A l_A)\cos(k_B l_B) - \frac{1}{2}(t + \frac{1}{t})\sin(k_A l_A)\sin(k_B l_B) \tag{2.21}$$

where

$$k_A^2 = \frac{2m_A E}{\hbar^2} - k_x^2 - k_y^2, \tag{2.22}$$

$$k_B^2 = \frac{2m_B(E-V)}{\hbar^2} - k_x^2 - k_y^2, and \tag{2.23}$$

$$t = \frac{m_A k_B}{m_B k_A} \tag{2.24}$$

The resulting band structure $E_n(k_z)$, which is a solution of eq. 2.21, is called minibands. In contrast, purely two-dimensional quantum confined states are usually called subbands. The crucial quantity distinguishing two-dimensional subband from three-dimensional minibands behavior is the ratio of minibands width to the strength of some broadening mechanisms such as scattering rate or potential fluctuations. If this broadening is larger than the minibands width, the electrons do not feel the miniband dispersion and are effectively confined in $z$ direction. Figure 2.3 shows schematically a superlattice band structure in real space and in k-space. Figure 2.4 shows the density of states, DOS, in minibands. The DOS does not have the real gap, but takes the constant value $m/\pi\hbar^2$ between the minibands. It is useful to have an explicit expression for the superlattice energy dispersion. This is available through the tight binding model, where one starts with the energy levels of separated quantum wells and takes into account the interaction with the nearest neighbouring wells, leading to

$$E_n(k) = E_n \pm \frac{\Delta_n}{2}\cos(k_z d) + \frac{\hbar^2(k_x^2 + k_y^2)}{2m}. \tag{2.25}$$

Here $E_n$ and $\Delta_n$ are the middle and the width respectively of the $n$-th miniband ($n \geq 1$). The minus sign in eq. 2.25 holds for odd minibands, the plus sign is for even ones. The effective mass for the in-plane motion is assumed to be identical to the mass in the well, since the electrons have a much higher probability amplitude there than in the barriers. Equation 2.25 can also be obtained by expanding eq. 2.22, 2.23 and 2.24 in the vicinity of the quantum well energy levels (24).

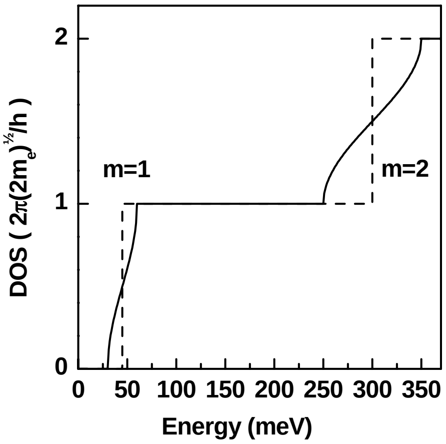

Figure 2.4: DOS for SL minibands (solid line) comparing the DOS of the same thickness single QW.

Within the tight-binding model the effective mass along the $z$ direction (evaluated at $k_z = 0$, i.e. the band bottom edge) is given by

$$\frac{1}{m_S L} = \frac{1}{\hbar^2}\frac{\partial^2 E}{\partial k_z^2} = \frac{\Delta d^2}{2\hbar^2}\cos(k_z d)|_{k_z=0} = \frac{\Delta d^2}{2\hbar^2}, \tag{2.26}$$

and the velocity by

$$v(k_z) = \frac{1}{\hbar}\frac{\partial E}{\partial k_z} = \frac{\Delta d}{2\hbar}\sin(k_z d). \tag{2.27}$$

Here we obtain the novel feature of the miniband, which is a possibility of a negative values of effective mass along the $z$-direction at $k_z > \pi/2d$. It means that in case of applied external force, **F**, an electron will (according the 2nd Newton's law) perform the oscillatory motion. First, it accelerates along the vector **F** till it reaches the negative mass $k_z$-space. There electron slows down till the $k_z = \pi/d$, where it stops ($v(k_z = \pi/d) = 0$) and finally goes backwards. Such an oscillatory behavior of electron within a miniband is considered in subsection 2.3.1.

### 2.1.4 Effect of the strain on the conduction band of quantum wells

Modern growth techniques allow the coherent growth of the thin layers of mismatched materials next to each other. The resultant strain placed on the material also affects the band structure and allows an additional degree of freedom in designing of optoelectronic devices. In this section we will discuss a simple model, the deformational potential theory, which if often used to describe the effects of strain on the band structure.

Let us first introduce the strain tensor, which describes the change of the crystalline lattice constant, $a_i$, due to the strain.

$$a_i^{strained} = \epsilon_{ij} a_j, \tag{2.28}$$

where $a_j$ is the j-th component of the lattice parameter in equilibrium, and $a_i^{strained}$ is the $i$-th component of the lattice parameter after the strain applied. For the system of our interest, pseudomorphic (without dislocations formation) growth is assumed. In this case, the epitaxial semiconductor layer is biaxially strained in the plane of the substrate by an amount $\epsilon_{||}$ and uniaxially strained in the perpendicular (growth) direction by an amount $\epsilon_{\perp}$. The in-plain lattice constant of two layers, coherently grown on each other is given by (25)

$$a_{||} = \frac{a_l G_l h_l + a_{sub} G_{sub} h_{sub}}{G_l h_l + G_{sub} h_{sub}}, \tag{2.29}$$

where $G_i$ denotes the shear modulus of $i$-th layer. In most of the cases we will consider thin strained layers grown on a thick substrate, $h_l \ll h_{sub}$. In such a limit case one obtains $a_{||} = a_{sub}$. For a thick substrate, the in-plain strain of the layer is determined from the bulk lattice constants of the substrate material, $a_{sub}$, and the layer material, $a_l$, by

$$\epsilon_{||} = \frac{a_{sub}}{a_l} - 1 \equiv \epsilon. \tag{2.30}$$

Because the layer is subjected to no stress in the perpendicular (growth) direction, the perpendicular strain $\epsilon_{\perp}$ is simply proportional to $\epsilon_{||}$ via

$$\epsilon_{\perp} = -\epsilon_{||}/\sigma, \tag{2.31}$$

where the constant $\sigma$ is the Poisson ratio. It depends on the $c_{11}$, $c_{12}$, and $c_{44}$ elastic stiffness constants of the layer and on the interface orientation.

$$\sigma_{001} = \frac{c_{11}}{2c_{12}}, \tag{2.32}$$

$$\sigma_{110} = \frac{c_{11} + c_{12} + 2c_{44}}{c_{11} + 3c_{12} - 2c_{44}}, \tag{2.33}$$

and

$$\sigma_{111} = \frac{c_{11} + 2c_{12} + 4c_{44}}{2c_{11} + 4c_{12} - 4c_{44}}. \tag{2.34}$$

Note, that for orientations, other than the (001), $a_{||}$ and $a_{\perp}$ do not represent the actual lattice constants in the crystallographic plane of the heterointerface, but merely express how the dimensions of the unit cell change under strain, as given by eq. 2.28. For the strains achieved by the lattice mismatched epitaxial growth on a (001) substrate the strain tensor is given by $\epsilon_{xx} = \epsilon_{yy} = \epsilon$ and $\epsilon_{zz} = -2c_{12}/c_{11}\epsilon$; all the off-diagonal strain terms are 0 in this case:

$$\hat{\epsilon} = \begin{pmatrix} \epsilon & 0 & 0 \\ 0 & \epsilon & 0 \\ 0 & 0 & -\frac{2c_{12}}{c_{11}}\epsilon \end{pmatrix}. \tag{2.35}$$

Once the strain tensor $\epsilon_{ij}$ is known, we can apply the deformational potential theory to calculate the effects of strain on various eigenstates in the Brillouin zone. The strain perturbation Hamiltonian $H\epsilon_{\alpha\beta}$ is defined and its effects are calculated from the first-order perturbation theory. In general we have (26; 27; 28)

$$H\epsilon_{\alpha\beta} = \Sigma_{ij} D^{ij}_{\alpha\beta}\epsilon^{ij}, \tag{2.36}$$

where $D^{ij}_{\alpha\beta}$ are the elements of the deformation potential operator and transform under symmetry operations as a second-rank tensor. A strain perturbation Hamiltonian for diamond lattices in the $|x>$, $|y>$, $|z>$ basis has been developed by Bir and Pikus (28).

Van de Walle's (25) Model-Solid Theory gives the expressions for relative shifts of conduction and valence bands valid for both, diamond and zinc-blende lattices in terms of model-solid deformation potentials:

$$\Delta\ E_c = a_c \frac{\Delta\Omega}{\Omega}, \tag{2.37}$$

$$\Delta\ E_{v,av} = a_v \frac{\Delta\Omega}{\Omega}, \tag{2.38}$$

where $E_c$ is the conduction band energy, $E_{v,av}$ is the average of the three top valence bands, $a_c$ and $a_v$ are the conduction and valence bands deformation potentials correspondently, $\frac{\Delta\Omega}{\Omega} = Tr(\hat{\epsilon}) = (\epsilon_{xx} + \epsilon_{yy} + \epsilon_{zz})$ is the fractional volume change.

### 2.1.5 Effect of magnetic field on the conduction band states of QW and SL

Since QW can be imagined as a particular case of a SL with infinitely thick barriers, let us consider the effect of magnetic field on the SL conduction band states. For an external magnetic field, B, applied to a superlattice, two basic configurations are possible. First, with B along the SL axis, i.e. perpendicular to the layers. Second, with B parallel to the layers.

In the first situation, the $z$-motion is separable from $x-y$ motion in the Hamiltonian, and the energy spectrum is given by (29)

$$E = E_{SL}(k_z) + (N + \frac{1}{2})\hbar\omega_c, \qquad (2.39)$$

where $\omega_c = eB/m$ is the cyclotron frequency with $1/m = 1/m_e^* + 1/m_h^*$, where $m_e^*$ is an electron effective mass, and $m_h^*$ is a hole effective mass. And $E_{SL}$ represents the miniband dispersion. In the limit of small magnetic fields, $\hbar\omega_c \ll \Delta$ ($\Delta$ is the miniband width), eq. 2.39 describes 3D electrons in a magnetic field (Landau levels). In the opposite limit, $\hbar\omega_c \gg \Delta$, the behavior rather bears similarities with the 2D case in that a real energy gap is opened between the Landau levels. However, the one-dimensional miniband dispersion $E(k_z)$ remains unchanged compared with the $B = 0$ case (see figure 2.3). This implies that the in-plane motion of the electrons is completely quantized and they can undergo truly one-dimensional motion along the superlattice axis.

When a magnetic field is applied in the plane of the layers (say, in $x$-direction), the motions in the plane and along the SL axis are coupled, and eigenvalues can be obtained by numerically diagonalizing the Hamiltonian (30; 31; 32)

$$H = \frac{\hbar^2}{2m}\frac{\partial^2}{\partial z^2} + \frac{1}{2}m\omega_c^2 z^2 + V_{SL}(z + Z_0). \qquad (2.40)$$

In general it results in the energy levels which depend on the position of electron, the Landau level center coordinate $Z_0 = -\hbar k_y/eB = -k_y l^2$, where $l$ is the, so called, magnetic length. Again, two limiting cases are possible: for energies much smaller than the width of the miniband, $\Delta$, the Landau levels are well defined in the usual sense (no $Z_0$ dependence) and the electrons perform a cyclotron motion through the barriers. The energy separation of Landau levels is then determined by the geometric mean of the in-plane effective mass and the superlattice effective mass, i.e. $\omega_c = eB/\sqrt{mm_{SL}}$. On the other hand, when the energies are lager than the miniband width (in the forbidden minigap), the Landau levels become dispersive.

If only the lowest Landau level is considered, the above condition is equivalent to the ratio $\hbar\omega_c/\Delta$ or to the ratio $d/l$ ($d$ is a superlattice period) being much smaller or greater than 1 (32). The latter condition can be interpreted classically: when the cyclotron diameter is comparable to or smaller than the SL period, the energy depends strongly on the orbit center position.

## 2.2 Intersubband spectroscopy

### 2.2.1 Interminiband transitions

Let us consider a superlattice with populated lowest miniband. When interacting with external electromagnetic field, the ground miniband electrons then can inelastically scatter into upper miniband states. Interaction of electrons with an external electromagnetic field is described by the perturbation Hamiltonian

$$H' = -\frac{e}{m_e}\mathbf{A}\cdot\mathbf{p}, \tag{2.41}$$

where $\mathbf{A}$ is the vector potential of the incoming light and $\mathbf{p}$ is the momentum operator. The induced transition rate between an initial state $i$ occupied by electron, and a final non-occupied state $f$, according to the Fermi's golden rule is given by

$$W_{if} = \frac{2\pi}{\hbar}| < i|H'|f > |^2\delta(E_f - E_i - \hbar\omega). \tag{2.42}$$

The absorption coefficient, $\alpha$, is defined as the ratio of the absorbed electromagnetic energy per unit time and volume and the intensity of the incident radiation, summed up over all the occupied initial states and non-occupied final states:

$$\begin{aligned}\alpha =&\frac{2}{(2\pi)^3}\frac{\hbar\omega}{I}\sum_{i,f}\int d^3k\frac{2\pi}{\hbar}| < i|\frac{e}{m_e}\mathbf{A}\cdot\mathbf{p}|f > |^2\\ &\times\left[f(E_i(\mathbf{k})) - f(E_f(\mathbf{k}))\right]\delta(E_f(\mathbf{k}) - E_i(\mathbf{k}) - \hbar\omega).\end{aligned} \tag{2.43}$$

$E_{i,f}$ are the full energy dispersions according to eq. 2.25 and $f(E_{i,f})$ are the Fermi-Dirac distribution functions of the initial and final states respectively. In the following we restrict ourselves to the $n = 2$ final miniband and $z$-independent electron effective mass $m_e$.

Using a parabolic in-plane dispersion, the integration over $k_x$ and $k_y$ can be performed analytically, and the only contribution to the matrix element in eq. 2.43 comes from the $z$ component. Thus intersubband transitions are allowed for radiation polarized perpendicular to the layers only. Of course, this is only true for simple isotropic band structures, as that we consider here. But, for instance, for holes (due to valence band mixing (33; 34; 35; 36; 37; 38; 39)), or when electron resides in a valley which is tilted with respect to the confinement direction (40; 41; 42; 43; 44; 45), so on, (see subsection 2.2.6) this restriction on polarization brakes up.

When one replaces the $\delta$-function by a normalized Lorenzian to account phenomenologically for the line broadening, eq. 2.43 transforms into

$$\alpha = \frac{e^2 kT}{\varepsilon\omega_c\eta\pi \mathrm{m}_e\omega/} \int_0^{\pi/d} dk_z | < 1|p_z|2 > |^2$$
$$\times \; ln \left( \frac{1 + e^{(E_F - E_1(k_z))/kT}}{1 + e^{(E_F - E_2(k_z))/kT}} \right) \left( \frac{\Gamma/\pi}{(E_2(k_z) - E_1(k_z) - \hbar\omega) + \Gamma^2} \right). \tag{2.44}$$

Here, $k$ is the Boltzmann's constant and $\eta$ is the refractive index, the other quantities have they usual meaning. The Fermi energy, $E_F$, has to be calculated from the electron concentration for each temperature.

Dimensionless quantity characterizing the strength of an optical transition, oscillator strength, is defined through the momentum matrix element by

$$f_{12}(k_z) = \frac{2}{m_e \hbar\omega_{21}} | < 1|p_z|2 > |^2. \tag{2.45}$$

In case, when the states 1 and 2 are localized in real space (which is not the case in superlattices), it is equivalently to use the oscillator strength definition through the coordinate matrix element:

$$f_{12} = \frac{2m_e\omega_{21}}{\hbar} | < 1|z|2 > |^2. \tag{2.46}$$

In the limiting case of vanishing dispersion along the $z$ direction, eq. 2.44 reduces to the absorption coefficient for the intersubband transitions in quantum well. For multiple quantum wells with thick barriers it is convenient to define a dimensionless absorption per well, which peak value at $T = 0$ is given after Khurgin (46) by

$$A = \frac{n_{2D} e^2 \hbar}{2\varepsilon_0 c\eta \; m_e \Gamma} f_{12}, \tag{2.47}$$

where $n_{2D}$ is the electron sheet density. This expression remains valid only as long as $A \lll 1$, otherwise one has to treat the layer taking into account the electrodynamic boundary conditions for a conducting sheet (47).

Optical absorption spectra of solids are often analyzed in terms of critical points (or van Hove singularities) of the joint-density of states, JDOS,

$$J(\omega) = \frac{2}{(2\pi)^3} \int d^3k \delta(E_2(\mathbf{k}) - E_1(\mathbf{k} - \hbar\omega)), \tag{2.48}$$

which is essentially what governs the frequency dependence of the absorption coefficient (apart from the two weight factors, i.e. the thermal occupation and the oscillator strength). Critical points occur wherever

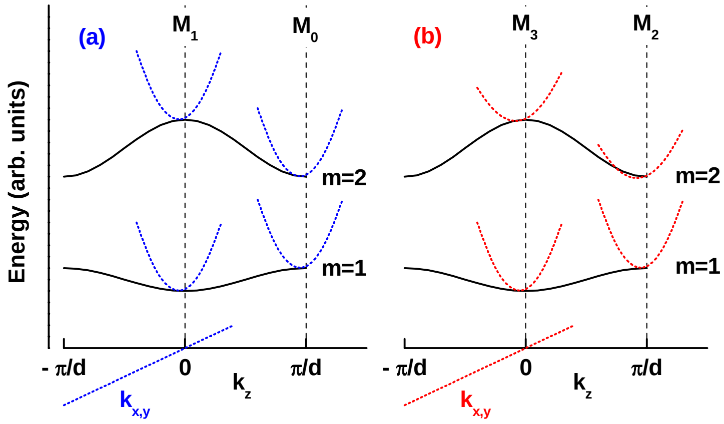

Figure 2.5: Classification of van Hove critical points (a) in case of parabolic band approximation, (b) when accounted for the band nonparabolicity. $m = 1$ and $m = 2$ are the ground and the first excited electron minibands correspondingly. Black curves represent energy dispersion in $z$-direction. The dotted curves represent the in-plane, $x - y$, energy dispersion.

the dispersion of two bands are parallel (see fig. 2.5) and can be classified according to the relative curvature of the two bands in each $k$-space direction (48; 49). In three dimensions, critical points are classified into $M_0$, $M_1$, $M_2$, and $M_3$, where the index indicates the number of $k$ directions in which the energy separation decreases away from the singularity. For example the direct fundamental band gap transition in direct band gap bulk semiconductor corresponds to $M_0$ critical point. Transition between the ground electron and hole minibands at the minizone center ($k = 0$) is also $M_0$, whereas one at the minizone edge ($k = \pi/d$) is $M_1$ transition. These have been observed by optical interband spectroscopy (50; 51; 52; 53). Transition between the ground electron and first excited electron minibands at the minizone center ($k = 0$) corresponds to $M_1$, and one at the minizone edge ($k = \pi/d$) corresponds to $M_0$ singularity in case of parabolic band approximation ($M_3$ and $M_2$ when accounted for the band nonparabolicity, see fig. 2.5). Considering only one dimension, it is possible to classify only two kinds of critical points: one of the minimum and one of the maximum transition energy. Around both of them

$$\frac{\partial k}{\partial \hbar\omega} \propto \sqrt{\hbar\omega}. \tag{2.49}$$

It is convenient to evaluate the JDOS using a tight binding energy dis-

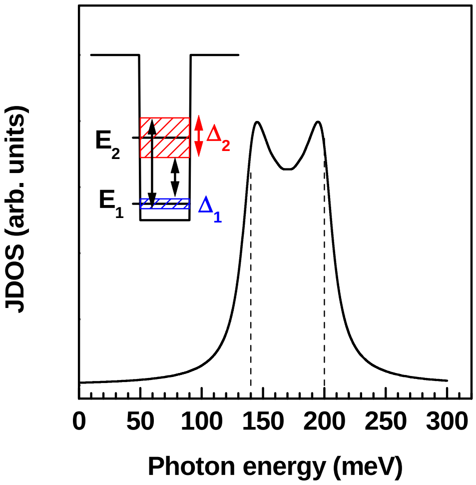

Figure 2.6: JDOS, calculated following eq. 2.48 with delta function replaced by Lorentzian to account phenomenologically for broadening, $\Gamma = 10meV$. Other parameters: $E_1 = 30$ meV, $E_2 = 200$ meV, $\Delta_1 = 10$ meV, $\Delta_2 = 50$ meV. Dash lines indicate transition energies at the center and edge of Brillouin mini-zone.

persion (54) along $z$ and a parabolic one along $x$ and $y$, which gives

$$J_{tb} = \frac{1}{\pi d S} \frac{1}{\sqrt{|[(\frac{\Delta_1}{2} + \frac{\Delta_2}{2})^2 - (\hbar\omega - E_2 + E_1]|}}, \tag{2.50}$$

where S is the sample area. Since the parabolic in-plane dispersion cancels in $\delta$-function, one is left with purely one-dimensional JDOS which exhibits two characteristics $\propto \sqrt{\hbar\omega}$ singularities at the low- and high-energy edges. This JDOS is symmetric (55) around $E_2 - E_1$, which is not the case for the Kronig-Penney model (54). Figure 2.6 shows JDOS after eq. 2.48 for the following parameters $E_1$=30 meV, $E_2$=200 meV, $\Delta_1$=10 meV, and $\Delta_2$=50 meV. Note that here we did account for broadening, and as a result the JDOS van Hove singularities spectral positions got shifted slightly away from the transition energies at the center and edge of Brillouin mini-zone.

If the electron concentration is high, several many-body effects become important (56; 57) for the calculation of the spectral position of the absorption peak. Also, the position of the resonant absorption and the lineshape are modified by the depolarization shift (58; 59; 60; 61) and exciton correction (56; 57) (the first is due to the resonant screening of the AC electric field of electromagnetic wave, the second is due to the interaction between the excited electron and the hole). The mentioned above effects will be considered in subsection 2.2.4.

### 2.2.2 Line broadening

Let us discuss different broadening mechanisms determining the linewidth of intersubband absorption.

(i) Phase breaking scattering processes: Each scattering event which changes the relative phase between the electron waves of the two involved subbands will also lead into a damping coherent intersubband transition. The corresponding phase-braking processes are the electron-electron scattering, the electron-phonon scattering and the scattering on potential fluctuations. These scattering processes lead to a homogeneous broadening of the intersubband absorption line, which is usually characterized by a dephasing time $T_2$. $T_2$ is a phenomenological parameter for the time scale on which the intersubband polarization decays. The homogeneous broadening makes significant contribution to the intersubband absorption linewidth. Very recently, the first direct experimental data on the homogeneous broadening become to be available (62; 63). The challenge of experimental evaluation of $T_2$ consists of difficulty of separation of homogeneous broadening from other mechanisms. Nonlinear spectroscopic methods (64) are the only tools which make it possible to separate the different contributions of line broadening.

(ii) Inhomogeneous broadening. Inhomogeneous broadening is a distribution of intersubband transition energies in the optically coupled range. It leads to a fast decay of macroscopic polarization caused by a destructive interference between the individual components. There is a variety of inhomogeneous broadening mechanisms: In most cases, the dispersion of subband energies in $k$-space (see fig. 2.7) is not parallel. And thus, the intersubband transition energies depend on the in-plane $k$-wavevector. Whenever the initial distribution of carriers covers the finite interval in $k$-space, this variation of intersubband transition energy causes the inhomogeneous broadening. In a single particle picture of non-interacting, independent two-level systems, this broadening has been estimated from the calculated subband dispersions , i.e. the effective masses and nonparabolicities and from the width of the carrier distribution function in $k$-space (65; 58). In addition to the non-parallel $k$-dispersion, the difference between the effective mass in the quantum well and the barrier can affect the linewidth (66).

A second important contribution to inhomogeneous broadening comes from disorder effects like fluctuations of the quantum well width or the alloy composition. In addition, the randomly distributed ionized donor-impurities lead to a weak fluctuating potential for the carriers in the wells. The influence of this effect on the intersubband absorption line depends strongly on the spatial overlap of the impurities potential and carrier distribution of quantized states (67).

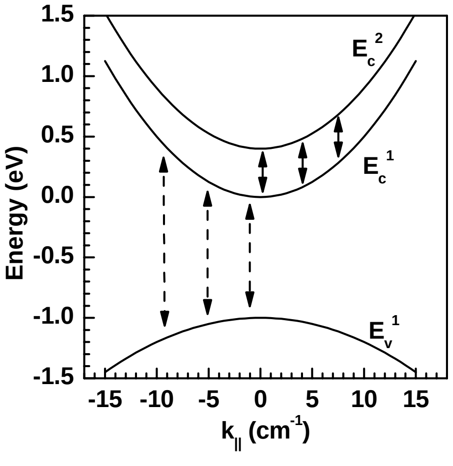

Figure 2.7: Schematic illustration of an in-plane dispersion of electron and hole subbands. Note significantly different variation of transition energies (and, consequently, inhomogeneous broadening) with $k$ for interband and intersubband transitions.

(iii) Many-body effects: The single particle picture of non-interacting, independent two-level systems breaks down at high carrier concentrations of several $10^{12}\text{cm}^{-2}$. In addition to the already mentioned single particle excitations, there are collective charge-densities and spin density oscillations in a dense two-dimensional plasma (68; 69; 70; 71; 72; 73; 74; 75; 76). The Coulomb interaction between the carriers occupying different states in ground and first excited subbands introduces coupling between the intersubband transitions at different $k$-vectors. This affects the shape of the absorption band, reducing the linewidth and shifting the position of the maximum of the absorption band towards the higher photon energies (60; 77; 78; 61; 59; 56).

Contrary to the Coulomb interaction, another many-body effect, Landau damping, is known to broaden the intersubband absorption line (79; 80). This effect is, basically additional scattering of the photon on the collective plasma oscillations, and is pronounced wherever the step of DOS exist.

### 2.2.3 Oscillator strength and sum rules

In atomic systems the so-called $f$-sum rule for the oscillator strength is known to hold, which reads

$$\sum_j f_{ij} = 1. \tag{2.51}$$

Here $i$ is the initial state and the sum is performed over all the final-state quantum numbers $j$. For absorption processes $f_{ij}$ is positive, for emission processes it is negative. The sum rule can also readily be applied to a single, infinite potential quantum well. There, the oscillator strength can be evaluated analytically, to give

$$f_{ij} = \frac{64}{\pi^2} \frac{i^2 j^2}{(j^2 - i^2)^3}. \tag{2.52}$$

For example, $f_{12} = 0.96$, $f_{23} = 1.87$, $f_{14} = 0.03$. Due to the inversion symmetry, transitions between two even or two odd states are forbidden.

For an electron in a periodic potential, Ehrenreich and Cohen(81) have derived a modified sum rule, which reads

$$\sum_j f_{ij} + \frac{m_e}{\hbar^2} \frac{\partial^2 E_i(k_z)}{\partial k_z^2} = 1 \tag{2.53}$$

or

$$\sum_j f_{ij} = 1 - \frac{m_e}{m_{SL}^{(i)}}. \tag{2.54}$$

Here $m_e$ is the bulk conduction band mass and $m_{SL}^{(i)}$ is the superlattice mass in the $i$th miniband, evaluated at $k_z$. The first term in eq. 2.53 describes transitions between different minibands and the second term describes free-carrier type transitions.

Let us now to put the explicit expression of the tight-binding miniband energy dispersion eq. 2.25 in eq. 2.53 and consider $k$-dependent oscillator strength for absorption transitions in two miniband system. In two miniband model the sum over the $j$ states in 2.54 disappears, and we obtain

$$f_{12}(k_z) = 1 - \frac{m_e \Delta_1 d^2 \cos(k_z d)}{2\hbar^2} \tag{2.55}$$

As illustrated in fig. 2.8, the oscillator strength is suppressed at the Brillouin mini-zone center and increases up to the Brillouin mini-zone edge. But in average it is equal to the oscillator strength in an isolated QW. Specific feature of the oscillator strength in superlattice is that it becomes greater than unity for $k - z > \pi/2d$. Physical origin of such a behavior is a negative superlattice effective mass in this region of $k_z$.

### 2.2.4 Many body effects on the intersubband transition

Before we introduce the many-body effect on the intersubband transitions, let us first account for the depolarization (plasmon shift) and exiton-like (interaction of electron with the hole in the ground state)

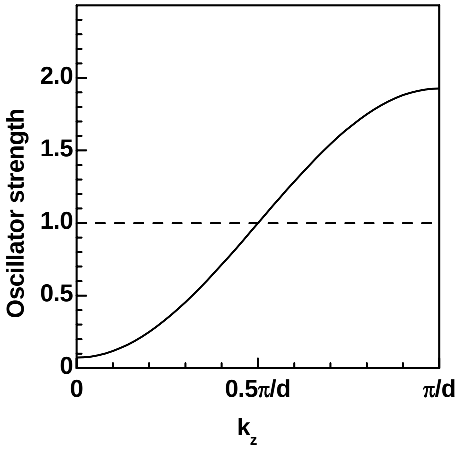

Figure 2.8: Oscillator strength $f_{12}$ as a function of $k_z$ for the superlattice parameters $\Delta_1 = 10meV$, $d = 10nm$, $m_e = 0.060m_0$.

effects on the transition energy, $\hbar\omega_0$. In order to include these effects let us use the Ando's formalism (77), which gives the shifted intersubband transition energy, $\Delta\ E$, as

$$\Delta\ E = \hbar\omega_0\sqrt{1+\phi-\beta}, \tag{2.56}$$

where the factor $\phi$ accounts for the depolarization shift and is given by

$$\phi = 2\frac{4\pi \mathrm{e}^2}{\varepsilon} n_{2D}\ S_{01}\frac{1}{\hbar\omega_0}, \tag{2.57}$$

where $n_{2D}$ is the two-dimensional density of electron gas, $\varepsilon$ is the dielectric constant, and $S_{01}$ is the Coulomb matrix element given by

$$S_{01} = \int_0^\infty dz \left(\int_0^z \xi_1(z')\xi_0(z')dz'\right)^2, \tag{2.58}$$

where $\xi_0$ and $\xi_1$ are the wave functions for the ground and excited state, respectively. The factor $\beta$ in eq. 2.56 accounts for the exciton-like shift given by

$$\beta = -\frac{2n_{2D}}{\hbar\omega_0}\int_{-\infty}^{+\infty} dz\xi_1(z)^2\xi_0(z)^2\frac{\partial V_{xc}(n_{2D}(z))}{\partial n_{2D}(z)}, \tag{2.59}$$

where $V_{xc}(n_{2D}(z))$ is the exchange-correlation potential as a function of the local sheet density $n_{2D}(z)$ and is described elsewhere (57). Three points should be mentioned here. First, the exciton-like shift is very small as compared to the depolarization shift. Second, eq. 2.56 produces a trend similar to that of the experimental data (70; 82), i.e. a blue-shift as $n_{2D}$ increased. Third, the experimental peak position energy as a function of $n_{2D}$ is much larger than the results obtained from eq. 2.56 (59; 83). Thus, the depolarization and exciton-like shifts alone do not appear to account for what is observed experimentally and therefore other effects should be considered.

Since the dopant densities, necessary to obtain intersubband transitions experimentally, are relatively high, $\sim 10^{11} - 10^{12} cm^{-2}$, one would expect that the many body effects such as electron-electron exchange and direct Coulomb interactions for the ground state are significant. In order to include the exchange interaction energy, let us use an expression for the energy, which is based on the Hartree-Fock approximation, derived after Manasreh *et al.* (59; 83) and given for the $m$-th subband by

$$E_{exch} = -\sum \int d\mathbf{r} \int d\mathbf{r}' \frac{e^2}{4\pi\varepsilon} \frac{1}{|\mathbf{r} - \mathbf{r}'|} \Psi_n^*(\mathbf{r}')\Psi_m(\mathbf{r}')\Psi_n(\mathbf{r})\Psi_m^*(\mathbf{r}), \quad (2.60)$$

where the summation is taken over all the occupied subbands. In order to render the model analytic, following Bandara *et al.* (78),let us use the wave functions for a simple parabolic band and an infinite square well. With these simplifications, eq. 2.60 reduces for the ground state to:

$$E^{(0)}_{exch}(k) = -\frac{e^2 k_F}{4\pi\varepsilon} \left[ \frac{2}{\pi} \mathbf{E}\left(\frac{k}{k_F}\right) - \left(\frac{\pi}{6} - \frac{5}{8\pi}\right) \frac{k_F}{k_L} \right] \quad \text{for} \quad (k < k_F). \quad (2.61)$$

and

$$E^{(0)}_{exch}(k) = -\frac{e^2 k_F}{4\pi\varepsilon} \left[ \frac{2}{\pi\, k_F} \left( k\mathbf{E}\left(\frac{k_F}{k}\right) + \frac{k_F^2 - k^2}{k} \mathbf{K}\left(\frac{k_F}{k}\right) \right) - \left(\frac{\pi}{6} - \frac{5}{8\pi}\right) \frac{k_F}{k_L} \right] \quad \text{for} \quad (k > k_F) \quad (2.62)$$

For the first excited state eq. 2.60 reduces to

$$E^{(1)}_{exch}(k) = -\frac{e^2 k_F}{4\pi\varepsilon} \left(\frac{5}{9\pi}\right) \frac{k_F}{k_L}, \quad (2.63)$$

where $k$ is the magnitude of the $k_{||}$ wavevector, $k_F$ is the Fermi wavevector ($k_F = \sqrt{2\pi n_{2D}}$), $k_L = \pi/L$, $\mathbf{E}(x)$ is an elliptic integral of the second kind, and $\mathbf{K}(x)$ is an elliptic integral of the first kind. The fact that the ground state is $k$-dependent, while the excited state is not, is due to the orthogonality of the ground and excited state wave functions. It should be noted that the exchange energy shifts in eqs. 2.61–2.63 are defined for low temperatures only. The Hartry-Fock exchange energy suffers the well-known defect of an infinite slope at the Fermi wave vector. This gives rise to an unphysical "dip" in the absorption spectrum at $k = k_F$ and a zero density of states at the Fermi energy.

By adding $E^{(0)}_{exch}(k)$ and $E^{(1)}_{exch}(k)$ to the ground state energy, $E_0$, and the excited state energy, $E_1$, in eq. 2.44, respectively, one can obtain the new peak position energy of the intersubband transitions which is defined here as $\hbar\omega_1$. It should be pointed out that the exchange interaction alone when it is added to the single-particle calculations cannot explain the peak position as a function of $n_{2D}$ (59; 83). The theory can be further improved by replacing $\hbar\omega_0$ in eqs. 2.56,2.57, and 2.59 with

$$\hbar\omega_2 = \hbar\omega_1 - E_{dir}, \tag{2.64}$$

where the direct Coulomb interaction energy for the ground state, $E_{dir}$, derived for an electrically neutral doped well is given after Bandara *et al.* (78) by

$$E_{dir} = \frac{3n_{2D}\ e^2}{8\varepsilon\ k_L^2 L}. \tag{2.65}$$

The effect of $E_{dir}$ term on $\Delta\ E$ is small as compared to that of $E_{exch}$ or the depolarization shift (59; 83). But it grows with $n_{2D}$ and becomes considerable for a high carrier densities (~10 meV for $10^{12} cm^{-2}$ sheet density range).

In the end it worth to mention, that the same theory properly describes the observed experimentally (59; 83) blue-shift of the intersubband peak energy with reducing the temperature (~5 meV for $10^{12}$ cm$^{-2}$ sheet density range).

### 2.2.5 Band nonparabolicity effects in semiconductor quantum wells

**Simple description of the band nonparabolicity effect**

Energy band structure of semiconductor crystals is build so, that there are many energy band extrema (see fig. 2.9 (a)) in the certain points of reciprocal space: $L$, $\Lambda$, $\Gamma$, $\Delta$, $X$, $K$, and $\Sigma$. The most of the crystal electronic properties are defined by the lowest minimum of the conduction band and the top maximum of the valence band. Usually, such a minimum is interpolated by parabola (dash line fig. 2.9 (b)), which is valid for the very close vicinity of the symmetry points of $k$-space. The deviation of the real band from the parabola (see fig. 2.9 (a)) is called an energy band nonparabolicity. A nonparabolicity of the energy dispersion in the neighborhood of energy band extrema in bulk semiconductors can be approximately accounted as follows

$$E = \frac{\hbar^2 k^2}{2m_e}\left(1 - \gamma k^2\right), \tag{2.66}$$

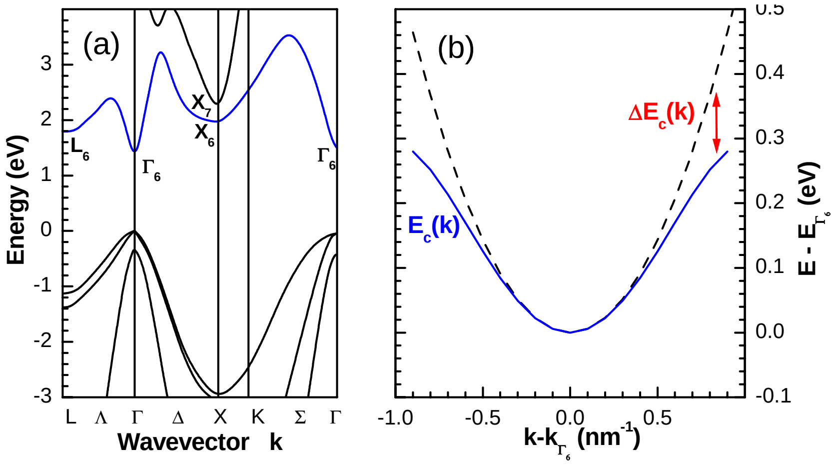

Figure 2.9: Band nonparabolicity effect on the conduction band energy dispersion.

Table 2.1: The nonparabolicity parameters derived for some semiconductors.

| material | $\gamma \times 10^{19} m^{-2}$ | material | $\gamma \times 10^{19} m^{-2}$ |
|---|---|---|---|
| $GaAs$ (84) | 4.9 | $In_{0.70}Ga_{0.30}As$ (5) | 15.3 |
| $In_{0.32}Ga_{0.68}As$ (85) | 3.9 | $In_{0.73}Ga_{0.27}As$ (86) | 12.8 |
| $In_{0.32}Ga_{0.68}P$ (85) | 1.5 | AlAs (86) | 0.9 |
| $In_{0.53}Ga_{0.47}As$ (5) | 11.3 | $In_{0.55}Ga_{0.45}As$ (86) | 3.5 |

where $E$ is the carrier energy, relatively to the band edge in the extremum point, $k$ is the wavenumber, $m_e$ is the effective mass of the carriers, and $\gamma$ is, so called, the nonparabolicity parameter. The nonparabolicity term lowers the band edge by a fractional amount of $\gamma k^2$ (see fig. 2.9 (b)). The values of nonparabolicity parameters of some semiconductors are listed in table 2.1. It is seen from eq 2.66, that the band nonparabolicity effect is noticeable for the carriers with $k \neq 0$, i. e. for the carriers above the band edge. Quantum confined carriers in heterostructures (QW, SL) are the case. For simplicity, let us consider an electron in the conduction band. If due to the spatial confinement the electron energy spectrum becomes quantized into $E_1$, $E_2$ .... eigen states above the band edge, than the wavenumber, $k_1$, for the lowest (first) state is equal

$$k_1^2 = 2m_e E_1/\hbar^2 \tag{2.67}$$

and the band lowering due to the band nonparabolicity is found to be

$$\Delta E = -\gamma \hbar^2 k^4 / 2m_e = -\gamma 2 m_e E_1^2 / \hbar^2. \tag{2.68}$$

As we see from eq 2.68, this effect grows up quadratically with the confinement energy, therefore should be much more pronounced for the states confined high above the conduction band edge. Note, that as long as we introduced nonparabolic energy dispersion 2.66, the eq. 2.67 now is only approximately valid for the small $k$ values. In fact, we should use for $k_1$ the solution of eq. 2.66

$$k_1^2 = \left(1 - \sqrt{1 - 8\gamma E_1 m_e / \hbar^2}\right) / 2\gamma \tag{2.69}$$

(which in the $\gamma \to 0$ limit transforms back into eq. 2.67). While the band dispersion is not parabolic anymore, we should comment on the effective mass concept which we still use up to now. Strictly speaking, the whole concept of effective mass breaks up, since the previous physical meaning of $m_e$ parameter is lost. $\partial^2 E(E_1)/\partial\, k^2$ is not the $\hbar^2/m_e$ constant anymore. Instead,

$$\partial^2 E(E_1)/\partial k^2 = \hbar^2/m_e(1 - 6\gamma k_1^2), \tag{2.70}$$

where $k_1$ is as in eq. 2.69. The meaning of $m_e$, which we keep using, now is related to the second derivative of $E(k)$, but only at $k = 0$.

Let us consider now, how to solve the Hamiltonian for the conduction band, for example, including the band nonparabolicity. Among the simplified approaches, which give simple analytical expressions for the QW (SL) energies by neglecting second-order terms in the $\mathbf{k} \cdot \mathbf{p}$ Hamiltonian, we can distinguish the two-band $\mathbf{k} \cdot \mathbf{p}$ EFA model originally proposed by Bastard (19; 20), its three-band extension (87), and an empirical version of it proposed by Nelson (84). Comparative analysis (88) of all three simplified models with respect to the transfer matrix method (TMM) reveals a very good agreement between empirical Bastard model (EBM) (84) results and those calculated by the TMM and the Extended Bastard Model (88) techniques. Discrepancy in energy levels positions is found to be less than 1 meV. Advantages of EBM technique are that (i) it considers the single band, (ii) it gives the analytical equations for the eigenstates problem, (iii) it accurately treats the nonparabolicity effect and deals with the correct effective mass, by having the $\gamma$ and $m_e$ be as the input parameters.

### Energy dependent effective mass approximation (Empirical Bastard Model)

Let us now describe the basic assumptions of EBM. EBM takes the analytical solution of the Hamiltonian for the single parabolic band, eqs.

2.21, 2.22, 2.23, and 2.24, (i.e. one which does not include the nonparabolicity) and introduce the nonparabolicity effect via the energy dependent effective mass (84).Thus, it holds the dispersion relation in the quasi "free particle form"

$$E = \hbar^2 k^2 / 2m_e(E). \tag{2.71}$$

The assumption of the model (84) is the explicit expression for the $m_e(E)$

$$m_e(E) \equiv m_e(1 + E/E_l), \tag{2.72}$$

where $E_l$ is an energy gap between the conduction and light-hole valence bands. The nonparabolicity parameter is related to the energy gap and the effective mass at $k = 0$ by

$$\gamma = \hbar^2 / 2m_e E_l. \tag{2.73}$$

The boundary conditions at the well-to-barrier interface are

$$m_e^w / m_e^b = E_l^w / E_l^b, \tag{2.74}$$

$$\gamma_w / \gamma_b = (m_e^b / m_e^b)^2. \tag{2.75}$$

Here, $\gamma$ and $m_e$ are the input parameters ($E_l$ can be expressed through eq. 2.73). Here we want to stress once again the important fact, that EBM does not operate with the dispersion relation 2.71 then solving the Hamiltonian (it would not end up with a simple analytical solution in form of eq. 2.21). But, instead, it takes the simple solution for the parabolic band eq. 2.21 and postulates the nonparabolicity influence that has to result in the same solution, but with the $m_e(E)$, instead of $m_e$. For the case of SL the dispersion relations for the well are

$$E_w = \hbar^2 k_w^2 / 2m_e^w(E), \tag{2.76}$$

and for the barrier

$$E_b = V - \hbar^2 k_b^2 / 2m_e^b(E), \tag{2.77}$$

with the boundary conditions

$$\begin{aligned} \cos(k_z d) = {} & \cos(k_w l_w)\cos(k_b l_b) \\ & - 1/2[m_e^w k_b / m_e^b k_w + m_e^b k_w / m_e^w k_b]\sin(k_w l_w)\sin(k_b l_b) \end{aligned} \tag{2.78}$$

The resulting effects of nonparabolicity on the eigenstates values are: (i) the nonparabolicity has a very small effect on the lowest subband edge regardless on the QW width and hence the energy of the state; (ii) the nonparabolicity causes a raising of the lowest subband edge; (iii) the

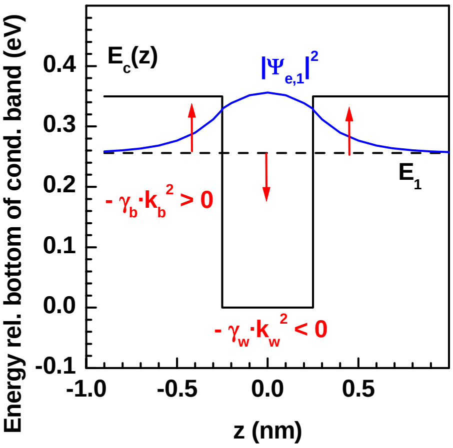

Figure 2.10: Illustration to the effect of interplay of the well and barrier band nonparabolicities on the confinement energy (see Eqs. 2.68 and 2.79).

nonparabolicity causes a lowering of subband edge energies of higher subbands and the effect becomes substantial for the highest subband edges. The rising of the lowest subband edge (instead of the expecting lowering of all the subbands) and extremely strong influence of nonparabolicity on the highest subband edge can be explained in terms of competition between the nonparabolicities in the well and in the barrier (see fig. 2.10). The nonparabolicity in the well tends to lower the energy levels while that in the barrier raises them. The reason why the nonparabolicity of the barrier dominates in the case of the lowest quantum level can be understood in terms of the relative occupancies in the well and in the barrier (84; 88) and by the $k$-value in each layer. Within the framework of the Perturbation Theory

$$\Delta E_1 = \int_{-\infty}^{+\infty} \Delta E_c(z) \Psi_{e,1}(z) dz, \tag{2.79}$$

where $\Delta E_1$ is the energy shift of the ground confined state of electron, $\Delta E_c(z)$ is the shift of the conduction band edge due to nonparabolicity (see Eq. 2.68), and $\Psi_{e,1}(z)$ is the ground state electron wave function.

### 2.2.6 Selection rules for conduction band intersubband transitions in (001)-grown quantum wells

To address the question of intersubband transitions selection rules in details, we first consider the 8-band $\mathbf{k} \cdot \mathbf{p}$ calculation results of Yang *et al.* (89). In case when the principal quantum number change, $\Delta n$, is an odd integer (1,3,...), the optical intersubband transitions are allowed of both, TE and TM, polarizations. TM-polarized transition will be dominating. The ratio of correspondent optical matrix elements, evaluated at the zero in-plane wave vector is given by (89):

$$\frac{\mid M_{TE} \mid}{\mid M_{TM} \mid} \approx \frac{1}{3} \frac{(E_{n'} - E_n)\Delta}{(E_n + E_g + \Delta)(E_{n'} + E_g)}, \tag{2.80}$$

where $E_n$ and $E_{n'}$ are the initial and the final state energies correspondingly, $E_g$ is a fundamental energy gap, and $\Delta$ is a valence band spin-orbit splitting. Formula 2.80 gives approximately 0.004 for GaAs QW with 124 meV spacing of $n$ and $n'$ for. And the ratio of the correspondent absorption coefficient is, consequently, square of it, i.e. 0.000016. The ratio 2.80 increases slightly with the in-plane wave vector, as it has been demonstrated by Voon *et al.* (90).

In case when the principal quantum number change, $\Delta n$, is an even integer (2,4,...), the optical intersubband transitions of both, TE and TM, polarizations are again allowed, but only for the electrons with a non-zero in-plane wave vector. The transition rates are proportional to the value of the in-plane wave vector. In this case the TE-polarized transition is dominant. The ratio of correspondent optical matrix elements is given by (89):

$$\frac{\mid M_{TM} \mid}{\mid M_{TE} \mid} \approx \frac{\sqrt{2}}{3} \frac{(E_{n'} - E_n)\Delta}{(E_n + E_g + \Delta)(E_{n'} + E_g)}. \tag{2.81}$$

It is important to stress, however, that the strength of the TE-polarized transitions for even values of $\Delta n$ is comparable with the strength of the TE-polarized transitions of odd $\Delta n$, i.e. still much weaker than the TM-polarized transitions of odd $\Delta n$.

The more sophisticated 14-band $\mathbf{k} \cdot \mathbf{p}$ calculations (91), concludes, however, the strength of the TE-polarized transitions of up to 20% of that of TM-polarized transition in thin quantum wells. The lack of inversion symmetry in zinc-blende materials allows to introduce the additional term in the intersubband optical matrix element for the TE-polarization in the 14-band model, which is, however, not taken into account in the 8-band calculations.

From the application point of view (surface emitting QCL, normal incidence QWIP), it would be likely, however, to realize the strong in-plane polarized intersubband transitions. Extensive experimental (92; 93) and theoretical (91; 94; 95) efforts were pointed towards the "break" of selection rules in quantum wells.

## 2.3 Vertical transport and carrier dynamics

### 2.3.1 Miniband transport

**Bloch oscillations**

A very elementary solution for the superlattice transport has been provided by Esaki and Tsu in their pioneering paper (96). Let us assume that in the lowest miniband the states close to the miniband minimum at $k_z = 0$ are occupied and are in thermal equilibrium. If the electric field is applied in the $z$-direction, the Bloch states are no longer the eigenstates of the total Hamiltonian but change in time. According to the acceleration theorem (14)

$$\frac{dk_z}{dt} = \frac{eF}{\hbar}, \tag{2.82}$$

the states remain to be the Bloch states with respect to time, but the Bloch vector becomes time dependent. And if an electron starts at the minimum of the miniband at $t = 0$ we find $k_z(t) = eFt/\hbar$. At $t = \pi\hbar/(eFd)$ the boundary of the Brillouin zone ($k_z = \pi/d$) is reached. Due to a periodicity, this point is equivalent to the point $k_z = -\pi/d$, so that the trajectory continues at $k_z = -\pi/d$, which is often called a Bragg-reflection. Finally, at $t = \tau_{Bloch} = 2\pi\hbar/(eFd)$ the electron gets back to initial position. So the electron performs an oscillatory movement in $k$- and also in real space with the angular frequency $eFd/\hbar \equiv \omega_B$, the Bloch frequency. These are the famous Bloch oscillations. Recently they have been observed experimentally through the four-wave mixing (97; 98) and also by measuring directly the THz radiation emitted by the oscillating charge at the Bloch frequency (99). If one uses the tight-binding energy dispersion, the velocity of Bloch states propagation in $k$-space is

$$v = \frac{\Delta d}{2\hbar} \sin\left(\frac{eFdt}{\hbar}\right). \tag{2.83}$$

Thus, the spatial displacement of the wavepacket is described (100) as $z(t) = z_0 + (\Delta/2eF)(1 - cos(eFdt/\hbar))$. The real-space displacement of Bloch-oscillating electrons was observed experimentally in semiconductor superlattices (101).

**Relaxation time approximation**

Scattering processes will interrupt the oscillatory behavior. As scattering processes are likely to restore the thermal equilibrium, it makes sense to assume that the scattered electron will be found close to $k_z = 0$. As long as the average scattering time $\tau$ is much smaller than $\pi\hbar/(2eFd)$, the electrons will remain in the range $0 \leq k_z < \pi/(2d)$, where the velocity increases with $k_z$ and thus an increase of $F$ will increase the average drift velocity. Thus for $eFd \ll \pi\hbar/(2\tau)$ a linear increase of $\upsilon_{drift}(F)$ is expected. In contrast, if $\tau \geq \pi\hbar/(eFd)$ the electrons reach the region $-\pi/d < k_z < 0$ with negative velocities and thus the average drift velocity can be expected to drop with the field for $eFd \geq \pi\hbar/\tau$. For high fields, $eFd \gg 2\pi\hbar/\tau$, the electrons perform many periods of the Bloch oscillations before they are scattered and thus the average drift velocity tends to the zero for $F \rightarrow \infty$. A detailed analysis for a constant (momentum-independent) scattering time $\tau$ gives Esaki-Tsu relation (96) :

$$\upsilon_{drift}(F) = \upsilon_{Esaki-Tsu}(F) = \frac{d\Delta}{2\hbar}\frac{eFd\hbar/\tau}{(eFd)^2 + (\hbar/\tau)^2}. \tag{2.84}$$

The drift velocity exhibits a linear increase with $F$ for low fields, a maximum at $eFd = \hbar/\tau$ and a negative differential conductivity for $eFd > \hbar/\tau$, see fig. 2.11. This general behavior also is observed experimentally (102; 103).

If the thermal equilibrium is not achieved within a single scattering event, but needs a sequence of inelastic processes with the energy loss per event equal $\hbar\omega_{scatt}$ (104), the obtained field dependence of drift velocity agrees qualitatively with the case above. Except in the low field regime the drift velocity is $\Delta/(2\hbar\varpi_{la})$ tines smaller. The physical reason of this effect is clear: the electron needs to be scattered $\Delta/(2\hbar\varpi_{la})$ times before it reaches the thermal equilibrium, when previously it was assumed to occur within a single scattering event.

Given above description of miniband transport is extremely simplified. It does not account for lateral motion and thermal carrier distribution, and uses the single relaxation time constant to account for the variety of possible scattering processes. However, the general trend of the miniband transport behavior is correct (for the electric field values where the miniband concept is still valid). For detailed miniband transport description see, for example, a recent review by Wacker (105) and references therein.

### 2.3.2 Wannier-Stark hopping

If the electric field applied to a superlattice along the $z$ direction is strong enough, the miniband breaks into a set of discrete, equidistant energy levels, which are localized in real space within a scale of one period of the superlattice (see fig 2.12). This is a Wannier-Stark ladder, which energy spectrum is given by(106; 107; 108)

$$E_{WS} = \nu\ eFd + E_{\perp}. \tag{2.85}$$

Here $F$ is the electric field strength and $E_{\perp} = (\hbar^2/2m_e)(k_x^2+k_y^2)$. The existence of the Wannier-Stark ladder (109; 110) was observed experimen-

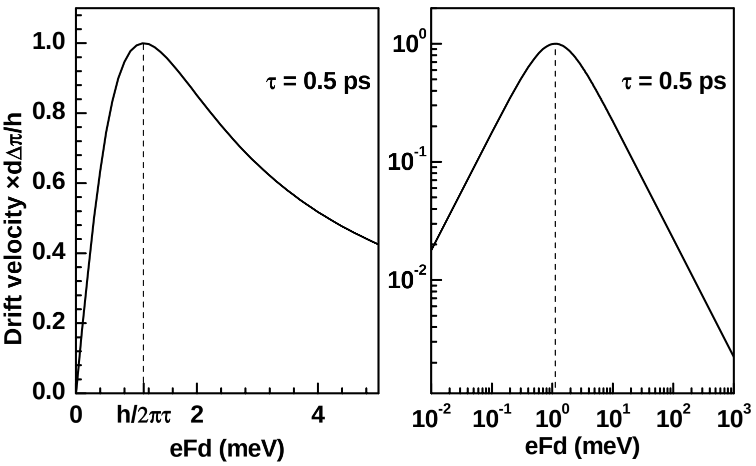

Figure 2.11: Esaki-Tsu miniband drift velocity calculated for 0.5 ps relaxation time following eq. 2.84, plotted in liner scale (left hand panel) and bilogarithmic scale (right hand panel).

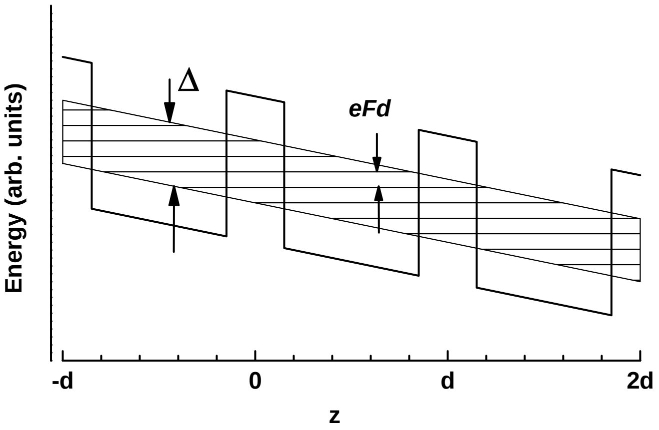

Figure 2.12: Schematic illustration of the superlattice conduction band edge under applied electric field along the $z$ direction. Horizontal lines represent the Wannier-Stark levels.

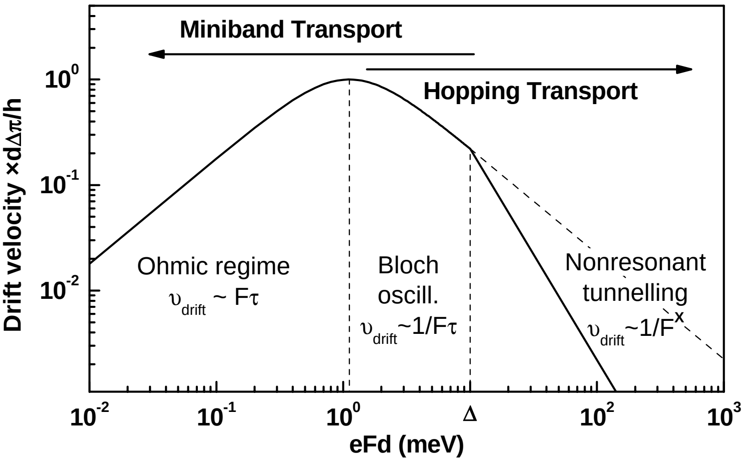

Figure 2.13: Schematic double logarithmic diagram of the zero-temperature electron drift velocity. Exact value of parameter $x$ depends on the actual dominant scattering process.

tally by optical spectroscopy in the semiconductor superlattice (101; 111).

The only difference between the Wannier-Stark ladder and the case of discussed in previous subsection Bloch oscillations is that the energy splitting between the localized states is large enough to be spectrally resolved. Such a situation happens in superlattices in high electric fields. Scattering processes cause the energy loss and consequently transitions between the individual eigenstates, yielding a net current in the direction of electric field (112). This mode of the carrier transport is called the Wannier-Stark hopping.

Very close numerical results for the electric field dependent drift velocity have been obtained for both the Miniband Transport and Wannier-Stark hopping approximation (104) in the high electric field regime.

In case of extremely high electric fields (i.e. $eFd > \Delta$) the localization length of Wannier-Stark states becomes shorter than the miniband period, and analogy with the regime of Bloch oscillations breaks down. For this very high field range the decrease of drift velocity follows the $1/F^2$ dependence (104) when the longitudinal acoustic phonon scattering dominates; or the $1/F^{3.5}$ dependence (113) if the impurity scattering dominates.

Figure 2.13 shows following Ref. (104) the resultant drift velocity field dependence in the regimes of miniband transport and Wannier-Stark hopping.

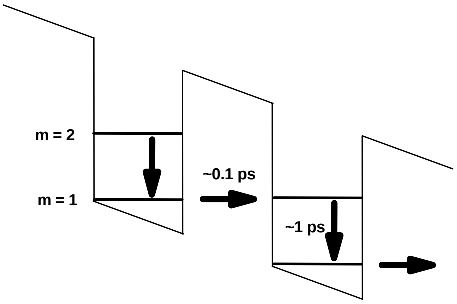

Figure 2.14: Schematic illustration of the sequential resonant tunnelling process (horizontal arrow) and subsequent intra-well intersubband carrier relaxation (vertical arrow).

### 2.3.3 Sequential resonant tunnelling

The superlattices with thick barriers (i.e. narrow minibands) can fairly well considered as a sequence of weakly coupled quantum wells with spatially localized eigenstates. Due to the residual coupling between the wells, tunnelling processes through the barriers are possible and the electrical transport results from Sequential Tunnelling from one well to another.

At the finite fields, the ground states get misaligned in energy space and the resonant tunnelling becomes forbidden. However, in this regime the current is possible due to the scattering induced broadening of eigenstates. This case is similar to the hopping transport at extremely high electric fields (as described in previous section) in a sense that the spatial overlap of the eigenstates is negligible.

Transport conditions change drastically, when the electric field is strong enough to align the energy of the ground state of one quantum well with the excited state energy of the subsequent quantum well. In this case resonant tunnelling occurs. Due to its high probability the resonant tunnelling results in a peak of drift velocity at the resonant field conditions. This peak is broadened due to (i) the scattering assisted transport at the field values around the resonance and (ii) the well thickness fluctuations. Corresponding scattering time, $\tau_{\perp}$, can be evaluated from the resonant peak half-width at half-maximum, $\delta F$, if the input of (ii) is subtracted (114):

$$\tau_{\perp} = \hbar / ed\delta F. \tag{2.86}$$

This gives the $\tau_{\perp} \cong 100fs$ approximation for the experimental data obtained in Ref. (114). The carrier relaxation time from the excited state into the ground state in a subsequent well (see fig. 2.14) is approximately one order of magnitude higher for the appropriate intersubband spacing (115). Therefore, the transport in case of sequential resonant tunnelling (in case of Ref. (114)) is limited by the intra-well relaxation rate.

### 2.3.4 Inter/intra-subband carrier dynamics

After tunnelling into the excited state subband (arrow "IN", Fig. 2.15), the electron can undergo a coherent intersubband transition with photon emission (arrow 1 Fig. 2.15) or a complex relaxation scenario (arrows 2 and 3, Fig. 2.15) without photon emission. Relevant scattering events are mainly electron-electron and electron-longitudinal optical phonon scattering. The first leads to the heating of electron plasma and the second transfers the excess energy to the crystal lattice. Process 2 in Fig. 2.15 is called the *intersubband scattering.* It can be assisted with either the LO-phonon emission (dominates at $T = 0$) or absorption (dominates at high $T$). Auger processes are also possible, but relevant scattering rates are small, usually in the range of $(1\ \mathrm{ns})^{-1}$. The process 3 in Fig. 2.15 is called the *intrasubband scattering* (dominated by the electron-LO-phonon scattering at low doping) A combination of last two processes is refereed as an intersubband carrier *relaxation.* All the processes, mentioned above, play the crucial role in functioning of QCL. In a particular focus are the correspondent transition rates.

Intersubband scattering from the upper state $m = 2$ to the lower subband/subbands is one of the main "parasitic" processes which depopulate higher lasing state, and thus, reduce the population inversion. Ferreira and Bastard (116) have elaborated a widely used approach for calculation of the electron–LO-phonon scattering rates in QWs. The rate of scattering from an initial electron state $i|\mathbf{k}_i>$ into a final state $j|\mathbf{k}_j>$ due to the LO-phonon emission at $T = 0$ is equal to:

$$\frac{1}{\tau_{ij}} = \frac{m_e^* e^2 \Omega_{\mathrm{LO}}}{2\hbar^2 \varepsilon_\rho} \int_0^{2\pi} d\theta \frac{I^{ij}(Q)}{Q}, \tag{2.87}$$

where

$$Q = (k_i^2 + k_j^2 - 2k_i k_j \cos\theta)^{1/2} \tag{2.88}$$

is the length of the $\mathbf{k}_i - \mathbf{k}_j$ vector (equals to the emitted LO-phonon $k$-vector);

$$k_j^2 = k_i^2 + \frac{2m_e^*}{\hbar^2}(E_i - E_j - \hbar\Omega_{\mathrm{LO}}), \tag{2.89}$$

$$\varepsilon_\rho^{-1} = \varepsilon_\infty^{-1} - \varepsilon_0^{-1}, \tag{2.90}$$

and

$$I^{ij}(Q) = \oint dz \oint dz' \chi_i(z)\chi_j(z) e^{-Q|z-z'|} \chi_i(z')\chi_j(z'), \tag{2.91}$$

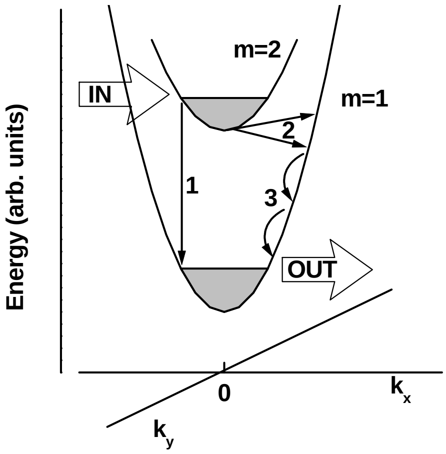

Figure 2.15: Schematic illustrations of the main inter-/intra-subband events crucial for the QCL operation. Arrows "IN" and "OUT" indicate correspondingly the processes of tunnelling in the $E_2$ state and tunnelling/scattering out of the state $E_1$. Arrow 1 indicate the photon assisted intersubband transition. Arrows 2 indicate possible electron intersubband scattering. Arrow 3 is a subsequent carrier relaxation within the ground subband (refereed also as a carrier plasma cooling).

where $E_{i,j}$ are the energies of correspondent states at $\mathbf{k}_{i,j} = 0$, $m_e^*$ is the electron effective mass, $\Omega_{\mathrm{LO}}$ is a frequency of LO-phonon, $\theta$ is an angle between vectors $\mathbf{k}_i$ and $\mathbf{k}_j$, $\varepsilon_\infty$ and $\varepsilon_0$ are the high-frequency and static relative permittivities of the heterolayer, $\chi_{i,j}$ are the envelope wave functions of correspondent states.

The electric field transient measurements (117) and the femtosecond four-wave mixing study (62) report an ultrafast 100-500 fs decays for the resonant coherent transitions. This is the notably faster process, than intersubband relaxation with a transition rate of $\sim 1ps$ (118; 119), determined by the intersubband scattering with the LO-phonons.

Speaking about the intersubband relaxation times it worth to mention, that being of the 1 ps order of magnitude they do, however, significantly scale with the intersubband energy spacing, see Fig. 2.16. Even though LO-phonon scattering rates are expected to scale with effective mass for different QW materials (116), experimental intersubband carrier relaxation times for both materials seems to follow closely the same trend when intersubband energy spacing increased. With increased intersubband energy spacing the number of intrasubband scattering events, which an electron needs to perform before it reaches the bottom of subband, increases proportionally to the energy spacing. Consequently the input of intraband relaxation processes into the population dynamics

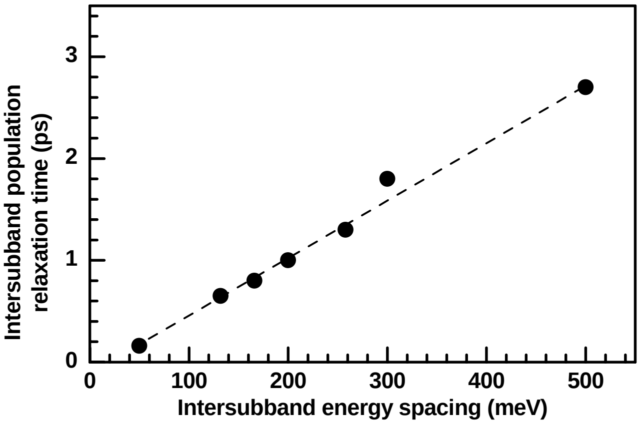

Figure 2.16: Some recent experimental results (120; 115; 121; 122; 119) on the intersubband relaxation time vs intersubband energy spacing (full circles) for the GaAs and $In_{0.53}Ga_{0.47}As$ QWs. Dashed line is drawn for eyesguide.

rises up. Asano *et al.* proposed the empirical expression for the intersubband population relaxation time which account for the intrasubband relaxation (115):

$$\tau(E_{ISB}) = \tau_{inter}(E_{ISB}) + \frac{E_{ISB}}{\hbar\Omega_{LO}}\tau_{intra}, \tag{2.92}$$

where $\tau(E_{ISB})$ is the resulting intersubband relaxation time, $\tau_{inter}(E_{ISB})$ is the time of intersubband scattering, $E_{ISB}$ is the intersubband energy spacing $\hbar\Omega_{LO}$ is the energy loss per scattering event (LO index denotes scattering by LO-phonon which is the most relevant scattering at low doping levels), $\tau_{intra}$ is the time of the single scattering event within the subband (~0.1 ps for LO-phonon scattering). For intersubband transitions with a small subband spacing (1–$2\hbar\Omega_{LO}$) the second term in the expression 2.92 vanishes, and the population relaxation time for the ground state becomes of ~0.2–0.3 ps (120). When the intersubband spacing becomes smaller than $\hbar\Omega_{LO}$, the population relaxation time increases. This happens because the intersubband scattering assisted with a single LO-phonon emission becomes forbidden.

## 2.4 Introduction into intersubband QCLs design

### 2.4.1 QCL design outlook

In this section we describe the principles of the QCL operation. It consists of seven subsections, which describe different ways to achieve the population inversion in the active region. Classification of different designs, which we are going to use, is aimed to reflect different approaches to achieve the population inversion, and does not follow the chronology of individual inventions.

Two subsections (2.4.2 and 2.4.5) review the population inversion approaches via fast depopulation of the lower lasing state. This can be done via resonant LO-phonon scattering (subsection 2.4.2) or through the miniband transport carrier escape (subsection 2.4.5).

Subsections 2.4.6 and 2.4.4 review the population inversion approaches via separation of the lasing transition and carrier escape (tunnelling out the active region) in $\overrightarrow{k}$-space. This can be done either in $k_{x,y}$-space in a single quantum well active region design (subsection 2.4.6) or in $k_z$-space in a superlattice active region design (subsection 2.4.4).

And the last subsection (2.4.7) describes the function of injector region.

### 2.4.2 Depopulation of the lower state via the resonant LO-phonon scattering

Depopulation of the lower lasing state via the resonant single LO-phonon scattering is probably the most common QCL active region design (2; 123; 124; 125; 126; 127; 128; 129; 130). The population inversion is provided by fast depopulation of the state ***1*** through the resonant LO-phonon scattering into the state $\boldsymbol{1'}$ (see Fig. 2.17). Some advanced designs (131; 124) use even two LO-phonon scattering in a sequence, which improve device performance. Such extension of the resonant single LO-phonon scattering depopulation of the lower lasing state leads to a reduced thermal backfilling of the lower state, and hence to the high temperature operation (131; 124). But the bottom line of all of them is the same: the resonant LO-phonon assisted depopulation of the lower state. Within this design approach one can distinguish two representative cases: "diagonal" and "vertical" transition active regions.

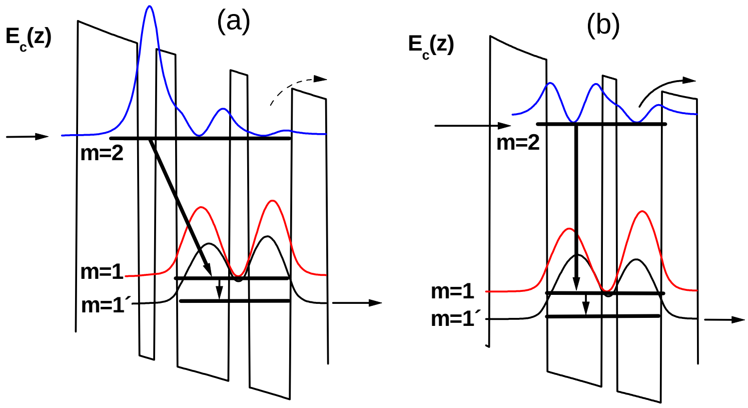

Figure 2.17: (a) Conduction band edge profile and the probability distributions for three QW active region design with diagonal transition. (b) The same for two QW active region design with vertical transition. The horizontal arrows indicate tunnel injection into and out of the well, and the vertical lines indicate transitions between the subbands .Thick arrow is both the resonant transition with photon emission and intersubband scattering. Small vertical arrow is a resonant intersubband LO-phonon scattering (by design).

### Diagonal transition active region design

Figure 2.17 (a) illustrates the conduction band energy profile in the $z$-direction of the "diagonal" transition QCL active region under operating bias. Thick arrow indicates both the resonant transition with photon emission and the intersubband scattering. Vertical arrow represents the resonant LO-phonon assisted intersubband scattering. Fast carrier tunnelling $(\tau \sim 0.2\text{ps})^{-1}$ through the injection barrier provides the efficient filling of the level *2*. The key-feature of such a design is a reduced spatial overlap of the upper lasing state $m = 2$ and the lower state $m = 1$. The lasing transition between them occurs through the photon-assisted tunnelling. The "diagonal" nature of the laser transition decreases the escape rate of carriers from state 2 into the continuum (dashed arrow), thus enhancing the injection efficiency. At the same time the reduced spatial overlap of the $m = 2$ and $m = 1$ states decreases the *2*-to-***1*** intersubband scattering rate and this way increases the lifetime of the upper lasing state up to a few picoseconds (2; 132).

Thus the "diagonal" transition active region design provides (i) the high population inversion and (ii) the low carrier escape rates from the upper lasing state into the classical continuum of states above the barriers. Such a design strategy was exploited in the very first QCL (2). The drawback of the "diagonal" transition design, however, are

(i) the reduced gain due to reduced spatial overlap of the states ***1*** and ***2*** and (ii) the broad gain spectra due to the increased influence of heterointerface roughnesses.

**Vertical transition active region design**

Figure 2.17 (b) shows the two QW active region design, which localizes both, the upper state 2 and lower state 1 essentially in the same wells. Such a design gives narrower gain spectra, comparing to the similar "diagonal" transition design (Fig. 2.17 (b)) due to the reduced influence of the heterointerfaces and the higher gain due to a huge spatial overlap of the states. The drawback of the "vertical" transition design is a weaker confinement of excited state in QWs and, consequently, higher probabilities of the carrier escape into continuum (bowed arrow in Fig. 2.17). This problem, however, can be overcome with a specific design of injection region (125), which will be described in subsection 2.4.7.

**High temperature operation and the "bottleneck" effect**

At cryogenic temperatures the concentration of LO-phonons in semiconductor is negligible. So, one can exclude the thermal backfilling of the state $m = 1$ from $m = 1'$. However, at elevated temperatures the carriers are scattered back into $m = 1$ state (thus, reducing the population inversion between the $m = 2$ and $m = 1$ states) with the rate proportional to the population of the $m = 1'$ state. The latter is defined by the tunnelling escape rate into the injector region. Experimentally obtained values of the tunnelling escape rate (127) of $\approx$2 ps$^{-1}$ is much smaller than the LO-phonon scattering rate from $m = 1$ to $m = 1'$. Thus, tunnelling out of the active region becomes to be a "bottleneck" for the lower lasing state depopulation. The high temperature operation of QCLs, however, is very desirable for application. Thermal backfilling effect is reduced by double-LO-phonon resonant depopulation of the lower lasing state (131; 124), as briefly mentioned above. Novel "bound-to-continuum" design, specially developed for the high temperature operation (133), is described in subsection 2.4.5.

### 2.4.3 Constant population inversion design

**Laser action by tuning the oscillator strength**

Figure 2.18 shows the QCL design, where the lowest state ***2*** of the injector miniband ***I*** is far below the first excited state ***3*** in the single QW active region under operating electric field. Laser action takes place between the injector state ***2*** and the ground state ***1*** of the single QW active region. The states are ***2*** and ***3*** are completely decoupled. In contrast to the diagonal transition QCL design described in subsection

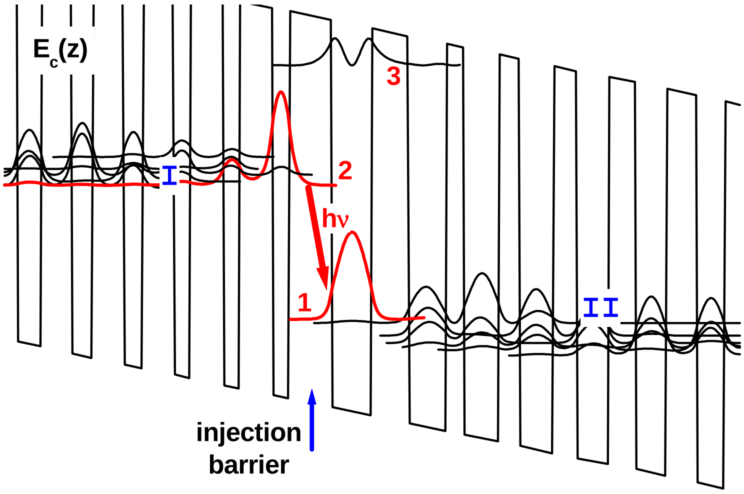

Figure 2.18: Illustration of the conduction band edge profile and the carrier probability distributions in the constant population inversion active region design.

2.4.2, the present design: (i) does not employ the resonant LO-phonon scattering depopulation of the lower lasing state, (ii) includes significantly thicker injection barrier, and (iii) provides extremely small overlap of the upper lasing state ***2*** and the lower lasing state ***1***. The lower lasing state ***1*** is depopulated exclusively due to the carrier tunnelling into the miniband of states, ***II***, of the next injector stage. Correspondent carrier lifetime in the state ***1*** is of the order of 0.5 ps (134) and depends very weakly on the applied electric field. The injector state ***2*** has a lifetime of tens picoseconds. So, the huge population inversion is constantly provided. The gain, however, depends strongly on the applied field. As the field increases (i) the energy separation of the states 2 and 1 increases due to increased potential drop between the two states (ii) the spatial overlap of the states ***1*** and ***2*** increase. Thus the tuning factor in the present design, unlike in all the other designs, is a gain (or, in another words, the dipole matrix element of ***2***-to-***1*** transition). When the threshold gain is achieved, the lasing action based on the photon assisted tunnelling between the states ***2*** and ***1*** is set on. A remarkable feature of the present design is the strong field dependence of emission wavelength (≈240 $\text{cm}^{-1}$ total tuning range) (134), which has a huge application potential for the sensing of gases and liquids.

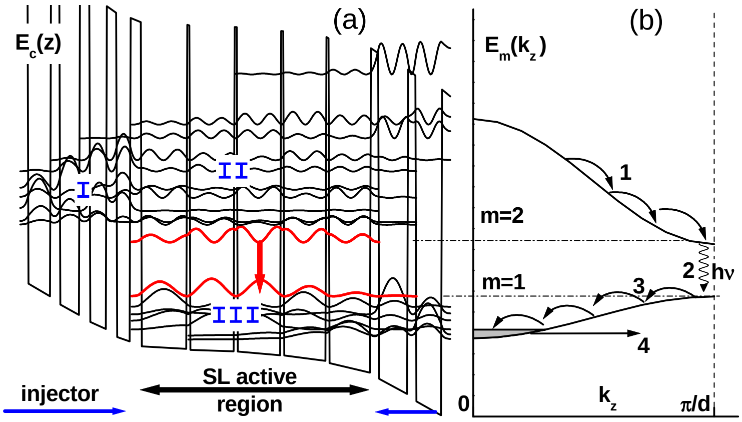

Figure 2.19: (a) Conduction band edge profile and manyfold states of InGaAs-InAlAs superlattice active region QCL. Appropriate bending of the conduction band edge profile is achieved either by the uniform doping of the active region superlattice (135), or by the local doping close to the injection barrier (136; 137). (b) Ground and first excited minibands energy dispersions in $k_z$-plane. Arrows indicate the individual processes: 1 and 3 are intrasubband carrier relaxation, 1 photon emission process, 4 miniband transport out the active region.

### 2.4.4 Local $k_z$-space population inversion

**Superlattice active region**

Single period SL-active-region under operating electric field is sketched on fig. 2.19 (a). The first excited miniband (II) of SL-active-region is strongly coupled with the miniband (III) of ground states in injector (formed under electric field), thus, providing fast electron injection. Being within the miniband II carriers quickly relax to the bottom of the miniband (see fig. 2.19 (b)), and finally reside in $k_z = \pi/d$ location in $k$-space. In contrary, carriers in the ground state miniband (I) of active region are scattered to the $k_z = 0$ location in $k$-space (see fig. 2.19 (b)). Thus, in $k_z = \pi/d$ population inversion is obtained simply due to the intraminiband relaxation within the SL itself. Such a phenomenon is referred as a "natural" population inversion (138). A distinctive feature of such an active region is the high oscillator strength of direct miniband transition at $k_z = \pi/d$ (see subsection 2.2.3 for details). This is an important factor for achieving the threshold gain. High power and room temperature operation of SL-active-region QCLs are achieved (137; 139). The down-side of SL-active-region QCL design is a high threshold current at high operating temperatures, which is, likely, due to thermal escape of the carriers from the upper miniband ***II*** into

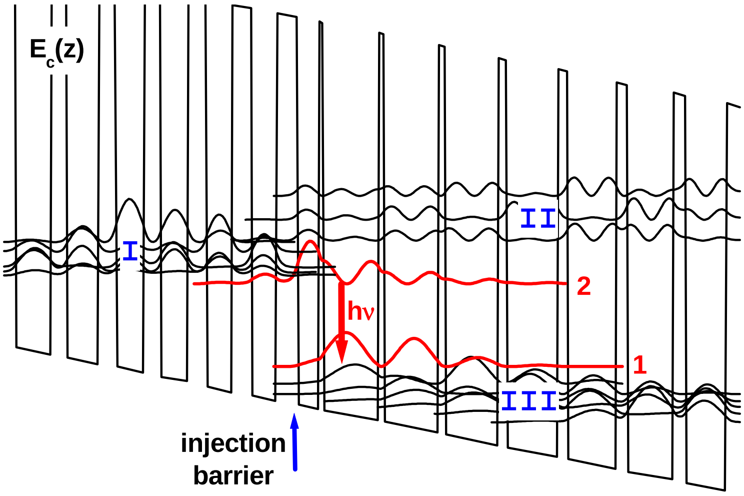

Figure 2.20: Illustration of the conduction band edge profile and the carrier probability distributions in the bound-to-continuum active region design.

continuum. Consequently, in material systems with high CBO (say AlAs-GaAs) high temperature operation is extremely improved (140).

### 2.4.5 Lower state depopulation via miniband transport carrier escape

#### Bound-to-continuum active region design

Bound-to-continuum QCL design (depicted on fig. 2.20) utilizes both advantages: (i) high injection efficiency of diagonal transition 3-QW laser design and (ii) fast depopulation of lower lasing state of SL QCL design. In bound-to-continuum design there is no sharp distinction between the active- and injector-region. The miniband ***I+III*** of the ground states formed by a chirped superlattice extends through the whole single period with some narrowing close to the injection barrier. The upper lasing state is introduced with a narrow QW within injection barrier and locates within the minigap of the chirped superlattice (i.e. between the miniband ***III*** and ***II***). Because of sufficient separation (∼2 LO-phonon energies (133; 141)) of upper lasing state ***2*** and the miniband of excited states ***II***, the thermal carrier escape into classical continuum trough the miniband ***II*** is suppressed. Fast intraminiband scattering effectively depopulate the lower lasing state ***1*** with the rate of $(0.2\ \mathrm{ps})^{-1}$ (133). Fast miniband transport is maintained all through the single stage of QCL, so, there is no "bottleneck" effect expected, contrary to the two-/tree-quantum well

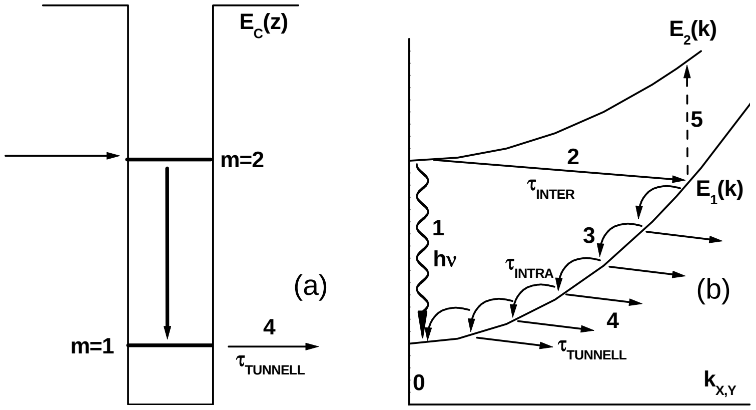

Figure 2.21: (a) single quantum well active region. Horizontal arrows indicate tunnelling injection into and out the well. Vertical line indicate transitions between the subbands. (b) ground and excited states energy dispersions in $k_{X,Y}$-plane. Arrows indicate the individual processes within the intersubband transition: 1 resonant transition with photon emission, 2 nonradiative intersubband scattering (most likely the LO phonon scattering), 3 intrasubband relaxation (most likely the LO phonon scattering), 4 tunnelling events out the well, and 5 photon reabsorption.

active region design. And consequently, high device performance at room temperature is achievable (133; 141).

### 2.4.6 Local $k_{x,y}$-space population inversion

**Single quantum well active region**
Single quantum well active region QCL, published 1996 (127), represents the contradictive, at the first look, design of lasing transition using only two subbands within a single quantum well (see fig. 2.21(a)). From the simple reasoning of thermodynamical equilibrium and rate-equations between two energy levels, the population inversion in such a system is impossible. Situation changes, however, when we consider a subband dispersion in $k$-space (see fig. 2.21(b)), and look more close into the carrier relaxation dynamics. Critical issues here are: (i) the bulk band nonparabolicity which leads into differen curvatures of two energy dispersions curves (see fig. 2.21(b) and, consequently, different intersubband transition energies for different $k$. (ii) the non-thermal electron distribution within the lower subband (142). (iii) High energy separation of subbands. So the nonparabolicity effect is stronger and the intrasubband relaxation takes longer.

First, due to the band nonparabolicity, the reabsorption spectrum of the carriers at high $k$ does not overlap with spontaneous emission spectrum of the carriers at low $k$. So the reabsorption losses are small. Second, due to the long intrasubband relaxation scenario (arrow 3 fig. 2.21) a part of scattered (arrow 2 fig. 2.21) carriers tunnel out the well (arrow 4 fig. 2.21) before they reach the bottom of the ground subband. In another words, they do not finally input into the local population at $k = 0$. So, the local population at the very bottom of the ground subband is decreased comparing the hypothetic case of an instant intrasubband relaxation. Under such a conditions it becomes possible to obtain local population inversion within a $k = 0$ location. And laser actin comparable with double quantum well active region design was demonstrated (127).

### 2.4.7 QCL injector region

The role of injector region is to provide fast carrier transport in between the active regions. Therefore it is usually designed so, that the states of individual wells get coupled into the miniband under designed operation electric field. Carrier transition between injector and active region is done by resonant tunnelling or miniband transport, depending on the particular design (see subsection 2.4.1).

From the macroscopic point of view injector region can be also viewed as a digital alloy with a linear grading of conduction band edge offset. So that under a certain applied electric field the conduction band profile becomes flat, thus allowing effective carrier transport.

But there is one quantum mechanical phenomenon, which can not be understood within the digital alloy approach, namely, carrier reflection from the minigap of states in SL (143). In QCLs the minigap of states, formed in injector region is used to enhance the confinement of upper lasing level, which increase the lifetime of the upper lasing state and therefore leads to the outstanding device performance (125; 126; 127; 124; 123). To fulfil simultaneously the flat miniband condition under applied electrical field and minigap formation condition, one need to adjust the thickness of every well and barrier rather then just to vary the SL duty cycle. Important issue is to achieve the minimum of transmittance at the energy of upper lasing state. This is done (125; 144; 145; 146) by satisfying the Bragg reflection conditions for each pair of well and barrier:

$$k_w l_w + k_b l_b = \pi, \tag{2.93}$$

where $l_{b/w}$ is the barrier/well thickness. $k_{b/w}$ is the electron wavenumber:

$k \equiv 2\pi/\lambda = \sqrt{2m^* E/\hbar^2}$, $E$ is the energy separation of the upper lasing state and conduction band edge in corresponding material.

Another critical parameter of injector design is doping level and profile. Usually, donors are located away from the active region (i.e. in the middle of injector region) to avoid additional broadening of the gain spectra (due to ionized impurity scattering). Doping level is usually chosen so, that the Fermi level is located at the neighborhood of the conduction band edge of the well material. Systematic study of device performance and emission wavelength of GaAs-based QCL was recently published by Giehler *et al.* (147).

Critical issue in injector design is to provide a sufficient carrier energy loss of a few LO-phonon energies, when travelling from a one active region to another (148). This avoids thermal backfilling of the lower lasing state.

## 2.5 Summary of chapter 2

To summarize chapter 2, we have reviewed the following topics:

(i) Envelope Function Approximation in application to quantum wells and quantum well superlattices; formation of quantized states and minibands in quantum wells and superlattices; influence of strain on material parameters and electron states; influence of magnetic field on quantized states;

(ii) intersubband absorption phenomenon; intersubband absorption lineshape, oscillator strength, selection rules; influence of band non-parabolicity and carrier density on the lineshape and spectral position of intersubband absorption;

(iii) basic issues of vertical electron transport in semiconductor superlattices and intersubband scattering dynamics;

(iv) basic principles of quantum cascade laser operation, and classical approaches of intersubband laser active region design.

# Chapter 3

# InGaAs-InAlAs material system for short-wavelength QCLs

## Preface

In present chapter we want to explore the limits of utility of strain-compensation in InGaAs-InAlAs/InP QCLs. Our activity will be focused mainly on highly strained $In_{0.70}Ga_{0.30}As$-AlAs material combination on InP for QCL application.

Our motivation to study $In_{0.70}Ga_{0.30}As$-AlAs material system is to utilize high conduction band offset of this material combination for achieving the short-wavelength intersubband laser.

Our goal is to achieve QCL action with as short as possible emission wavelength.

QCL performance is sensitive to many parameters, like: material quality, precise engineering of ISB transitions, active region design, and processing steps. To solve the challenge of a new short-wavelength QCL iteratively we first demonstrate the growth and ISB transitions engineering on the new $In_{0.70}Ga_{0.30}As$-AlAs material system on InP. There are only few studies of such a material combination towards the short-wavelength ISB application in literature coming from the other groups (149; 150; 151). And all of them are done on the uncoupled multiple quantum wells. Such a design is pointed towards the short wavelength QWIP application. In contrary, we demonstrated short-wavelength ISB transitions on coupled $In_{0.70}Ga_{0.30}As$-AlAs heterostructures: double quantum wells and superlattices, which are close prototypes to QCL active region.

Then grow and fabricate the known QCL design after Ref. (131) on $In_{0.54}Ga_{0.46}As$-$In_{0.51}Al_{0.49}As$ material system (called test-structure hereafter). Successful fabrication of the test-structure assure the deep understanding and the high performance of growth and processing steps of QCL.

After the analysis of the QCL test-structure design we did design our original QCL active region on the new $\mathrm{In_{0.70}Ga_{0.30}As}$-AlAs material system. After device fabrication step we obtained laser action in 3.7-4.2 $\mu$m spectral range.

At the end of the chapter we discuss the laser performance and possible fields of its application.

## 3.1 Material growth and basic characterization

All the structures discussed in this thesis were grown by GSMBE (152). Special feature of GSMBE is that group V elements are produced by thermal cracking of gases, usually hydrides ($\mathrm{AsH_3}$, $\mathrm{PH_3}$, $\mathrm{NH_3}$). Cracking produces a number of species, for instance:

$$\begin{aligned} 2\mathrm{AsH_3} &\longrightarrow 2\cdot(\mathrm{AsH\text{-}} + 2\mathrm{H\text{-}}); \\ \ldots &\longrightarrow 2\cdot(\mathrm{As\text{-}} + 3\mathrm{H\text{-}}); \\ &\longrightarrow 2\cdot(\mathrm{As\text{-}} + \mathrm{H\text{-}} + \mathrm{H_2}); \\ &\longrightarrow \mathrm{As_2} + 3\mathrm{H_2}. \end{aligned} \tag{3.1}$$

At fixed conditions (temperature, pressure) one of cracking scenarios 3.1 can dominate. Our GSMBE is equipped with low pressure cracking cell. Within the used range of cracking temperature of 830-900 °C it produces mostly AsH- (and/or PH-) radicals, as revealed by in-situ mass-spectrometry. Higher cracking temperatures (900-1000 °C) and high cracking pressures are known to produce mostly $\mathrm{As_2}$ dimers (153; 154; 155). In any case, pressure in GSMBE is mostly defined by partial pressure of H- and $\mathrm{H_2}$ species, which are more difficult to pump out than $\mathrm{As_2}$, As-, .... Because of the finite pumping capacities, significantly lower fluxes of group V elements can be achieved in GSMBE comparing the solid source MBE.

Optimal MBE growth conditions were achieved by adjusting of V/III flux ratio for each growth temperature. This has allowed to obtain high quality InGaAs-InAlAs heterostructures within the 520-400 °C range of growth temperatures. While for the lattice matched InGaAs-InAlAs structures on InP 500-520 °C growth temperature range seems to be optimized and widely used (156; 154; 157); lower growth temperatures of 450-400 °C, however, appeared to be necessary to grow coherently highly strained $\mathrm{In_{0.70}Ga_{0.30}As}$-AlAs heterostructures (158). Growth mode and material quality was controlled *in-situ* by reflection high-energy electron

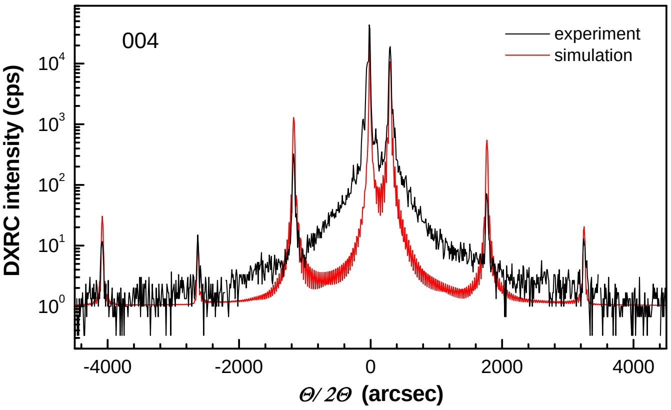

Figure 3.1: DXRC of 50 period 7.1 nm $In_{0.55}Ga_{0.45}As$ - 5.6 nm $In_{0.46}Al_{0.54}As$ superlattice, on InP. Solid line is experimental spectrum, dotted line is a simulation result.

diffraction, RHEED, pattern observation and *ex-situ* by X-ray diffraction and photoluminescence measurements. During InGaAs and InAlAs growth on InP in the substrate temperature range of 400-520 °C sharp $2 \times 1$ RHEED pattern was usually observed during the layer deposition as well as during the growth interruptions. The higher was internal strain within a heterostructure, the lower growth temperature was used to maintain sharp RHEED pattern. No layer quality degradation was observed at 400 °C growth temperature, likely, due to low V/III species flux ratio (close to stoichiometric) used.

Measured double crystal X-ray rocking curves, DXRC, of superlattice structures (see example on fig. 3.1) coincide very well with simulation based on dynamic scattering theory, indicating flat heterointerfaces formation. Doping level was controlled by capacitance-voltage, CV, profiling and Hall-effect measurements, and corresponds well to the flux of Si dopant. All the structures reveal intensive room temperature, RT, photoluminescence, PL, (fig. 3.2) and narrow , down to 12 meV, low temperature, LT, PL (fig. 3.3).

As long as strain compensation condition is fulfilled, Nomarski phase contrast microscope, NFCM, images reveal smooth dislocation free surface morphology.

An extreme case of strain-compensated heterostructure on InP is InAs-AlAs well-barrier combination. Two-dimensional growth of up to 16 monolayer thick single InAs QW within $In_{0.52}Al_{0.48}As$ matrix (159; 160) and up to 11 monolayer thick single InAs QW within $In_{0.53}Al_{0.47}As$ matrix (161) was demonstrated by Tournie *et al.* However, in case of short period InAs-AlAs superlattices many studies (see for example Ref. (162)

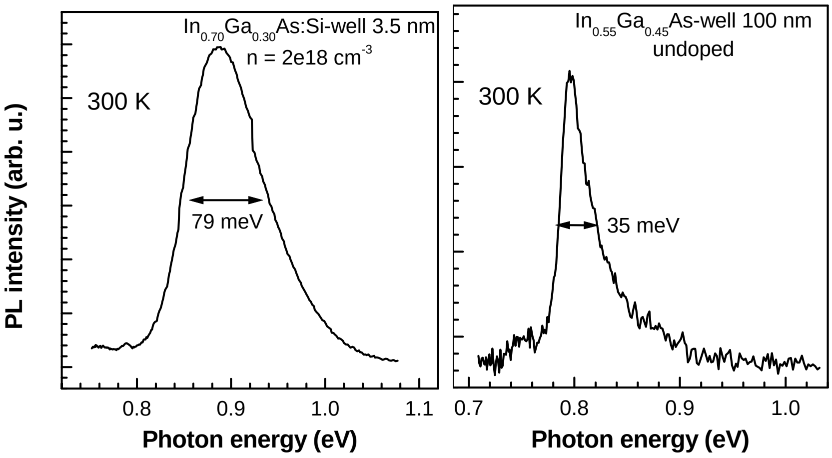

Figure 3.2: 300 K photoluminescence spectra of 3.5 nm $In_{0.70}Ga_{0.30}As$:Si - 5.7 nm $In_{0.40}Al_{0.60}As$ 50 period SL (left hand side); and 10 nm undoped $In_{0.55}Ga_{0.45}As$ QW with 20 nm $In_{0.50}Al_{0.50}As$ barriers (right hand side) grown on InP.

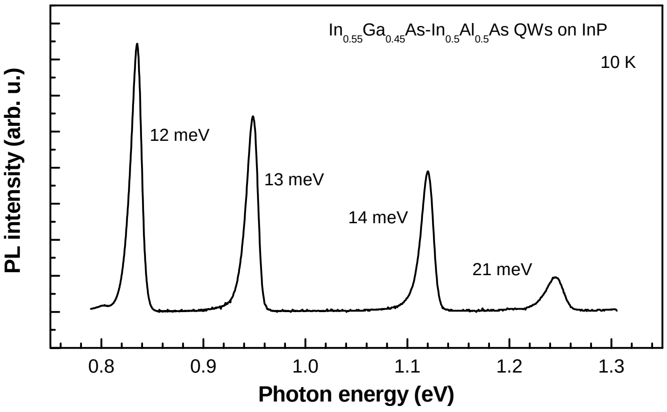

Figure 3.3: 10 K photoluminescence spectra of 10, 3, 1.5, and 0.5 nm $In_{0.55}Ga_{0.45}As$ QWs with 15 nm $In_{0.5}Al_{0.5}As$ barriers in between, grown on InP.

and references therein) report on lateral composition modulation, i.e. three dimensional growth morphology for wells and barriers as thin as 2 monolayers each.

We have grown such a superlattice-samples with GSMBE and observed the three-dimensional growth mode at growth temperatures as low as 400, 350, and 300 °C. In contrary, the short period InGaAs-AlAs superlattices with $approx30\%$ Ga content were grown two-dimensionally and showed a good performance in terms of intensive photoluminescence, sharp X-ray pattern, and intensive intersubband absorption, as described below in section 3.2.

The theoretical critical thickness (163) of the strained III-V crystalline layer determined for the conditions of thermodynamic equilibrium cam be found form equation (164; 153)

$$\frac{0.22 \times ln(h_{crit})}{h_{crit}} = \epsilon, \tag{3.2}$$

where $\epsilon$ is the value of strain (see Eq. 2.30), and $h_{crit}$ is the critical thickness in angstroms. For the 3.9% strain of AlAs layer grown on InP, for example, we obtain the critical thickness value of approximately 5 monolayers.

The MBE growth conditions, however, are far from the thermodynamical equilibrium. Therefore, the experimental values of the critical thicknesses are somewhat higher then these predicted by theory, and strongly depend on the growth conditions. For example, AlAs layers with thicknesses of 7 monolayers were grown pseudomorphically on InP (see section 3.2).

## 3.2 Short-wavelength intersubband transitions engineering

### 3.2.1 Near-infrared ISBT in InGaAs-AlAs QWs and SLs

**Preface (or Material choice)**

An ambiguous goal to engineer the shortest wavelength intersubband transition and to design the shortest wavelength ever QCL laser has driven our research last few years. One of the most important starting condition was decision on material choice. We have decided to extend the possible range of ISB transitions on InGaAs-InAlAs/InP material system by growing it strain-compensated on InP. Figure 3.4 depicts the positions of Γ-valley minima for InGaAs and InAlAs relatively the vacuum level for In content ranging from 0 to 1. Calculations were done using Model Solid Theory parameters (25), assuming that the layers are coherently strained on InP. Particular choice of In content in well and barrier was based on following two criteria: (i) to maximize Γ-valley edge offset and (ii) to maintain the zero net strain at target average well/layer thickness ratio. Because our final -and most challenging-goal is QCL, the target average well/layer thickness ratio should be defined by tentative QCL design. Choice was made for combined (often called as *digital alloy*) AlAs-$In_{0.55}Al_{0.45}As$ barriers and $In_{0.70}Ga_{0.30}As$ wells. High In content InGaAs wells were chosen rather than pure InAs, because in QCL active region one need to grow relatively thick (3-10 nm) wells together with thin ($\approx$ 1 nm) barriers. The thickest coherent two-dimensional InAs layers on InP substrates ever reported (159; 160) were as thick as 16 ML ($\approx$4.8 nm), which would be thick enough for the active region QWs. But to compensate the local strain one need to grow then thick barriers in active region, which reduce coupling between the ground electron states and thus vanishes the miniband transport. In the case of $In_{0.70}Ga_{0.30}As$-AlAs combination, both conditions of thick wells and thin barriers can be easy fulfilled as well as strain kept compensated. At the same time additional $In_{0.55}Al_{0.45}As$ insertions in barriers allow very flexibly manipulate barrier thickness in injector region in QCL designs and to space single quantum wells in test-samples, used for ISB absorption study. In chosen material combination we obtain (see Fig. 3.4) 1.33 eV band offset between InGaAs and AlAs; and 0.54 eV offset between InGaAs and InAlAs. Position of indirect valleys (X and L) will be discussed below in present chapter.

In following we present our study of intersubband absorption in strain-compensated $In_{0.70}Ga_{0.30}As$/ AlAs/$In_{0.55}Al_{0.45}As$ multiple quantum wells and superlattices grown on InP. We also present X-ray diffraction study, arguing that the layers are pseudomorphically strained and exhibit slight compositional grading of the interfaces. We demonstrate that owing to the high AlAs barriers, intersubband absorption can be tailored to wavelengths shorter than 2 $\mu$m. In some samples, a small, but non-negligible absorption is also observed with $s$-polarized light.

Intersubband transitions are now routinely used for optoelectronic devices such as quantum cascade lasers (QCL) and quantum well infrared detectors (QWIP) in the mid-infrared (wavelength = 3 $\mu$m - 20 $\mu$m) spectral range (165). Recently also a QCL in the far-infrared, at 87 $\mu$m, has been reported (6). Yet there is considerable interest to extend applications of intersubband transitions also to the near infrared (< 3

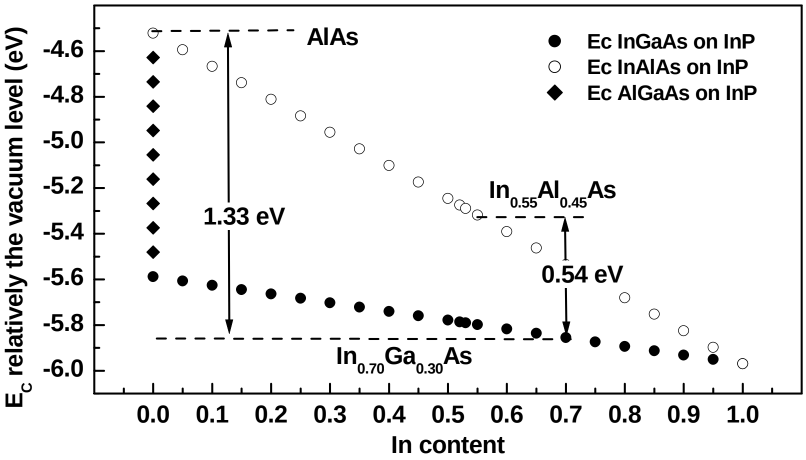

Figure 3.4: Positions of Γ-valley minima for (In,Ga)As, (In,Al)As, and (Al,Ga)As ternary alloys pseudomorphically strained on InP, calculated after (25).

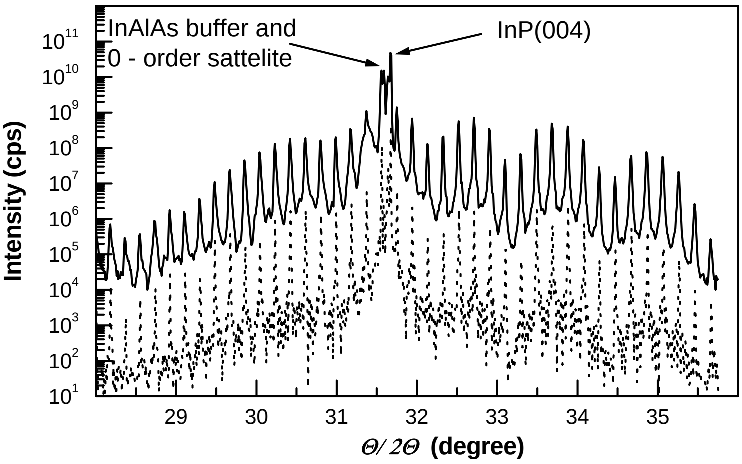

Figure 3.5: XRD pattern of the 7 ML $In_{0.7}Ga_{0.3}As/AlAs/In_{0.55}Al_{0.45}As$ MQW around the InP (004) reflex. Experimental data (solid line) and simulation (dotted line) using a model that includes interfacial compositional grading.

$\mu$m) and in particular to the 1.55 $\mu$m communication wavelength region. Such devices would offer very fast switching and modulation frequencies (166; 167) due to the fast intersubband relaxation in the sub-picosecond regime.

In the past few years short-wavelength intersubband absorption has been demonstrated in several novel material systems, such as GaN/AlGaN (168; 169; 170; 171) or ZnSe/BeTe (172). Yet it would still be preferred to employ common III-V technology based on GaAs or InP. In the GaAs/AlGaAs system the band offset at the Γ-point can be as large as 1.0 eV for pure AlAs, but the X-states in AlAs are much lower and can even drop below the GaAs quantum well state in narrow quantum wells (QW). This can be partly remedied by using strained InGaAs, which increases the band offset and also lowers the QW states. Short-wavelength intersubband absorption in this system has been reported by several groups and the Γ-X crossover has been observed (173; 174; 175; 176). On the other hand, lattice matched InGaAs/InAlAs on InP has a conduction band offset of 0.52 eV. Larger offsets can only be achieved in strained structures, which have for instance been employed in the shortest-wavelength QCL to date ($\lambda = 3.5$ $\mu$m) (5). InGaAs QWs on InP with pure AlAs barriers have - to our knowledge - only been investigated by one group (150). They observed absorption wavelengths as short as 1.55 $\mu$m as well as a strong, red-shifted intersubband absorption in the normally forbidden *s*-polarization. This has been an issue of extensive discussion in the literature (177), because other groups were able to observe only weak *s*-polarized signals (178). An alternative heterosystem lattice matched to InP is $In_{0.53}Ga_{0.47}As/AlAs_{0.56}Sb_{0.44}$, which has a very high band offset and is also promising for short-wavelength applications (179; 180).

In the present subsection we explore the potential of the InGaAs/AlAs system grown pseudomorphically on InP substrates for short-wavelength intersubband transitions. Our strategy is to use InGaAs quantum wells with a large In content, which are compressively strained: this provides deep QWs, a Γ-like ground state, and helps to compensate - together with a slightly compressively strained $In_{0.55}Al_{0.45}As$ buffer - the strain from the tensile strained AlAs barriers. When good overall strain compensation is achieved, thick multilayer structures can be grown pseudomorphically.

All samples were grown by gas-source molecular-beam epitaxy (GSMBE) on semi-insulating InP (001) substrates. To provide a smooth growth front a 200 nm undoped InP buffer was grown first at 465 °C followed by an undoped $In_{0.55}Al_{0.45}As$ buffer (480 °C) and the QW structures (400 °C). Two types of structures were grown, namely multiquantum wells (MQW) and short-period superlattices (SL). The MQWs consist of 30 periods of $In_{0.70}Ga_{0.30}As$ wells with various thicknesses (see

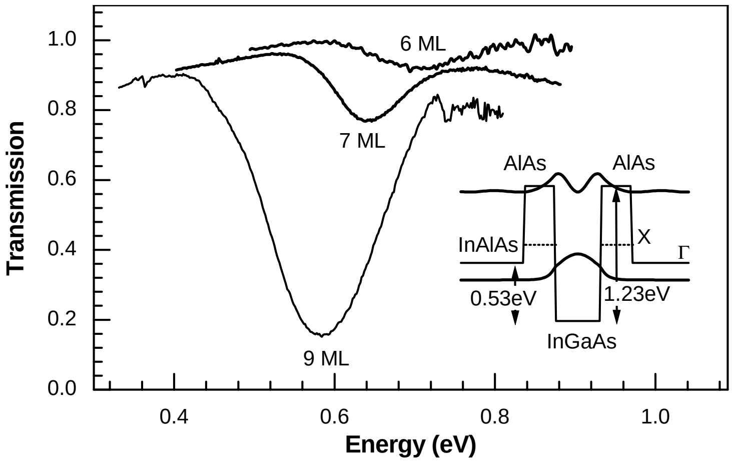

Figure 3.6: Transmission spectra of the $In_{0.7}Ga_{0.3}As/AlAs/In_{0.55}Al_{0.45}As$ MQWs with different InGaAs well widths. The inset shows the schematic conduction band diagram of the QW structure and calculated wavefunctions for the sample with 7 ML thick wells.

below) confined by 1.5 nm or 2.0 nm thick AlAs barriers. A 20 nm thick $In_{0.55}Al_{0.45}As$ layer is inserted between each period to compensate the large tensile strain caused by the AlAs layers. The SLs consist of 40 pairs of $In_{0.70}Ga_{0.30}As$ (4.2 or 3.3 nm) and AlAs (1.2 nm). In all cases the $In_{0.70}Ga_{0.30}As$ QW layers are Si doped (for details see below). A sketch of the conduction band alignment of the MQWs is shown in the inset of fig. 3.6 It should be noted that due to the high In content in the wells, the QW ground states are well below the X-states in the barriers. According to Van de Walle's model-solid theory (25), the conduction band offset between wells and barriers can be estimated to ≈1.3 eV (see Fig. 3.4). Considering only the high In content in the wells, one would expect an even higher offset, but part of it is compensated by the strain-induced shift of the band edges. Figure 3.4 sketches the positions of Γ-valley minima for (In,Ga)As, (In,Al)As, and (Al,Ga)As ternary alloys relatively the vacuum level. Calculations are done including the pseudomorphic strain on InP following (25), but without accounting for the effect of band bowing (181).

High-resolution X-ray diffraction (XRD) was performed at the European Synchrotron Radiation Facility (ESRF) in Grenoble (France). The diffraction pattern near the (004) reflex of a MQW sample with 7 monolayers (ML) thick $In_{0.70}Ga_{0.30}As$ QWs is presented in fig. 3.5 Using a dynamical simulation, the two peaks very close to the substrate peak (lower-angle side) can be identified as zero-order MQW peak and as originating from the $In_{0.55}Al_{0.45}As$ buffer, respectively. The tiny splitting indicates nearly perfect overall strain compensation, to better than 0.2%. The best fit (dotted line), however, is achieved by assuming interfaces which are not sharp, but rather compositionally graded by 1-2 ML. In addition, reciprocal space maps at the (224) and (115) reflections were employed to verify that the QW structures were grown fully pseudomorphic and no strain relaxation by generation of misfit dislocations occurred.

The intersubband absorption spectra were measured at room temperature with a Fourier transform infrared spectrometer using a multiple-reflection waveguide geometry fabricated by polishing two end facets at an 45° angle. fig. 3.6 shows the transmission spectra of three MQW samples with well thicknesses of 2.8, 2.2, and 1.9 nm, corresponding to about 9, 7, and 6 MLs, respectively. Plotted is the ratio of the $p-$ and $s-$polarized transmission, further normalized to the same ratio of an undoped InP substrate. The absorption peaks are observed at 0.58, 0.66, and 0.72 eV, respectively, the latter two corresponding to wavelengths shorter than 2 m. All experimental peaks occur at energies which are about 10-15% too low, when compared to a calculation in the framework of the effective mass approximation including nonparabolicity and strain-modified band edges (25). If we, however, assume a modified QW potential with a one-monolayer-thick interface layer having an intermediate composition between well and barrier layers, we can reproduce the experimental values of the peak energies. This is supported by the XRD measurements, which yield the best fit with such modified interface layers (fig. 3.5) as described above. Although low-temperature growth of the QW structures suppresses In segregation and interdiffusion across the heterointerfaces, some short-scale interface roughness during the growth of heavily strained layers may still develop (182), which effectively also yields a thin interface layer with intermediate composition.

Next we focus on the absorption strengths and widths. The observed absorption linewidths are relatively large (full width of 120-170 meV, i.e., relative linewidth of 15-20%), an observation which is quite typical for short-wavelength intersubband absorption [8]. It is caused by interface roughness and well thickness fluctuations, which have a significant influence in thin QWs, and also partly by nonparabolicity in connection with the high doping. The absorption strength should be proportional to the areal electron density. We note that the 9 and 6 ML samples are nominally doped $1{\cdot}10^{19}$ $cm^{-3}$ in the wells, whereas the 7 ML sample only $2{\cdot}10^{18}$ $cm^{-3}$. Thus the absorption decrease from the 9 to the 7 ML sample appears reasonable; however, the absorption of the 6 ML sample is by far too weak and cannot be explained by simple means (similar observations have been made in (173; 174)). A partial reason may be a

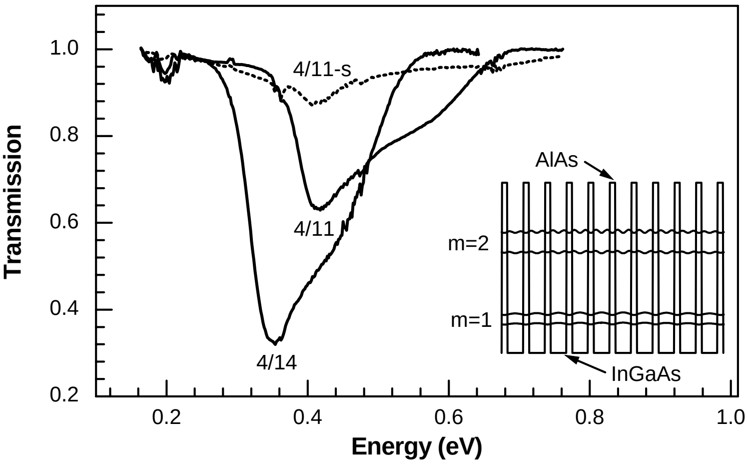

Figure 3.7: Transmission spectra of the two $In_{0.7}Ga_{0.3}As/AlAs$ superlattices with 14 and 11 MLs well widths, respectively. In addition, the pure $s$-polarized spectrum is plotted for the 4/11 SL (dotted). The inset shows the conduction band profile of the 4/11 SL with the square moduli of the wavefunctions at the first two minibands boundaries. Observed typical for superlattices two-component-like lineshape is due to the oscillator strength extrema at $k_z = 0$ and $k_z = \pi/d$.

smaller oscillator strength since for this sample the upper state is already in the continuum above the barriers (the inset in fig. 3.6 shows the 7 ML sample with still marginal confinement); the main cause why the carriers do not participate in the absorption process, remains unclear however.

In fig. 3.7 the transmission spectra of the two superlattice samples are presented. They have the same barrier width (1.2 nm or 4 MLs), but different well thicknesses of 4.2 nm and 3.3 nm (14 and 11 MLs), respectively, and are doped in the wells with $n = 2 \cdot 10^{18}$ cm$^{-3}$. Plotted is again the ratio of $p$- to $s$-polarized signals normalized to a substrate signal as described above. The spectra clearly exhibit the asymmetric shape which is typical for strongly coupled superlattices, due to the variation of the oscillator strength along the SL wavevector $k_z$ (183; 54). The peak and the shoulder correspond to the transitions at the center ($k_z = 0$) and the edge ($k_z = \pi/d$) of the mini-Brillouin zone, respectively (see inset of fig. 3.7). The latter transition can be observed, because the first miniband is fully occupied due to the high doping density. For the 4/11-ML superlattice the absorption extends up to nearly 0.7 eV, roughly 1.8 $\mu$m wavelength. The experimental and calculated absorption profiles coincide reasonably if we include again a compositionally graded monolayer at the interfaces.

An additional, third spectrum is displayed in fig. 3.7 (dotted line). It is the pure *s*-polarized signal of the 4/11 ML superlattice, divided by the *s*-polarized signal through an undoped substrate. It appears rather convincing that there is some finite intersubband absorption remaining in *s*-polarization, 10-20% the intensity of the *p*-polarized absorption (the sharp features at 0.37 eV stem from organic molecules probably on the sample holder). In some of the other samples, there is indication of similar behavior (not shown), but it cannot always be unambiguously separated from the background. These observations do not support the previous work of Smet *et al.* (150), who observed a comparable size of *s*- and *p*-absorption, but are rather consistent with later studies by Liu (178), who showed 3% s-polarized absorption in $In_{0.1}Ga_{0.9}As$ QWs. Theoretical work predicts some small *s*-polarized absorption resulting from $k \cdot p$ coupling to higher bands (94; 184; 91). Presently there are no detailed calculations for the exact structures investigated here, but due to their high In content and the large strain it appears not unreasonable to assume a modest relaxation of the intersubband selection rule, resulting in an "forbidden" absorption strength as observed in the present work.

In conclusion, we have studied intersubband absorption in highly strained, but strain-compensated InGaAs/AlAs multiquantum well and superlattice structures, with absorption wavelengths below 2 $\mu$m. Small *s*-polarized absorption is also observed, which however does not appear to contradict theoretical considerations.

### 3.2.2 Near Infrared ISBT in InGaAs-AlAs DQWs

In this subsection we present a comprehensive approach of engineering the short wavelength intersubband transitions in coupled $In_{0.70}Ga_{0.30}As$-AlAs-$In_{0.55}Al_{0.45}As$ double quantum wells (DQWs). One straight-forward advantage of such a design is the ease of strain balancing, comparing the case of a single QW. That is because the ratio of total QW width to the total AlAs barrier width increases.

All structures considered here were grown using gas-source molecular-beam epitaxy on a slightly compressively strained $In_{0.55}Al_{0.45}As$ buffer on low-doped n-type InP:Sn or semiinsulating InP:Fe substrates. Typical growth conditions and characterization are described in previous subsection.

The heterostructures consist of 30 periods of AlAs - $In_{0.70}Ga_{0.30}As$ - AlAs - $In_{0.70}Ga_{0.30}As$ - AlAs ($1.5/L_{WW}/0.9/L_{NW}/0.9$ nm) DQWs, each period separated by 15 nm $In_{0.55}Al_{0.45}As$ . The width of the narrower QW, $L_{NW}$, is varied as 2.8, 2.6, 2.4, and 2.4 nm for samples A28, A26, A24 and A24-6 respectively. The width of the wider QW, $L_{WW}$, was 3.2 nm for all the samples, except the A24-6, where $L_{WW}$ was changed to

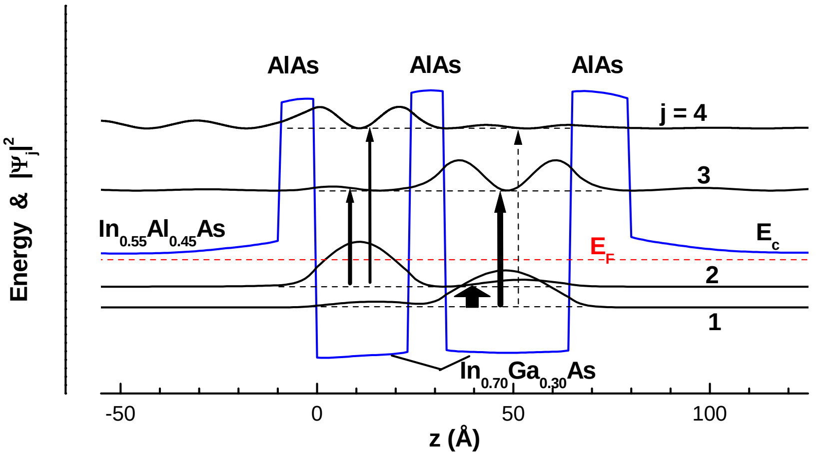

Figure 3.8: Illustration of strain-compensated $In_{0.70}Ga_{0.30}As/AlAs/In_{0.55}Al_{0.45}As$ DQW conduction band profile, $E_c$, with square moduli of the wavefunctions of ($j$=1, 2, 3, and 4), states localized in $In_{0.70}Ga_{0.30}As$. The dashed line represents the Fermi energy, $E_F$. Arrows indicate the individual ISBTs to be considered. Calculated oscillator strengths for depicted transitions are listed in table 3.1.

2.6 nm.

Conduction band profile and confined state wavefunctions were obtained using self-consisted Schrödinger-Poisson calculations and input parameters from the Model Solid Theory (25). Figure 3.8 depicts the conduction band edge, $E_c$, and the calculated probability function for confined electronic states in a DQW sample A24. Fermi energy level, $E_F$, is represented by a dashed line. Arrows indicate the correspondent intersubband transitions to be considered.

Table 3.1 summarizes the well widths, calculated oscillator strengths, and the energy spacing between the calculated Fermi energy and the second confined state in DQW for studied samples. When coupling the narrow well, NW, of various thicknesses with the wide well, WW, of 3.2 nm, than oscillator strength, $f$, calculations (see table 3.1) reveal that (i) in the case of thicker NW we obtain an increased $f$ for 1-4 transition, and (ii) in the opposite case of thinner NW we obtain an increased $f$ for 2-4 transition. Beside that, surrounding of the NW by a WW increases the spatial localization of state 4. Consequently stronger absorption by transitions into the state 4 are expected in such a DQW, comparing the case of single NW.

Figure 3.9 shows the intersubband absorption spectra for three samples with the same $L_{WW}$ and different $L_{NW}$, samples A28, A26, and A24

Table 3.1: Calculated oscillator strengths for considered samples.

| No. | $L_{NW}$ (nm) | $L_{WW}$ (nm) | $f_{12}$ | $f_{13}$ | $f_{14}$ | $f_{23}$ | $f_{24}$ | $E_F - E_2$ (meV) |
|---|---|---|---|---|---|---|---|---|
| A28 | 2.8 | 3.2 | 0.43 | 0.19 | 0.21 | 0.75 | 0.14 | 135 |
| A26 | 2.6 | 3.2 | 0.39 | 0.35 | 0.16 | 0.66 | 0.27 | 117 |
| A24 | 2.4 | 3.2 | 0.34 | 0.48 | 0.08 | 0.56 | 0.29 | 84 |
| A22 | 2.2 | 3.2 | 0.31 | 0.57 | 0.04 | 0.48 | 0.26 | -44 |
| A24-6 | 2.4 | 2.6 | 0.51 | 0.04 | 0.21 | 0.66 | 0.04 | 285 |

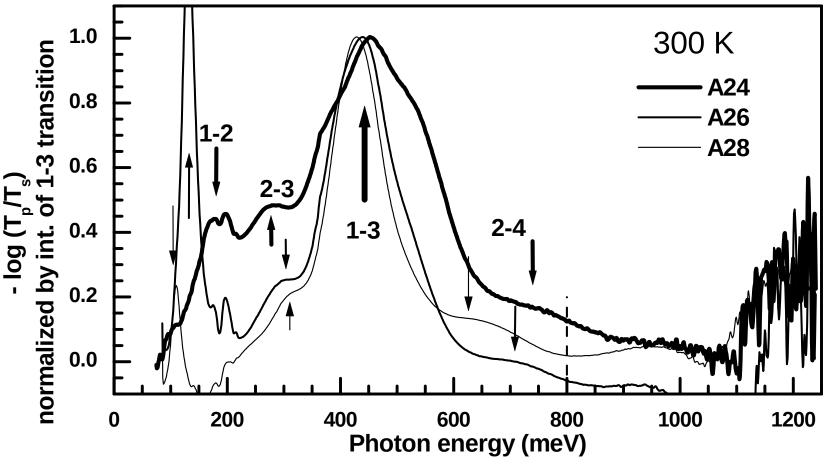

Figure 3.9: Room temperature intersubband absorption of samples A24, A26, and A28, scaled by the intensity of 1-3 line absorption amplitude. The same set of transitions is observed here for all the three samples: 1-2, 2-3, 1-3, and 2-4. Observed spectral shift is consistent with a width variation of a narrow well. In case of sample A28, however, 1-2 transition is at the very edge of the CaF beamsplitter transmission range, which might affect it's lineshape.

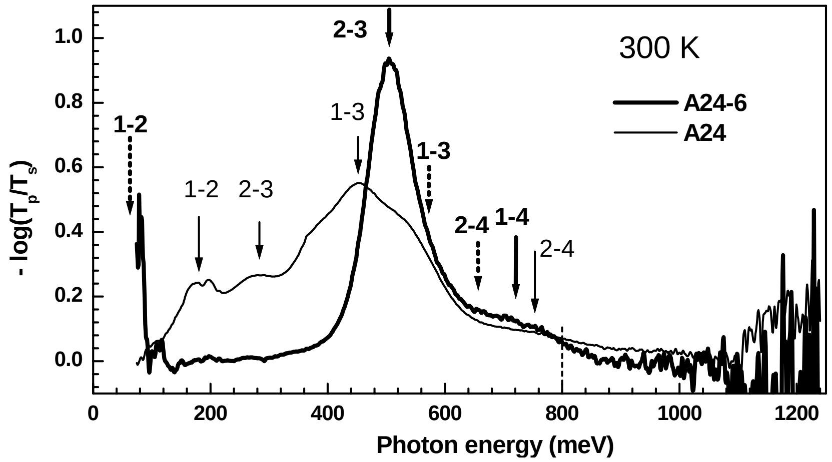

Figure 3.10: Room temperature intersubband absorption of sample A24 (thin line) and A24-6 (thick line). Spectral positions of individual intersubband transitions are indicated with the thick arrows for A24-6 and thin arrows for A24. Dotted arrows mean, that correspondent individual transitions are not clearly resolved. Transitions 1-3 and 2-4 in sample A24-6, for example, are not seen at all, which is consistent with a small calculated correspondent oscillator strengths (see table).

(see table 3.1). The spectral position of the strongest 1-3 transition (3.1 $\mu$m) is very similar in all three samples because the both states 1 and 3 are mostly localized in the 3.2-nm well. The varying of the narrower QW width affects primarily the energies of states 2 and 4 because these states are mostly localized in the narrower well. Consequently, reducing the width of the narrower well causes a red shift of the 2-3 and a blue-shift of 2-4 and 1-4 transitions. In the case of A24, the shoulder of the absorption band attributed to the 2-4 transition extends beyond 800 meV. The 1-4 transitions are hardly seen, most probably due to their very small oscillator strengths (see table 3.1). The relation between the transition energies and the well width is in all cases consistent with behavior described above.

Figure 3.10 shows the intersubband absorption spectra for two samples with the same $L_{NW}$ and different $L_{WW}$, samples A24 and A24-6 (see table 3.1). Narrowing the $L_{WW}$ from 3.2 nm to 2.6 nm increases the energy of 2-4 transition but drastically decreases it's oscillator strength (see table 3.1). At the same time oscillator strength of 1-4 transition increases, but it's transition energy increases (see table 3.1). Finally we obtain 1-4 transition in the sample A24-6 to be stronger, than 2-4 one. However, there is no improvement neither in transition energy, no in absolute absorption amplitude, when comparing the 2-4 transition in sample A24. Spectra on the Fig. 3 are not scaled, and it is clearly seen that short wavelength absorption in 700-800 meV range is of very similar amplitude.

Such a complex interplay of transition energy and oscillator strength makes it difficult to obtain shorter wavelength transitions with a decent absorption amplitude for a fixed material system. One of the key issues here seems to be a week localization of high energy states. And since that, further narrowing of 2,4 nm QW is a misleading strategy for device oriented designs. It will increase the transition energy, but it will decrease the transition oscillator strength at the same time. A possible improvement of present DQW design would be surrounding the narrow well with a $In_{0.70}Ga_{0.30}As$-AlAs superlattices, which form a minigap of states at the energy of a second confined level in the narrow well (or just above the conduction band edge of AlAs) (144; 168; 169). Such a design would increase localization of the upper electron state in narrow QW and, consequently, increase intersubband absorption amplitude.

Now we want to comment briefly the peaks, marked by "1-2" on Fig. 2 and 3. Spectral position and spectral shift of those features, when changing $L_{NW}$, convincing us, that they are transitions from state 1 to state 2 (as indicated on Fig. 3.8) at high values of wave-vector. However, we want to point out that the narrow width of this feature and quite high intensity in case of sample A26 is rather confusing. This is probably an artifact due to the operation close to the edge of used GaF beamsplitter spectral range. To clarify our interpretation of those peaks it would be more likely to obtain them in more convenient spectral range. To shift those transitions slightly towards the higher energies and make them more intensive, we have grown an additional DQWs with 2.2 nm thin NW and *nominally* 3.2 nm thick WW (sample A22, see table) with twice less doping density than in other samples. In this case due to increase of states 1 and 2 energy splitting and reduced doping the state 2 is not populated. This leads to a single 1-2 peak around 200 meV (see Fig. 3.11), and vanished 2-3 transitions. Transition 1-3 is shifted towards the higher energies, comparing the spectra of sample A24. It is most probably, because the WW was grown slightly thinner, than nominal 3.2 nm.

Thus, using a design based on double quantum wells in the strain-compensated AlAs-$In_{0.70}Ga_{0.30}As$ system, intersubband transitions within a broad wavelength range, including 1.55 $\mu$m, are achieved.

To summarize, a comprehensive study of intersubband transitions in $In_{0.70}Ga_{0.30}As$-AlAs DQWs is provided. Consistent interpretation of observed transitions is given. Drop of absorption coefficient from smaller to higher energy transitions is consistent with calculated oscillator strengths

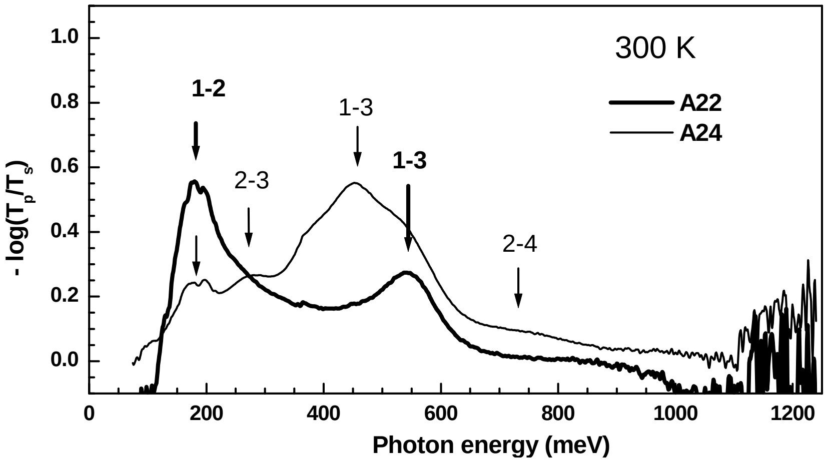

Figure 3.11: Room temperature intersubband absorption of sample A24 (thin line) and A22 (thick line). Spectral positions of individual intersubband transitions are indicated with the thick arrows for A22 and thin arrows for A24.

and the states population. It is mostly due to the weak spatial localization of high-energy state 4 (as marked on Fig. 3.8). 1.55 $\mu$m (800 meV) is covered within the absorption line-width of intersubband transition 2-4 within the 2.4-3.2 nm DQWs and transition 1-4 within the 2.4-2.6 nm DQWs. Stronger 2-4 transitions are expected to obtain, when using the AlAs-In$_{0.70}$Ga$_{0.30}$As superlattice barriers in combination with 2.4 nm well.

## 3.3 Growth and characterization of QCL test-structures

### Preface

Before to design a QCL on the new strain-compensated material combination we have grown, processed, and characterized two lattice-matched InGaAs-InAlAs/InP QCLs designed after Hofstetter *et al.* (131). One of them, hub1254, was grown with InAlAs cladding and laser ridges were defined by wet chemical etching. Another one, hub1304, was grown with InP cladding and laser ridges were defined by a combination of chemically assisted ion beam etching, CAIBE, and wet chemical etching. Detailed analysis of performance of this two structures is described elsewhere (185). In the following section we briefly analyze some design and fabrication issues, which will be afterwards transferred onto the new material combination.

### 3.3.1 Analysis of the active region design

In this subsection we analyze the QCL test-structures design.

Figure 3.12 depicts conduction band profile and moduli square of Wannier-Stark states wavefunctions of a 1.5 cascade of active region at 40 kV/cm electric field. Injection into higher lasing state 4 (see Fig. 3.12) is done from the miniband of Wannier-Stark states miniband of injector region (left side). Fast depopulation of lower lasing state occurs through the resonant LO phonon scattering of carriers from state 3 to state 2 and further to state 1 (so-called double-phonon resonance (131; 124)) with following escape into the next injector region (right side). ("State 4" is actually a combination of two coherently coupled states spaced by ≈4 meV at ≈40 kV/cm electric field). State 4 and 3 have a big overlap in real space, which leads to a high value of matrix element, up to $z_{43}$ ≈1.7 nm as calculated here (3nm in Ref. (129)), and thus, large oscillator strength

$$f_{43} = \frac{2m_e^*\omega_{43}}{\hbar}| < 4|z|3 > |^2 = 0.39, \tag{3.3}$$

and therefore a large gain (186)

$$g = \tau_4 \left(1 - \frac{\tau_3}{\tau_{43}}\right) \frac{4\pi\ e\ z_{43}^2}{\lambda_0\varepsilon_0\ n_{eff} L_p} \frac{1}{2\gamma_{43}}, \tag{3.4}$$

where $\gamma_{43}$ is the gain spectral width, usually estimated from electroluminescence, $L_p$ is the gain region size in real space (in QCLs it is usually taken to be the length of a single cascade of active region (186)), $n_{eff}$ is the effective refractive index of the mode, $\lambda_0$ is the transition wavelength, $\tau_3$ and $\tau_4$ are correspondingly the lifetimes on 3-rd and 4-th level, and $1/\tau_{43}$ is a state 4-to-state 3 scattering rate. Results on relevant scattering times and value of threshold current are given in Ref. (129).

From the analysis of current active region design we can summarize, that:

- The resonant coupling of one injector-region-state and upper-lasing-state is a necessary condition of the effective population of the upper-lasing-state.
- Such a resonant coupling leads to the "splitting" of the oscillator strength over two transitions (injector-region-state - to - lower-lasing-state and upper-lasing-state - to - lower-lasing-state). The resonant coupling is very sensitive to the external electrical field.

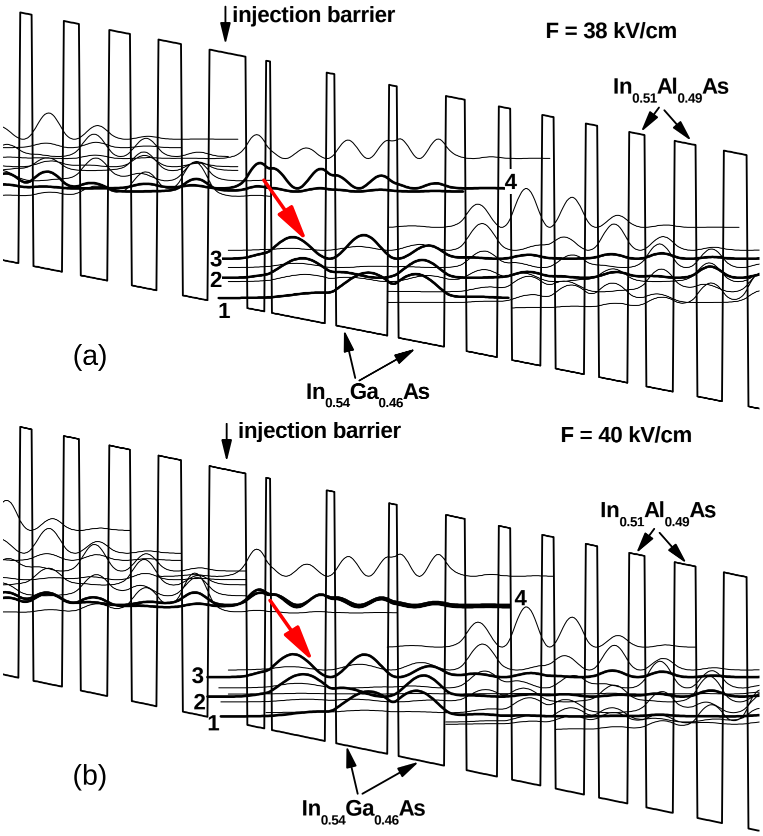

Figure 3.12: Calculated conduction band profile of a 1.5 cascade of QCL active region (same for sample hub1254 and hub 1304) at (a) 38 kV/cm and (b) 40 kV/cm electric field together with moduli square of Wannier-Stark state wavefunctions. Numerical calculations are done within the envelope function approximation using energy dependent electron effective mass after Ref. (84) to account for the band nonparabolicity. Parameters used are: effective mass in the $In_{0.54}Ga_{0.46}As$ well $m_e^w = 0.043 \cdot\ m_0$ and in $In_{0.51}Al_{0.49}As$ barrier $m_e^w = 0.073 \cdot\ m_0$; the nonparabolicity parameters are $\gamma_{well} = 9.6 \times 10^{-19}$m2 and $\gamma_{well} = 3.2 \times 10^{-19}$m2; CBO $\Delta\ E_c = 514 meV$. Appropriate software used for calculations is developed by Mathias Ziegler (185).

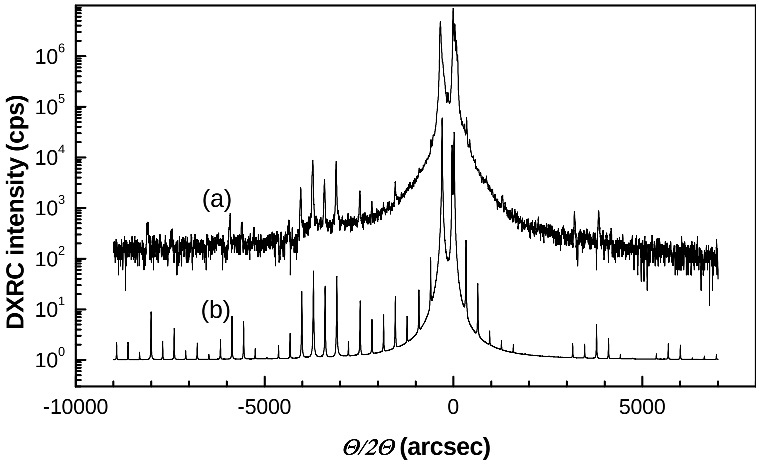

Figure 3.13: Double crystal rocking curves of Hofstetter's QCL structure, but with $In_{0.54}Ga_{0.46}As$ wells and $In_{0.51}Al_{0.49}As$ barriers. (a) measurement of the grown sample, hub1254, (b) dynamic scattering theory simulation.

- Depending on the broadening of the states, laser cavity length and on the thickness of the injection barrier lasing transitions from the two coherently coupled upper states might be spectrally resolved (for low broadening, thin injection barrier, and short laser cavity).

### 3.3.2 Basic characterization of QCL structure

In this subsection we characterize the optical and crystalline quality of the grown wafers.

Whole QCL structure was grown in the single run, exploiting a unique possibility of used GSMBE setup to deposit arsenides and phosphides at the same time. Active region was grown at 500 °C without interruptions on the heterointerfaces. Figure 3.13 shows DXRC of the whole QCL together with simulation of the nominal layer sequence (but with $In_{0.54}Ga_{0.46}As$ wells and $In_{0.51}Al_{0.49}As$ barriers instead of lattice matched compositions in original design (131)). Excellent matching of measured DXRC and simulation confirms precise control of layers composition and thicknesses over the whole $\approx 10\mu$m thick structure. Sharp DXRC features reflects the flat heterointerface morphology over 35 cascades of QCL active region.

Figure 3.14 depicts low temperature PL spectrum of QCL sample. Narrow PL linewidths of InGaAs waveguide, 19 meV, and InGaAs-InAlAs

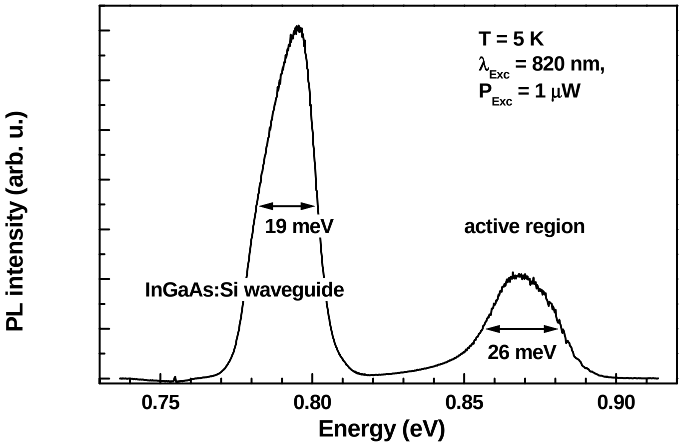

Figure 3.14: Low temperature photoluminescence spectrum of complete QCL structure grown after (131) with InP cladding.

active region, 26 meV, confirm high optical quality of grown material. Both DXRC and PL measurements confirm an excellent material performance.

### 3.3.3 Laser cavity

In this subsection we describe and analyze the issues connected with laser cladding and laser ridge fabrication.

Sample, hub1254, was grown on n-type (n$\approx 5 \cdot 10^{18}$ cm$^3$) InP:S substrate. 2 $\mu$m low doped InP:Si (n=$2 \cdot 10^{17}$ cm$^3$) layer was grown on the top of it to reduce the free carrier absorption in the substrate. The substrate together with InP:Si buffer served as a lower cladding layer of QCL. 3 $\mu$m thick lattice matched InAlAs:Si (n=$1 \cdot 10^{17}$ cm$^3$) was used as a top cladding layer. Sample hub1304 was grown following the same recipe, except the InP:Si top cladding instead of InAlAs. Figure 3.15 depicts scanning electron microscope, SEM, images of the cleaved facet of fully processed laser ridges of hub1304 (Figure 3.15 left panel) and hub1254 (Figure 3.15 right panel) wafers. Detailed processing description is given elsewhere (188). SEM facet imaging of laser from wafer hub1254 is made in backscattering electron mode, which is sensitive to chemical composition. Resolved are cladding layers, InGaAs:Si spacer layers, and active region (as indicated on Fig. 3.15). InGaAs spacing layers are used to enhance the refractive index step on the core-cladding interface.

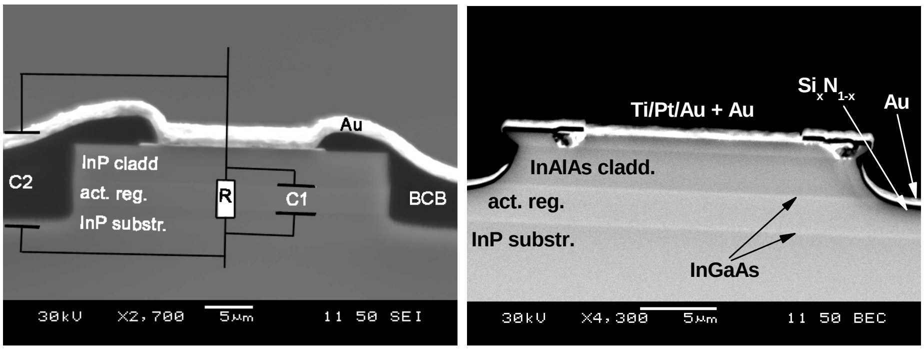

Figure 3.15: SEM images of the cleaved edges of two laser stripes. Smooth vertical sidewalls is a result of combined dry and wet chemical processes (left-side panel). Excellent sidewalls result in very low optical cavity losses. Thick electrical insulation layer of BCB deduces the bypass capacitance, C2, between the top metallization and substrate, and thus, reduces the bypass current in pulsed operation. Prism-like ridge profile (right-side panel) is a result of single-step wet chemical etching. Such a shape of the laser ridge increase slightly the effective area of the active region, thus increasing the necessary drive currents. However, prism-like ridge shape offers at the same time a better heat-sinking out the active region. For this laser ridge shape we have obtained slightly higher $T_0$ parameter that in vertical side-walls ridge. SEM images were acquired by Sebastian Dreßler. For details of QCL processing see Refs. (187; 188).

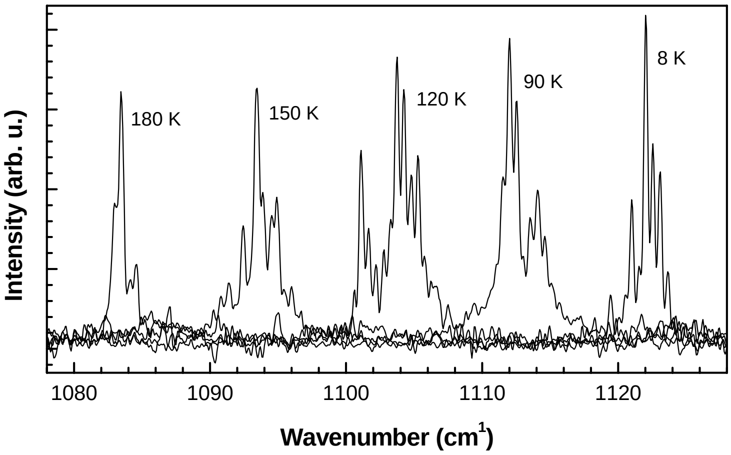

Figure 3.16: Lasing spectra acquired in 8-180 K temperature range from 34 $\mu$m wide and 2 mm long laser stripes, hub1254, driven with 100ns current pulses at 5 kHz repetition rate.

### 3.3.4 Laser performance

In this subsection we analyze the lasing spectra in respect to the active region design and compare performance of QCLs processed into the different shape ridges.

For emission measurements 20 $\mu$m wide 1-2 mm long cleaved laser stripes were mounted substrate down on a copper heat sink and placed in He continuous flow cryostat. Laser stripes were usually driven with 100-200 ns current pulses with 5 kHz repetition rate. We have obtained stimulated emission from many different stripes in 8-300 K temperature. Laser performance was found extremely sensitive to all the packaging steps. This, naturally, is not surprising, because QCLs usually operate in 0.5-10 kAcm$^{-2}$ current density range (at low temperature) (135; 135), which in turn requires very robust contacts and effective heat sinking.

Figure 3.16 shows an example of high resolution FTIR spectra from 2 mm long stripe in 8-180 K temperature range. Narrow mode structure confirms a high development of all, growth, processing, and packaging steps. Emission wavelength can be tuned with heat sink temperature over 8.9-9.3 $\mu$m spectral range, or within 133-139 meV energy range. Doping density (averaged per 60 nm thick single cascade) in present structure is only $0.4{\cdot}10^{17}$ cm$^{-3}$. Therefore, many body effects (in particular, depolarization shift, see section 2.2) are not expected to influence the generation wavelength.

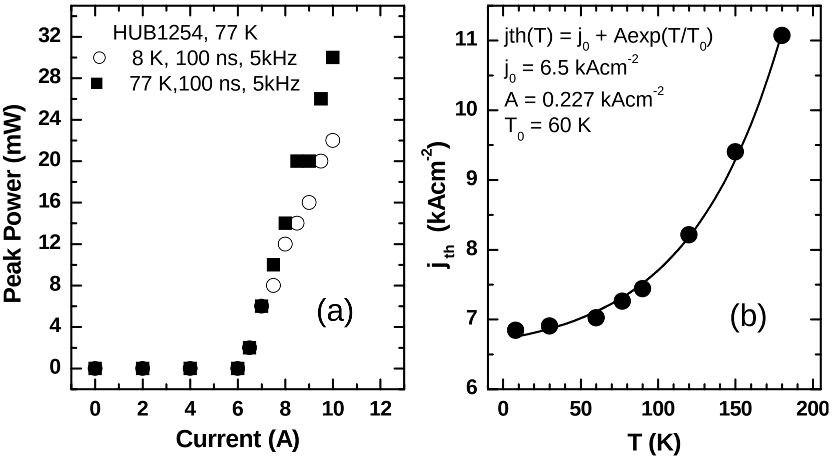

Figure 3.17: (a) Peak power, collected from the single laser facet at 8 K and 77 K heat sink temperatures. Laser strips where 20 $\mu$m wide and ≈2mm long, facets where left uncoated. Collecting efficiency estimated to be approximately 30%. (b) Threshold current density vs heat sink temperature.

On another hand, band gap difference between lattice matched (to InP) InGaAs and InAlAs varies with a temperature over a narrow 2.5 meV range (as calculated after Ref. (181) including recommended bowing parameters). Therefore, assuming that ratio of CBO to fundamental energy gap difference is constant, CBO does not vary with temperature more than 2 meV per 300 K.

Although intraband scattering lead into narrow distribution of higher lasing state electrons in $k$-space, this distribution is temperature dependent. Therefore, difference in subbands dispersion (due to the band non-parabolicity effect) broadens and shift to the longer wavelength a gain spectrum and thus the lasing wavelength shifts. Strong spectral shift of the gain spectrum maximum is reported in a number of theoretical studies (189; 190). Upper and lower states themselves are broadened with temperature due to increase of electron-phonon scattering rate by approximately factor 2 (186).

Figure 3.17 (a) depicts dependence of laser power collected from the single facet vs current at 8 K and 77 K. Collection efficiency was estimated to be approximately 30% After a certain threshold laser power increases linearly with injected current with a slope ≈7.5mW/A. Figure 3.17 (b) depicts the threshold current density obtained in 8-180 K temperature range. From the fit of the temperature dependence of threshold current with phenomenological formula (186),

$$J_{th} = J_0 \cdot e^{T/T_0} + J_1, \tag{3.5}$$

we have deduced $T_0 = 80°\mathrm{C}$. In original Hofstetter's report of present QCL design slope efficiency of 0.4 W/A and $T_0 = 204$ K were reported, which is a way better performance, comparing to our results.

InAlAs cladding was observed to lead into higher waveguide losses (191). Together with 20 times lower thermal conductivity of InAlAs comparing the InP it was reported (191) to lead into 10 times lower peak power at 300 K comparing the case of InP cladding. Therefore, we relate the difference in performance of our structure comparing that in original Hofstetter's paper (131) mostly due to the InAlAs cladding, but also due to free carrier absorption in highly doped InP:S substrate.

## 3.4 Short-wavelength InGaAs-AlAs QCL

### 3.4.1 Outlook of short wavelength QCLs

Since their first realization, quantum-cascade lasers (QCLs) (2) have been demonstrated with emission wavelengths between 3.5 $\mu$m (5) and 100 $\mu$m (192). The range of demonstrated room-temperature operation is somewhat smaller, being 4.5–16 $\mu$m (193; 194). Operation within the atmospheric window in the band between 2.9 and 5.3 $\mu$m is interesting for gas detection because a large number of molecules (e.g., NO, CO, $CO_2$, $CH_2O$, $SO_2$) have characteristic absorption in this band. QCL operation in this band and, especially, near room temperature, remains challenging: Short wavelength emission requires a large conduction band discontinuity and narrow wells. Furthermore, the ability to operate the laser at higher temperatures requires that the conduction band edge in the barrier material lies much higher in energy than the upper lasing level to inhibit the thermally-activated escape of carriers into the quasi-continuum. Novel QCL materials with very high conduction band discontinuities (4; 4) have already shown laser action at long wavelength, but demonstrations at short wavelengths and at higher temperatures are not yet reported. To date the shortest wavelength QCLs have been based on the strain-compensated InP-based InGaAs/InAlAs system (5).

Within this system, the largest Γ-valley conduction band discontinuity can be reached using AlAs as the barrier. Already the introduction of thin AlAs blocking layers into a lattice-matched $In_{0.53}Ga_{0.47}As$-$In_{0.52}Al_{0.48}As$ design improves the temperature performance of a 5-$\mu$m QCL (195). The use of pure AlAs barriers throughout the active region is more difficult due to its large lattice mismatch to InP. In section 3.2 we have successfully demonstrated the growth of and short-wavelength intersubband transitions in short-period $In_xGa_{1-x}As$-AlAs strain-compensated superlattices. The current section describes the design and performance of a $In_{0.73}Ga_{0.27}As$-AlAs QCL with both short laser

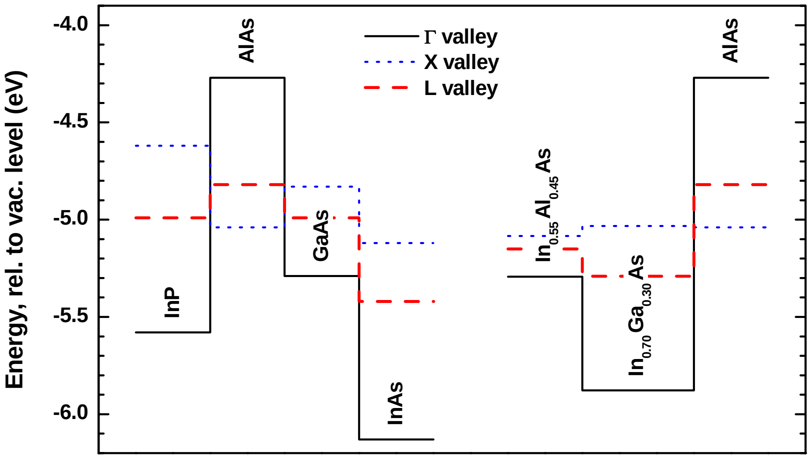

Figure 3.18: Γ-, X-, and L-valley positions for binary materials involved in QCL design (left hand side), and particular ternary compounds which build the active region (right hand side). Note, that the lowest indirect band in active region is L-valley in $In_{0.73}Ga_{0.27}As$ well material.

emission wavelength and high operation temperature.

### 3.4.2 Design of short-wavelength InGaAs-AlAs QCL

#### L-valley in InGaAs

An important issue which we need to consider now (before the attempt to design $In_{0.73}Ga_{0.27}As$-AlAs QCL) is indirect valleys in all the three materials: $In_{0.73}Ga_{0.27}As$, AlAs, and $In_{0.55}Al_{0.45}As$. ISB absorption in Γ-valley can be observed even if excited state is above an indirect valley minima. But laser active region design has necessary to be done so, that upper lasing state is below indirect valley minima (196). Otherwise inter-valley scattering will reduce population inversion between the lasing states, and thus brake the lasing conditions.

Figure 3.18 (left hand side) depicts Γ-, X-, and L-valley minima positions for some binary materials relatively vacuum level, calculated after Refs. (181; 25) without accounting for strain. Figure 3.18 (right hand side) depicts those valleys minima positions for our ternary alloys, obtained as linear interpolation between correspondent binary compounds. As one can see from the figure, the lowest indirect valley in $In_{0.73}Ga_{0.27}As$-AlAs-$In_{0.55}Al_{0.45}As$ material combination is L-valley in $In_{0.73}Ga_{0.27}As$, which is almost at the position of $In_{0.55}Al_{0.45}As$ Γ-valley minimum. Compressive strain and quantum confinement will shift the lowest L-valley state in $In_{0.73}Ga_{0.27}As$ somewhat higher. But we can already roughly estimate the shortest target wavelength in $In_{0.73}Ga_{0.27}As$-AlAs active region assuming that the upper lasing state can be put as high as $In_{0.55}Al_{0.45}As$ Γ-valley minimum, i.e. 540 meV above the bottom of $In_{0.73}Ga_{0.27}As$ QW (see Fig. 3.4). This gives us $n = 2$-to-$n = 1$ transition energy (3/4)·540 meV = 405 meV (in approximation of infinite barriers QW). In another words, because of the low L-valley minimum in $In_{0.73}Ga_{0.27}As$ the shortest expected lasing wavelength is in the best case 3 $\mu$m (although in absorption we have obtained transitions as short as 1.7 $\mu$m).

Regarding the low L-valley position in InAs (see Fig. 3.18 left hand side) it becomes clear, that further increase of In content in the well (say, even up to pure InAs) would give a minor advantage for shortening the possible lasing wavelength. In this contest, 3.5 $\mu$m strain-compensated QCL reported by J. Faist *et al.* (5) was already at the edge of possibilities of InGaAs-InAlAs/InP material system at all.

### Chirped superlattice active region design

QCL active region design is a result of quite sophisticated engineering of Wannier-Stark states. Precise eigne states calculations are needed for designs with resonant LO-phonon depopulation of lower lasing state (see section 2.4 for brief review). On the other side, in superlattice active region designs fast depopulation of the lower lasing state is achieved "automatically" through the intra-miniband scattering. To be less dependent on precision of our calculation we decided to try few own $In_{0.73}Ga_{0.27}As$-AlAs SL active region designs.

Figure 3.19 depicts the Γ-valley conduction band edge profile within a single period of the active region under an electric field of 76 kV/cm along with the calculated probability functions for confined electronic states. The confined state wavefunctions are obtained within an effective mass approximation; to account for band nonparabolicity, we used an energy-dependent effective mass after Nelson *et al.* (84). Used parameters: the Γ-valley conduction-band discontinuity for $In_{0.73}Ga_{0.27}As/AlAs$ and $In_{0.73}Ga_{0.27}As/In_{0.55}Al_{0.45}As$ are 1.38 eV and 0.55 eV; the effective mass at the bottom of Γ-valley and the nonparabolicity parameters for $In_{0.73}Ga_{0.27}As$, $In_{0.55}Al_{0.45}As$, and AlAs are: (0.035, 0.070, and 0.150)$\times m_0$ and (12.8, 3.5, and 0.9)$\times 10^{-19}$ m$^2$.

The lowest indirect valley in the described system of materials is the $L$ valley in $In_{0.73}Ga_{0.27}As$. Its energy (indicated with a dashed line on Fig. 3.19) approximately coincides with the Γ-valley minimum in $In_{0.55}Al_{0.45}As$ (25; 181), which is ≈90 meV above the upper lasing state, *2*. This energetic separation, corresponding to almost 3 LO phonon energies, is sufficient to effectively suppress thermally-activated $\Gamma - L$ inter-valley carrier leakage near room temperature.

The design of the active region is similar to the bound-to-continuum

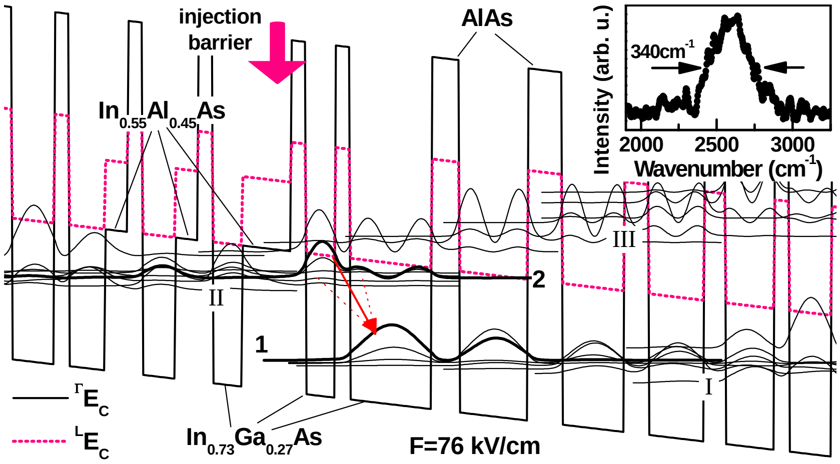

Figure 3.19: Conduction band profile and Wannier-Stark states of one and half cascade period in InGaAs-AlAs QCL structure, hub1507 at applied electric field of 76 kV/cm. Red dotted line indicates the level of L-valley $In_{0.73}Ga_{0.27}As$. Strain in L-valley included using elastic constants as in Ref. (197). Other parameters taken from Refs. (25; 181). Upper lasing state is calculated (185) to be 90 meV below the $In_{0.73}Ga_{0.27}As$ L-valley minima. The layer thickness in nm from left to right starting from the injection barrier (indicated by arrow) are: *3.0*/**0.9**/1.8/**0.9**/5.0/**1.7**/4.2/**2.1**/3.8/**1.5** /3.4/**1.3**/3.0/**0.9**/2.6/**0.9**/2.2/ *1.4*/**0.9**/2.0/*1.4*/**0.9**/1.8. AlAs layers are in bold, $In_{0.73}Ga_{0.27}As$ layers are in roman, and $In_{0.55}Al_{0.45}As$) layers are in italic. Underlined layers are doped to $5{\cdot}10^{17}$ cm$^{-3}$. The moduli square of the wavefunctions (1 and 2) responsible for the laser action are drawn with the thick lines. We have calculated 0.47 nm dipole matrix element for 2-to-1 transition at 76 kV/cm. The inset shows a below-threshold electroluminescence spectrum of a 39$\mu$m×2mm laser bar at 8 K. (Originally active region was designed by the author of the thesis using the "Poisson-1D" solver, as in subsection 3.2.2. However, the software developed by Mathias Ziegler (185) does properly accounts for the band non-parabolicity and gives better agreement with experimental results.)

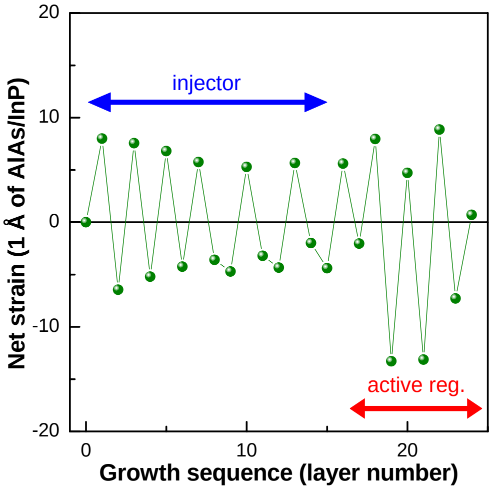

Figure 3.20: Strain profile through the single cascade period in InGaAs-AlAs QC structure, hub1507.

approach pioneered by Faist *et al.* (133), but the injection barrier is thinner (3.9 nm) than in a typical bound-to-continuum design. The consequence is that some states of the injector miniband *II* (separated by 1–10 meV from the upper lasing state ***2***) also spatially overlap with the lower lasing state ***1***. At 76 kV/cm, the dipole matrix elements of the resulting “parasitic” transitions (dashed arrows on Fig. 3.19) are as high as 0.29 nm, comparable to the 0.47 nm matrix element of the principal ***2***-to-***1*** transition (solid arrow on Fig. 3.19)). These multiple transitions result in a broad gain spectra, as reflected in the broad electroluminescence (inset on Fig. 3.19). Despite the broad gain, the design allows population inversion for multiple transitions due to the high injection efficiency into the upper lasing states, the low carrier leakage into the miniband ***III*** and into the indirect valleys, and the diagonal character of the lasing transitions.

**Strain compensation**

Using three different materials in injector and active region design let us independently manipulate the average conduction band profile (namely, engineer miniband in injector region) and strain profile over a single cascade. Figure 3.20 depicts perturbation of the total strain over a single cascade of active region. Strain is normalized to that of 0.1 nm of AlAs on InP for convenience. We know from the growth of previous structures, that at used growth conditions (for details we refer to previous section) we can surely grow 2.0 nm of AlAs on InP pseudomorphically. Therefore, keeping the local strain below that of 2.0 nm AlAs and net strain of a single cascade at zero we succeed to repeat single cascade as many times as necessary for particular design, still maintaining coherent 2D growth mode (as monitored *in-situ* by RHEED and *ex-situ* by Nomarski phase-contrast microscopy and X-ray).

### 3.4.3 Growth and characterization of InGaAs-AlAs QCL-structure

**Laser cavity design and growth**

The laser structure (HUB1507) was grown on a low doped ($n = 2{\cdot}10^{17}$ cm$^{-3}$) InP:Sn substrate, which serves as a lower cladding layer. It consist of: 220 nm $In_{0.52}Ga_{0.48}As$:Si ($n = 5 \cdot 10^{16}$ cm$^{-3}$) lower waveguide; 1.4 $\mu$m thick 30 periods active region; 220 nm $In_{0.52}Ga_{0.48}As$:Si ($n = 5 \cdot 10^{16}$ cm$^{-3}$) top waveguide; 18 nm thick $In_{0.52}Ga_{0.48}As$:Si-$In_{0.52}Al_{0.48}As$:Si four period graded superlattice; 2.5 $\mu$m ($n = 1 \cdot 10^{17}$ cm$^{-3}$) InP:Si plus 0.8 $\mu$m ($n = 4{\cdot}10^{18}$ cm$^{-3}$) InP:Si top cladding layer; and 130 nm $In_{0.52}Ga_{0.48}As$:Si ($n = 1 \cdot 10^{19}$ cm$^{-3}$) top contact layer. Whole laser structure was grown in a single run by gas-source MBE.

Two component ($In_{0.55}Al_{0.45}As$ plus AlAs) barriers, used in some places of active cell, allowed us to tune the barrier thicknesses and the net strain almost independently. *This solution, makes the band engineering in present, $In_{0.73}Ga_{0.27}As$-AlAs, material system as easy as in case of lattice matched $In_{0.53}Ga_{0.47}As$-$In_{0.52}Al_{0.48}As$ combination.*

**X-ray rocking curve and simulation**

Figure 3.21 presents experimental X-ray rocking curve and simulation of a full $In_{0.73}Ga_{0.27}As$-AlAs$In_{0.55}Al_{0.45}As$ QCL-like structure with 26 cascades of active region and 3 $\mu$m InP cladding, hub 1507, grown in a single growth run. Fit of simulated curve to experimental data is done by tuning nominal thicknesses of individual layers in active region by less than 0.1 nm. In composition of used alloys was tuned to $In_{0.73}Ga_{0.27}As$-AlAs$In_{0.55}Al_{0.45}As$. Note, that we succeeded almost perfect matching of satellite intensity distribution in experiment and fit. Sharp satellites confirm high crystalline quality of the structure.

It is necessary to note, that rocking curves on Figs. 3.13, 3.5, and 3.21 were done on different instruments with different resolution and signal/noise ratio, therefore a straightforward comparison of those rocking curves is difficult.

**Photoluminescence**

Figure 3.22 depicts room temperature PL spectrum from QCL wafer hub 1519 in 0.7-to1.25 meV spectral region. Narrow PL linewidth of InGaAs waveguide, 60 meV, and intensive, but broad, line from InGaAs-InAlAs active region confirm high optical quality of grown material. Both DXRC and PL measurements confirm good material performance.

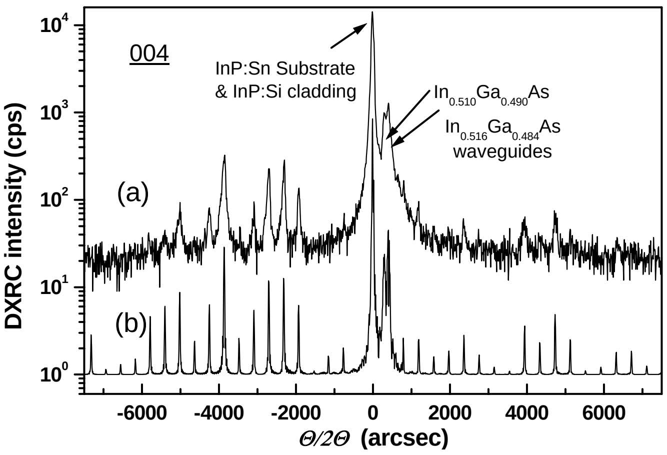

Figure 3.21: 004 reflection DXRC of a full QCL-like structure, hub 1507, with InP cladding (black solid curve). Dynamic scattering theory simulation of experimental data (red dotted curve).

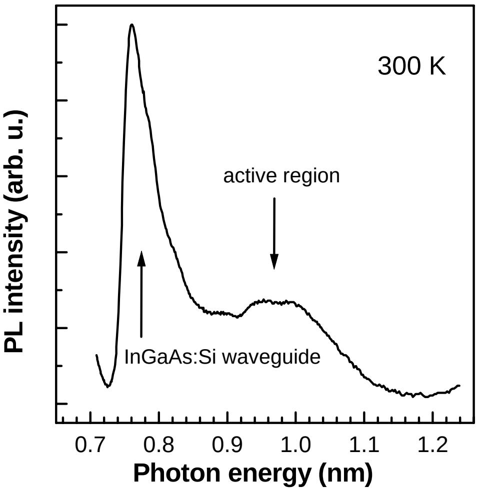

Figure 3.22: Photoluminescence spectrum from $In_{0.73}Ga_{0.27}As$-AlAs cascade structure, hub1507.

The grown structure was processed into a series of 28–44-$\mu$m wide ridges using a combination of chemically-assisted ion beam etching (CAIBE) and wet-chemical etching techniques. The substrate was thinned to 100 $\mu$m. Ti/Pt/Au contacts were then deposited on the top of the ridge and the bottom of the substrate and alloyed for 2 min at 430°C. The laser bars were then electrically insulated with bisbenzocyclobutene (BCB). Approximately 16-$\mu$m wide windows were opened on the top of the ridges and 1–2 $\mu$m of gold was deposited on the insulated laser bars for electrical contact between the ridge and contact pad. Laser bars with length 1.5 and 2 mm were cleaved and mounted, substrate down, on Au-plated copper sub-mountings. The cleaved facets were left uncoated.

### 3.4.4 Performance of InGaAs-AlAs QCL

**Short-wavelength operation**

Processed laser bars were characterized using 100-ns current pulses at a repetition rate of 5 kHz. Depending on temperature and driving current, the lasers emit at either a single or at multiple wavelengths in the 3.7–4.2 $\mu$m spectral range; the shortest laser emission observed is 3.74 $\mu$m at 8 K for the 39$\mu$m$\times$2.0mm laser bar. For the 28$\mu$m$\times$2.0mm laser bar and at 8 K, the threshold current was 0.48 A (857 A/cm$^2$) with maximum peak power of 6 W per facet; at room temperature the threshold current density was 4.8 kA/cm$^2$ and the maximum peak power 240 mW per facet. Laser operation was achieved up to 330 K.

Figure 3.23 shows high-resolution Fourier-transform spectra acquired in the step-scan mode from three different laser bars measured at a variety of temperatures and currents. The resulting laser mode structure (single mode, multi-mode (Fig. 3.23a), or multi-wavelength (Fig. 3.23b and c) depends on the drive current and temperature. Both single-color and multi-color operation modes were observed in all tested laser bars. The total spectral range covered with multi-color laser action at T=8 K and different driving currents extends from 3.7 $\mu$m to 4.1 $\mu$m; at T=296 K this range extends from 3.8 $\mu$m to 4.2 $\mu$m. A broad spectral range of observed laser emission for each tested device supported by the electroluminescence is indicative of a broad gain spectrum, which, in turn, can be utilized in advanced tunable laser configurations (198; 199; 200).

**Discussion of multi-color operation**

Now we discuss in some more details the nature of the multi-color operation of the current structure HUB1507. General behavior observed for all tested devices is that just above the threshold we obtain a single-color single-mode operation. At slightly increased drive current a number of longitudinal modes appear. And at higher values of drive current the additional transitions (colors) appear. They spectral position does

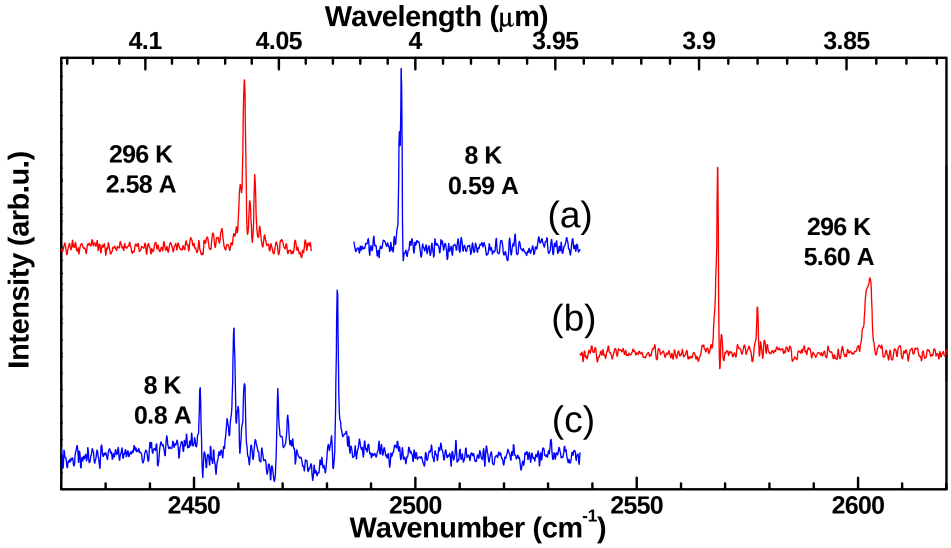

Figure 3.23: High-resolution Fourier-transform emission spectra from (a) 34$\mu$m$\times$1.5mm, (b) 39$\mu$m$\times$2.0mm, and (c) 28$\mu$m$\times$2.0mm lasers at different heat-sink temperatures and currents, as indicated. Used current pulses were 100 ns long with 5 kHz repetition rate. Lasers were cleaved at different locations of 2-inch wafer and operate at slightly different wavelengths due to the usual layer thickness gradient over the wafer.

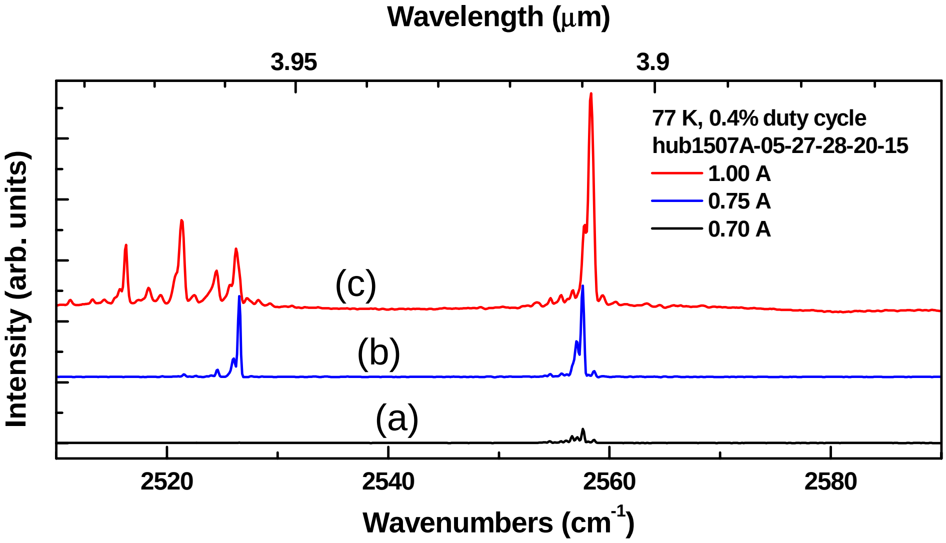

Figure 3.24: High-resolution Fourier-transform emission spectra from a 28$\mu$m×1.5mm laser acquired at liquid nitrogen temperature and different drive currents: (a) 0.7 A, (b) 0.75 A, and (c) 1.0 A. Used current pulses were 100 ns long with 40 kHz repetition rate. Note that at 0.75 A drive current the intensities of laser transitions at 3.96 $\mu$m and at 3.91 $\mu$m are almost the same. While at other currents (either higher or lower) the 3.91 $\mu$m transition dominates. Here transition at 3.96 $\mu$m is related to transition between the "leaking" state of injector miniband ***II*** and the lower lasing state ***1*** (see Fig. 3.19). Transition at 3.91 $\mu$m is related to transition between the upper lasing state ***2*** and the lower lasing state ***1*** (see Fig. 3.19). The 4 meV spacing of this two different transitions agrees well with one calculated at 76 kV/cm electric field.

not match to the mode spectrum of the principal transition (one, which appears at first and is always the most intensive).

There are at least two ways to explain the appearance of different colors in the spectrum of individual laser device. First explanation is that they are transitions from different states of the miniband ***II*** and state ***2*** to the lower lasing state ***1*** (see Fig. 3.19). If so, then (i) the energy spacing between different colors according to our calculations must be more than 4 meV; (ii) because the dipole matrix elements of corresponding transitions depend strongly on applied electrical field the intensity distribution over different colors must also depend strongly on applied electrical field.

Second explanation is that different colors are principal ***2***-to-***1*** lasing transitions in different active region cascades, which are hypothetically not equivalent. For example, a submonolayer change of the layer thicknesses in different cascades can shift the lasing transition to different wavelengths (accounting for the huge CBO). If so, then (i) there is no restrictions on the spectral spacing of different colors; (ii) the intensity distribution over different colors at fixed temperature should be almost constant, as it is mostly defined by the number of periods, which contribute to the gain of each color.

Different threshold conditions are easy to understand in both cased, as threshold depends on the dipole matrix element of different transitions as well as on the number of contributing cascades (186).

The spectrum (c) on Fig. 3.23 shows four different transitions spaced by ≈1–2 meV. Because of such a very small spacing these are, probably, different transitions which appear due to the presence of the regions with non-identical cascades in the laser core.

Figure 3.24 depicts the evolution of the lasing spectrum from a $28\mu\text{m}\times1.5\text{mm}$ laser at increasing drive currents. Intensity of the laser transition at ≈3.97 $\mu$m depends strongly on the drive current. Different drive currents, in turn, correspond to different biases, which changes the dipole matrix elements for the ***II***-to-***1*** and ***2***-to-***1*** transitions (see Fig. 3.19). Calculations of correspondent dipole matrix elements reveal the oscillation-like behavior with electric field. And at 82 kV/cm electric field the matrix element for the main 2-to-1 transition is equal to the one for the strongest transition from the miniband *II* to the lower lasing state ***1***. Experimental observation of such an oscillation-like behavior of the intensity distribution over the two laser transitions (Fig. 3.24) is an evidence that multi-color lasing occurs due to the multiple transitions within the one active region.

To summarize, there are at least two ways to explain the appearance of different colors in the spectrum of individual laser device. First explanation is that they are transitions from different states of the miniband

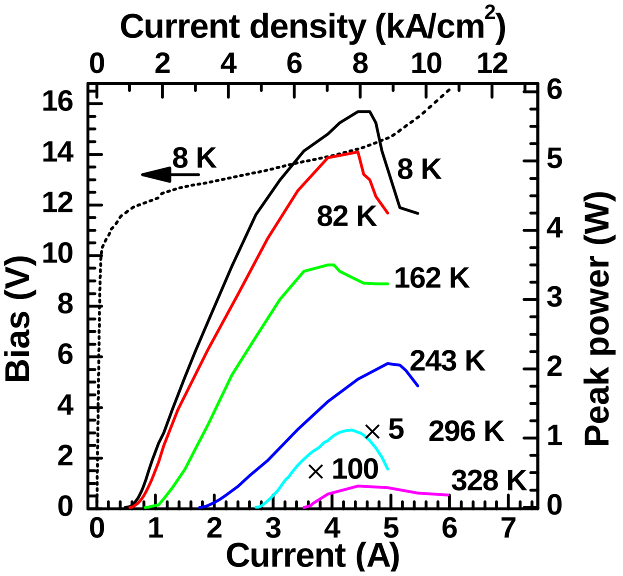

Figure 3.25: Pulsed optical power collected from a single facet of a 28$\mu$m×2mm laser bar *vs* current/(and current density) at a number of heat sink temperatures (as indicated on figure). The collection efficiency of optical setup is estimated to be $\eta \approx 40\%$ Plotted data are already multiplied by factor 2.5 to account for collection efficiency. Maximum peak power at $T$=8 K is approximately 6 W, ant those measured at $T$=296 K is 240 mW. The dotted curve is a current-voltage characteristics at $T$=8 K heat sink temperature. Device turn-on bias ranges between 10.6 V and 11.9 V for different temperatures.

***II*** and state ***2*** to the lower lasing state ***1*** (see Fig. 3.19). Second explanation is that different colors are ***2***-to-***1*** lasing transitions in different active region cascades, which are hypothetically not equivalent. Analysis of different experimental data along with the conduction band states calculation shows, that in the current structure we probably meat either one or another scenario depending on particular drive conditions.

**Output power**

Figure 3.25 shows the optical output power performance of a 28$\mu$m×2mm laser bar (see Fig. 3.23c) together with the low-temperature current-voltage (I-V) characteristics. At about 14 V bias (100 kV/cm electrical field) the I-V curve has a kink toward higher differential resistance which is accompanied by a drop in the optical output power. Our calculations show that even at 100 kV/cm the upper level remains well coupled to miniband *II* because the injection barrier is so thin. Rather, the laser efficiency decreases due to decoupling of the lower laser level ***1*** from the miniband *I* above 100 kV/cm and thereby reducing the extrac-

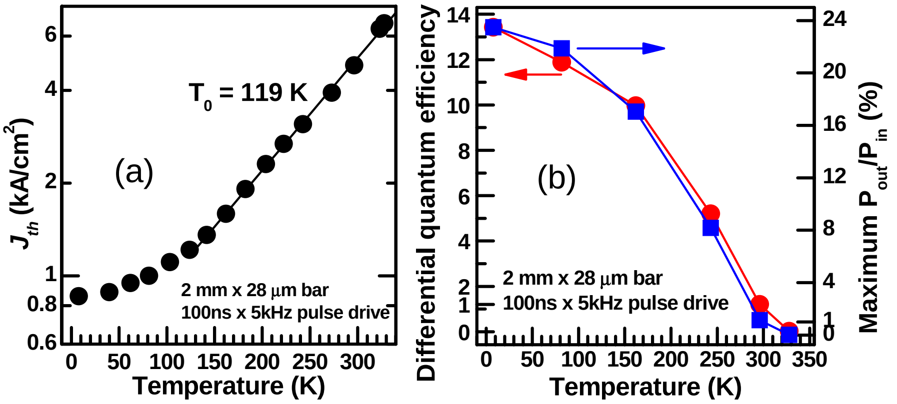

Figure 3.26: (a) Threshold current density, $J_{th}$, *vs.* heat-sink temperature for a $28\mu$m$\times$2mm laser ($\lambda \simeq 4.0\mu$m) in pulsed operation. The solid line is an exponential fit in the 140–328 K temperature range used to determine $T_0$. At a heat-sink temperature of 8 K, $J_{th} = 0.857$kA/cm$^2$. (b) Overall (all 30 periods) differential quantum efficiency and wall-plug efficiency as a functions of heat-sink temperature.

tion efficiency out of level ***1***.

Maximum peak power (Fig. 3.25b) at T=296 K is 240 mW per facet, which is already sufficient for gas-sensing applications. This performance at room temperature is achieved through the incorporation of the AlAs barriers even without advanced heat-sinking technology (e.g., buried heterostructure, epilayer-down mounting (201), etc.). At temperatures above 300 K, the power decreases rapidly (Fig. 3.25b) due to the thermally-activated carrier losses from the upper lasing state via scattering into the miniband *III* and into the *L*-valleys of the $In_{0.73}Ga_{0.27}As$, and the thermal backfilling of the lower lasing state ***1***.

**Characteristic temperature and laser efficiency**

The characteristic temperature was measured to be $T_0 = 119$ K from the dependence of threshold current density as a function of heat-sink temperature as depicted in Fig. 3.26(a). The threshold current densities ($J_{th} = 857$ A/cm$^2$ at 8 K, Fig. 3.26(a)) are the lowest values reported to date for QCLs emitting in the 3.5–5.0 $\mu$m spectral range and comparable to the best results at somewhat longer wavelengths (201).

Figure 3.26(b) depicts the wall-plug efficiency and overall (all 30 cascades) maximum differential quantum efficiency as a functions of heat-sink temperature. Wall-plug efficiency drops from 23% at 8 K down to 1% at 296 K. Differential quantum efficiency drops from 13 at 8 K down to 1.2 mW/A at 296 K.

**Summary of the laser performance**

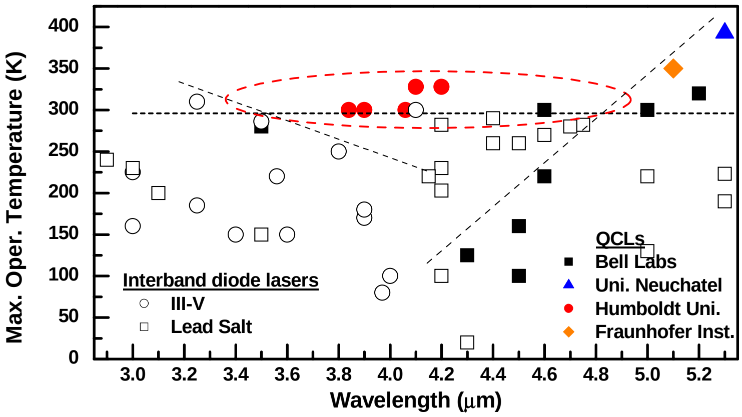

Figure 3.27: Summary of the maximum operation heat-sink temperatures *vs.* operation wavelength for published QCLs (solid symbols) within the first atmospheric window spectral range (5; 2; 148; 125; 126; 127; 128; 86; 124; 195). Open symbols indicate some of the very best recent achievements of interband lasers in current spectral region (for brief review see for example Refs. (202)).

To summarize, we have demonstrated the design and implementation of a quantum-cascade laser emitting between 3.7 and 4.2 $\mu$m. The design is based on strain-compensated $In_{0.73}Ga_{0.27}As$-AlAs on InP. At 8 K threshold currents as low as $J_{th} = 857$ A/cm$^2$ are obtained. Laser operation in pulsed mode is achieved up to a temperature of 330 K with maximum single-facet output peak powers of 6 W at 8 K and of 240 mW at 296 K. Due to the narrow (3.9 nm) injection barrier, our design allows multi-wavelength operation, similar to the superlattice active-region design (186). Thus, our particular design combines the high temperature operation advantage of the bound-to-continuum active-region design with multi-wavelength operation of a superlattice active-region design. At the same time, the large conduction-band discontinuity between the strained AlAs in the barrier and the strained $In_{0.73}Ga_{0.27}As$ well allows short-wavelength laser emission.

### 3.4.5 Application outlook

Despite of the growing need for gas-sensing application, there was a little progress in 3-5 $\mu$m spectral region QCLs so far (see Fig. 3.27). Lasing wavelength engineering in this spectral range as well as high operation temperature performance of QCLs is pretty much limited by the available conduction band offset in InGaAs-InAlAs/InP material system.

Among the electrically driven semiconductor laser sources in 3-5 $\mu$m

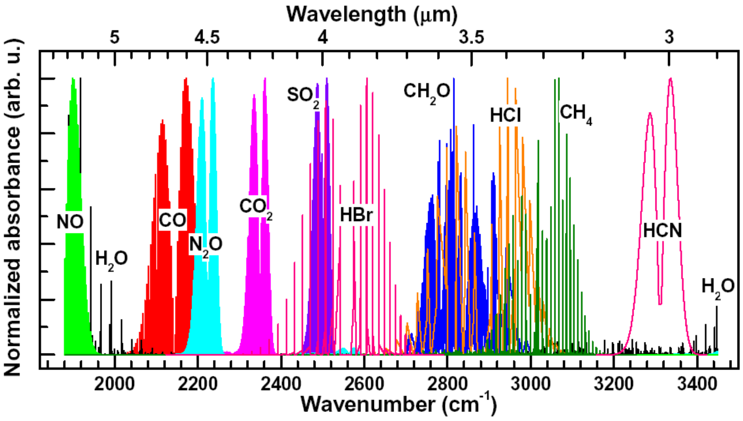

Figure 3.28: Normalized absorbance of organic gases within the first atmospheric window (Ref. HITRAN-database).

spectral range alternative to the QCLs one distinguishes: (i) the interband cascade lasers, IBCLs, (203; 202) and (ii) the led-salt lasers, LSLs, (204). In general, both the IBCLs and the LSLs demonstrate low performance at $\lambda > 3\mu$m, operating predominantly at cryogenic temperatures (see Fig. 3.27) and with low output powers. They very common feature is a low characteristic temperature $T_0$. Altogether, the interband lasers (IBCLs and LSLs) seems to be not an ideal solution for the laser sources in the first atmospheric window, 3–5 $\mu$m, spectral range.

Application of the QCL design strategy on the strain-compensated InGaAs-AlAs material combination has result in outstanding achievements in terms of the low threshold current density, output power, and maximum operation temperature. Demonstrated in current section laser (together with the very recent type-II IBCL (203)) are up to date the only two electrically driven semiconductor lasers operating at room temperature in 4.0–4.3 $\mu$m spectral range. A compact laser source in this range match perfectly for detection of $CO_2$ and $SO_2$ gases (see Fig. 3.28). Both of those gases are important for atmospheric pollution monitoring and medical applications.

## 3.5 Summary of chapter 3

To summarize chapter 3, we have

(i) **Explored the limits of utility of strain-compensation in InGaAs-InAlAs/InP material system**. We performed a consistent study of short-wavelength intersubband transitions in $In_{0.7}Ga_{0.3}As$-AlAs-$In_{0.55}Al_{0.45}As$ material system, grown strain-compensated on InP. Different design approaches were tested: multiple quantum wells, multiple double quantum wells, and superlattices. Short-wavelength intersubband transitions up to 1.55 $\mu$m are achieved in case of absorption.

(ii) **Utilized high conduction band offset of $In_{0.70}Ga_{0.30}As$-AlAs material combination for achieving the short-wavelength intersubband laser**. Basing on our experience on ISB transitions engineering on $In_{0.70}Ga_{0.30}As$-AlAs material, we have designed and realized a 3.7-to-4.3 $\mu$m QCL. The device demonstrates the **world-record** performance for this wavelength range in terms of maximum operation temperature, threshold current densities, output power and wall-plug efficiency.

# Chapter 4

# InGaAs-InGaP material system for QCLs application

## Preface

Among the GaAs-based materials, lattice-matched AlGaAs/GaAs, InGaP/GaAs, and InAlP/GaAs as well as strained AlGaAs/InGaAs material combinations have all found application in intersubband devices; the AlGaAs/GaAs materials system, in particular, has been used both for detectors (205) and quantum cascade lasers (QCL's) (3; 206). The maximum conduction band edge offset $\Delta E_c$ between direct band gap AlGaAs and GaAs is about 340–390 meV (207; 208), large enough to allow emission wavelengths in QCL's as short as 9 $\mu$m (208). Using strained InGaAs in the wells further increases $\Delta E_c$ and extends the emission wavelength range to 7.4 $\mu$m (209). The use of indirect band gap AlGaAs including AlAs, however, does not appreciably increase the maximum emission energy (140).

An alternative material system which is also latticed-matched to GaAs is the strain-compensated (In,Ga)P/(In,Ga)As system (210), the strain-compensated extension of $\mathrm{In_{0.49}Ga_{0.51}P}$/GaAs. Although $\Delta E_c$ in the lattice-matched $\mathrm{In_{0.49}Ga_{0.51}P}$/GaAs system is too small to use for mid-infrared QCL applications, the model-solid theory of Van de Walle (25) predicts a $\Delta E_c$ of 480 meV for $\mathrm{In_{0.32}Ga_{0.68}P/In_{0.32}Ga_{0.68}As}$, a combination where both materials can be epitaxial deposited and are direct band gap. *Up to the best of our knowledge there is only one report in the literature from the other group on study of* $In_xGa_{1-x}P$*-* $In_xGa_{1-x}As$ *strain-compensated material system on GaAs.* In present chapter we investigate $\mathrm{In_{0.32}Ga_{0.68}P}$- $\mathrm{In_{0.32}Ga_{0.68}As}$ material system in terms of

(i) growth optimization;

(ii) microscopic study of heterointerfaces;

(iii) determination of the relevant conduction band offsets;

(iv) intersubband transitions engineering in $In_{0.32}Ga_{0.68}P$-$In_{0.32}Ga_{0.68}As$ short period superlattices;

(v) study of the intersubband dynamics on the model samples;

(vi) quantum cascade test-structure design and characterization.

## 4.1 Material growth and basic characterization

### 4.1.1 Post-growth annealing study of $In_{0.32}Ga_{0.68}As$-$In_{0.32}Ga_{0.68}P$ superlattices

**Material outlook**

Al-free $In_xGa_{1-x}P/In_yGa_{1-y}As$ heterostructures are promising for device applications, because of the ease of selective etching (211; 212) and the possibility of regrowth steps (213). Thus this material system has been widely studied for different compositions ($x$,$y$), lattice matched to either GaAs or InP (214; 215; 216). If GaAs substrates are used, the small conduction band offset $\Delta E_c$ at the $In_{0.49}Ga_{0.51}P/GaAs$ heterointerface limits its application (217; 218; 219). For electronic, e.g. high electron mobility transistors (220) or opto-electronic devices based on interband or intersubband transitions (215; 216), a large $\Delta E_c$ is required. For this reason, the application of strain-compensated InGaP/InGaAs/GaAs heterostructures with higher conduction band offsets is of utmost interest.

When using single Ga and In sources and $x \neq y$ one has to change the source-cell temperature during the growth (which might employ long growth interruptions) or, when $x = y$, one has to deal with high strain ($> 1\%$). The latter case, furthermore, presents an additional challenge, in that arsenide/phosphide heterointerfaces tend to degrade for growth temperatures $T_{gr} > 450°C$ even for layers below the critical thickness (155; 221). To our knowledge, so far only one study (153) is devoted to the $In_xGa_{1-x}P/In_xGa_{1-x}As$ heterosystem. The $In_xGa_{1-x}P/In_xGa_{1-x}As$ system has an additional advantage: Because of the same In content in well and barrier, a possible group-III element intermixing (or In segregation) does not affect the heterointerface sharpness and the energy band profile. With regard to the group-V elements, a possible interdiffusion might smear the potential barrier within the quantum well (QW) but it does not form a layer, which might trap the carriers as InGaAs intermediate layers in InGaP/GaAs interfaces do (222). Moreover, Grandidier *et al.* (223) observe that the effect of intermixing on the heterointerface is much smaller when only the composition of group V elements is alternated (i.e. in $InAs_{0.21}P_{0.79}$/InP), in comparison with the case when both, the composition of group III and group V elements are changed as in the in $In_{0.39}Ga_{0.61}As_{0.93}P_{0.07}/InAs_{0.21}P_{0.79}$ system. Therefore, the use of the same of In/Ga ratio in both the barriers and the wells in the InGaAs/InGaP system should minimize the degree of heterointerface smearing.

In the present paper we describe in-situ RHEED, X-ray and optical studies of $In_{0.32}Ga_{0.68}P$-$In_{0.32}Ga_{0.68}As$ strain-compensated superlattices (SLs). The effect of different growth parameters as well as the impact post-growth thermal annealing is analyzed.

**Sample design**

Strain compensation in a multiple-layer structure promises a reduction of the defect density, an enhancement of the structural stability during post-growth treatments, and the possibility to grow a thick stack of alternatively strained layers. The structures grown were designed with a total strain of the structure close to zero. This means for an In composition of 0.3, the total InGaP thickness should be 1.6 times larger than the total InGaAs thickness. Each SL starts and finishes with an InGaP barrier. No cap-layer is grown on the top of the structures. The well and barrier widths are above the thermodynamic equilibrium thickness (164).

**Sample growth**

Our samples are grown in a conventional Riber-32 gas-source molecular-beam epitaxy (GSMBE) system equipped with arsine and phosphine as the sources of group-V elements. The hydrides, $PH_3$ and $AsH_3$, are decomposed at 850°C in low-pressure cracking cells; the main cracking products are PH and AsH. High purity (7N) solid In and Ga were used as the group-III element sources. The pressure in the MBE chamber under growth conditions is held in the $10^{-5}$ Torr range. The composition of group III elements is controlled by element cell temperature and monitored with an accuracy of a few tenths of a percent. The growth rate is determined with help of calibration samples. The layers thickness is reproducibly controlled with a precision down to 1 ML. RHEED is used for the *in-situ* surface control. Before the growth starts, the GaAs substrates are deoxidized at 630°C. A full oxide desorption is observed accompanied by the rise of thin RHEED streaks forming $2 \times 4\beta$ pattern. The 2000-Å-thick GaAs buffer layer is grown at 580°C with an arsine flux of 0.84 sccm. The first 100 ML of the buffer layer are grown with 20 interruptions of 1 min each to provide a smooth and atomically flat growth front. After the buffer layer growth, the substrate temperature ($T_s$) is decreased to the SL growth temperature of $T_{gr} < 500°C$ within 3 min. At $T_s = 520°C$, the arsine flux is switched off, maintaining the

(2×4) RHEED pattern and preventing an excess As coverage (recognized by a (2×1 RHEED pattern) before the InGaP deposition. An additional 2 minute pause is included to stabilize the substrate temperature. SLs with 6, 10, 20 and 50 periods as well as with various $In_{0.32}Ga_{0.68}As$ well and $In_{0.32}Ga_{0.68}P$ barrier thickness were grown at 350°C and 400°C. The growth cycle of one SL period consists of 8 steps, namely

1. a pause ($t_1$) under P flux to stabilize the phosphine flow and to obtain the P-terminated surface,
2. phosphide growth,
3. an interruption ($t_2$) under P flux to smooth the surface,
4. an interruption ($t_3$) without gas flux for removing the residual phosphine out of the growth chamber,
5. an interruption ($t_4$) under As flux to stabilize the arsine flow and to obtain the As-terminated surface,
6. arsenide growth,
7. an interruption ($t_5$) without any gas flux to vent residual arsine and
8. an interruption ($t_6$) under P flux to stabilize the phosphine flow.

#### In-situ RHEED observation

During growth of wells and barriers, the elemental $1 \times 1$ surface reconstruction is observed for both InGaAs and InGaP at growth temperatures ranged from 350°C to 400°C. For the gas switching steps, RHEED observations indicate a different surface morphology transformation on phosphide-to-arsenide and arsenide-to-phosphide heterointerfaces. A rather rough surface morphology (diffuse pattern) during the first $3-5$ seconds of As purge indicates an intensive P-to-As substitution. After 3 seconds, the surface flatness becomes improved, which is indicated by restoring sharp pattern. In contrast to the previous case, no pronounced transformation of the surface morphology is observed by RHEED for P termination of InGaAs surfaces and purging times as long as 20 s, indicating a relatively weak As-to-P substitution at the used temperatures.

#### Effect of growth interruptions variation

Double crystal X-ray rocking curves (DXRC) of 10 period SLs of nominally 5.3 $In_{0.32}Ga_{0.68}As$ and 6.0 nm $In_{0.32}Ga_{0.68}P$ grown with various growth interruptions are shown on Fig. 4.1. DXRCs are measured

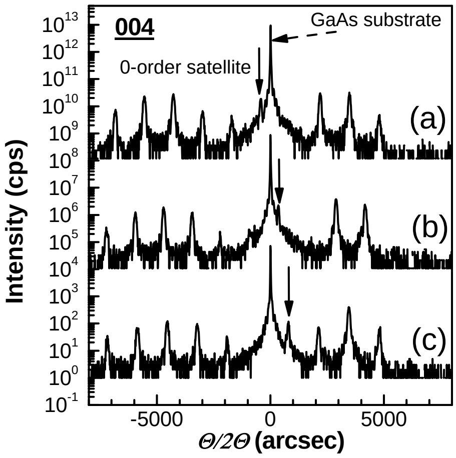

Figure 4.1: DXRC of 10 period SLs grown with the following growth interruptions on the heterointerfaces: a) AsH(3) purge $(t_4andt_5) = \mathrm{PH}_(3)$ purge $(t_1andt_2) =$ vent $(t_3andt_6) =$ 5 sec, b) PH(3) purge $(t_1)$ increased up to 20 sec, c) PH(3) purge $(t_1)$ increased up to 20 sec and AsH(3) purge $(t_4)$ decreased down to 0.5 sec. Rocking curves are shifted vertically for clarity. Growth temperature $T_{GR} = 360\circ$C in all the cases. All diffractions are (004). Solid arrows indicate the zero-order satellites of superlattice diffraction pattern. Dashed arrow indicate position of the GaAs substrate peak. Shift of zero order satellite is 780 arcseconds from (a) to (b), and 440 arcseconds from (b) to (c).

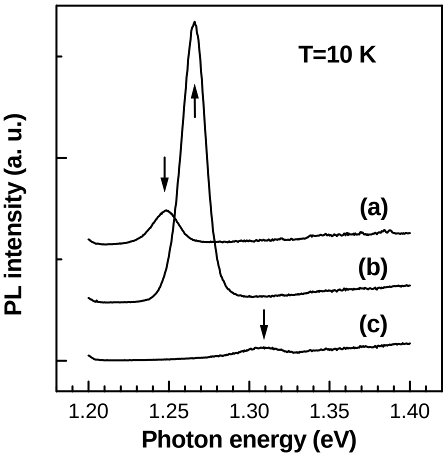

Figure 4.2: Steady-state photoluminescence spectra at $T = 10$ K of 10 period SLs grown with the following growth interruptions on the heterointerfaces: (a) $AsH_3$ purge ($t_4$ and $t_5$) = $PH_3$ purge ($t_1$ and $t_2$) = vent ($t_3$ and $t_6$) = 5 sec, (b) $PH_3$ purge ($t_1$) increased up to 20 sec, (c) $PH_3$ purge ($t_1$) increased up to 20 sec and $AsH_3$ purge ($t_4$) decreased down to 0.5 sec. Spectra are shifted vertically for clarity.

using a Bede Scientific QC1a double crystal diffractometer and simulated with the Bede RADS software. We assume that observed shift of the whole DXRC pattern on Fig. 4.1 is due to different contribution of As-P exchange process in presented set of the samples. It also worth to note, that the value of DXRC shift is comparable for the case of decrease of As purge by 4.5 sec (Fig. 2(a,b)) and increase of P purge by 15 sec (Fig. 4.1(b,c)).

For other set of samples, grown with the same growth interruptions, but slightly different temperatures in 350-to-400 °C range (data are not presented here) we have obtained identical DXRCs. DXRC satellites positions, however, are very sensitive to composition and layer thickness changes in a superlattice. Therefore, we neglect the effect of In composition or layer thickness uncertainty on the presented on Fig. 4.1 DXRC spectra.

The results obtained indicate that As-P interdiffusion is quite noticeable even at growth temperature as low as 360°C and As-into-InGaP incorporation is stronger than the P-into-InGaAs incorporation. Designing strain-compensated structures based on an arsenide-phosphide pair, one should either minimize the As and P termination time or evaluate and take into account the thickness of the layer created by P-to-As or As-to-P substitution.

Growth interruptions variation, and resulting As-P exchange, has a

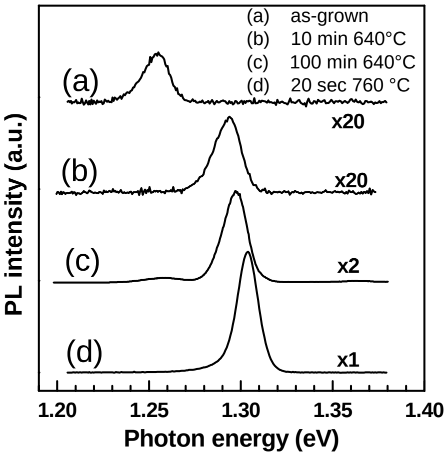

Figure 4.3: Steady-state photoluminescence spectra at $T = 10$ K of 4 samples from the same epitaxial run for different annealing conditions. Note the blue-shift by up to 50 meV and the associated luminescence increase by a factor of 50 that are cause by the RTA.

drastic impact on the heterointerface smoothness. Photoluminescence (PL) is known to be a sensitive tool to heterointerface roughnesses in quantum wells. Fig. 4.2 represents low temperature photoluminescence spectra of the same three samples, where the growth interruptions were varied. Great care was taken to acquire the spectra at the same conditions for comparison. PL intensity variation is huge: increase by 8 times, when increasing PH3 purge from 5 to 20 sec ((a)-(b)), and 35 times decrease, when decreasing AsH3 purge from 5 to 0.5 sec ((b)-(c)). Together with DXRC measurements this PL transformation reflects a crucial role of purging time when optimizing InGaAs-InGaP interfaces. We use the same In/Ga ratio in $In_{0.32}Ga_{0.68}As$ well and $In_{0.32}Ga_{0.68}P$ barrier. Therefore the both, increased substitution of As by P in $In_{0.32}Ga_{0.68}As$ or decreased substitution of P by As in $In_{0.32}Ga_{0.68}P$, will reduce the $In_{0.32}Ga_{0.68}As$ well thickness and increase by the same amount the $In_{0.32}Ga_{0.68}P$ barrier thickness. Spectral blue shift of PL peak (see Fig. 4.2) (as well as DXRC data) is consistent with such a narrowing of $In_{0.32}Ga_{0.68}As$ well.

A specific feature of many low-temperature grown materials is a relatively high density of non-radiative recombination centers. Thermal annealing is known (153) to improve the optical quality of material grown at low temperature. Thus we also study the effect of annealing on our structures.

Figure 4.3 shows the low-temperature steady-state PL behavior of samples for different annealing conditions. Obviously the annealing sub-

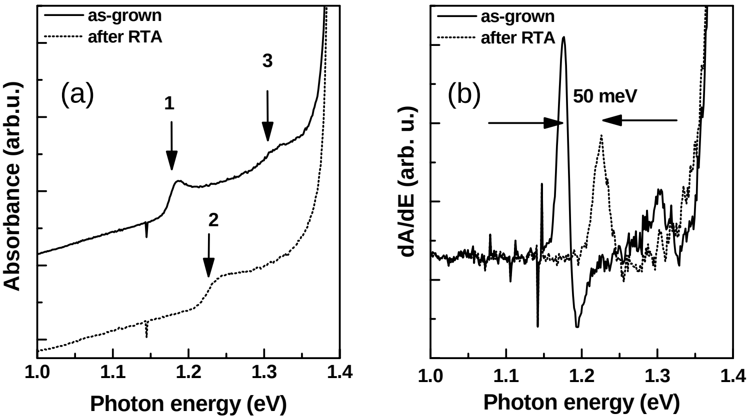

Figure 4.4: (a) Absorption spectra of superlattice SL1 at 300 K of the as-grown and the sample that experienced the RTA. Arrows 1 and 2 mark the $1_e - 1_{hh}$ transitions of as-grown sample and one after RTA. Arrow 3 - most likely corresponds to the $1_e - 1_{lh}$ transition. (b) First derivative of the spectra, presented on (a) part. The value of the blue shift is evaluated to be 50 meV.

stantially improves the PL properties. A PL intensity enhancement by a factor of up to 50, a remarkable decrease of the full width of half maximum (FWHM) from 18 meV to 13 meV, but also a blue-shift of about 50 meV are observed.

The above mentioned blue shift is confirmed by room-temperature absorbance measurements that are given in Fig. 4.4. At room temperature, all shallow donors and acceptors are fully ionized. So we relate the observed absorption edges, arrows 1-3 in Fig. 4.4(a), to interband electron-hole-pair generation. Edges 1 and 2 are $1_e - 1_{hh}$ transitions, and edge 3 is believed to be the $1_e - 1_{lh}$ one. The blue shift of 50 meV can be clearly evaluated from the plot of first derivative of absorbance, Fig. 4.4(b), which agrees well with our PL results.

Additionally, we perform time-resolved PL measurements for high energy ($E$ = 3.1 eV) impulsive fs-excitation at 10 K. For fs-excitation but time-integrated detection we obtain almost the same PL spectra as shown in Fig. 4.3, including the observed shift between the spectra from both samples. This demonstrates the absence of effects caused by hot electrons. Transient PL data with a temporal resolution of about 10 ps are given in Fig. 4.5. Except for one peculiarity, the transients of both samples demonstrate exactly the same behavior that is characterized by a 350 ps PL decay that most likely represents the total lifetime of non-equilibrium carriers within the QWs. A second more persistent component is caused by carrier accumulation due to the 82 MHz repe-

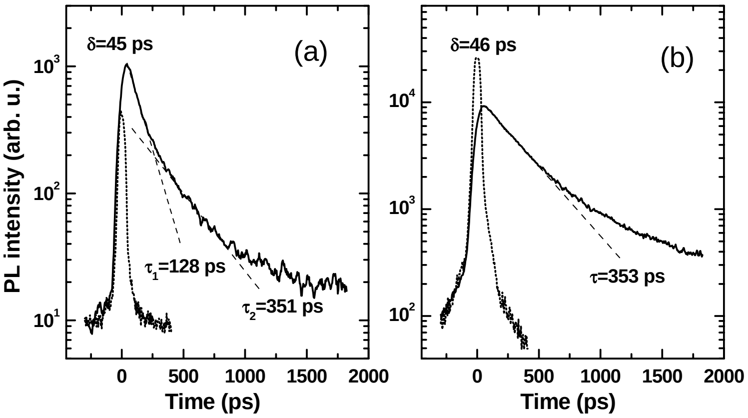

Figure 4.5: Transient photoluminescence decays at $T = 10$ K of the as-grown sample (measured at a detection energy of $E_{det} = 1.25$ eV) and the sample that experienced RTA (measured at $E_{det} = 1.30$ eV). For illustrating the over-all temporal resolution of the setup the excitation pulse at $E = 3.1$ eV is shown, as well. Note the absence of the fast saturable 130 ps component after RTA.

tition rate of the fs laser system. The most striking feature, however, is a fast transient that appears exclusively for the as-grown sample, cf. Fig. 4.5 on top. This fast but saturable decay can not be explained by intrinsic recombination but most likely directly visualizes carrier trapping. The non-radiative nature of this mechanism is proved by comparing PL spectra monitored at 250 and 600 ps, cf. abscissa scale in Fig. 4.5, i.e. in temporal windows where the 130 ps and 350 ps process dominate the recombination kinetics. No distinction is observed.

Now we discuss the observed behavior within the framework of the effects that might be involved into the annealing process

(i) strain relaxation at heterointerfaces,

(ii) smearing of potential well profile due to P-As post growth interdiffusion,

(iii) intrinsic defects generation/annihilation, and

(iv) the PL line of the as-grown sample might be considered defect related whereas after annealing interband recombination appears.

Regarding process (i), the observed PL line behavior contradicts the assumption of a thermally activated post-growth strain relaxation via dislocation generation, since this process should decrease the PL intensity and rather broaden the PL spectra. We do, however, observe a substantial increase of the PL intensity.

The reason for the blue shift of course can be (ii) or (iv), if one assumes that the observed PL emission is connected with intrinsic defects. But regarding the results of the transient PL measurement as well as the observed blue shift of the edge in room temperature absorption, the band-to-band nature of the observed PL emission for all samples becomes clear.

Hence, P-As intermixing is the most likely mechanism responsible for the observed PL transformation. The intermixing depth corresponding to the maximally observed blue shift of about 50 meV, evaluated by solving of the Schrödinger equation, is found to be $3-4$ ML per interface. We assume that this thermally activated intermixing is also enhanced by the alternating strain field on the heterointerfaces. It explains also the saturation of the blue shift value, when increasing the annealing time, as As-P interdiffusion reduces the heterointerface strain.

Process (iii), annihilation of traps is clearly shown by the transient PL as well as the non radiative nature of the transitions involving the traps. The detailed nature of the traps, however, can not be clarified within the frame of the present paper.

**Conclusions to the subsection 4.1.1**

To summarize, strain-compensated InGaAs/InGaP/GaAs SLs with well and barrier thicknesses higher than the corresponding theoretical critical thickness are grown using GSMBE at low growth temperatures (400°C and 350°C) on GaAs (001) substrates.

P substitution by As on InGaP/InGaAs interfaces takes place at $T_{gr} = 350°\mathrm{C}$ as well as at $T_{gr} = 400°\mathrm{C}$. X-ray analysis demonstrates that during 5 s As substitutes P within about 3 ML of InGaP. Employing As purging times as short as 0.5 s, it is possible to reduce the depth of P-to-As substitution substantially. Thermal annealing of InGaP/InGaAs strain-compensated SLs effectively reduces intrinsic non-radiative defects, improving PL intensity and FWHM. The observed spectral blueshift of the PL after annealing is shown to occur due to a band profile transformation caused by thermally activated P-As interdiffusion, enhanced by alternating strain on the heterointerfaces.

### 4.1.2 Heterointerface profile and alloy dis-order in lattice matched InGaP on GaAs

Heterojunctions between $\mathrm{In}_x\mathrm{Ga}_{1-x}\mathrm{P}$ (hereafter in the subsection InGaP) and GaAs have attracted attention recently because of their device applications. It has been predicted and confirmed that this system should have a large fraction of the total energy gap discontinuity occurring in the valence band, which improves the electron injection efficiency of an heterojunction bipolar transistor (HBT) (224). However, there exist discrepancies between band offsets results obtained by different techniques

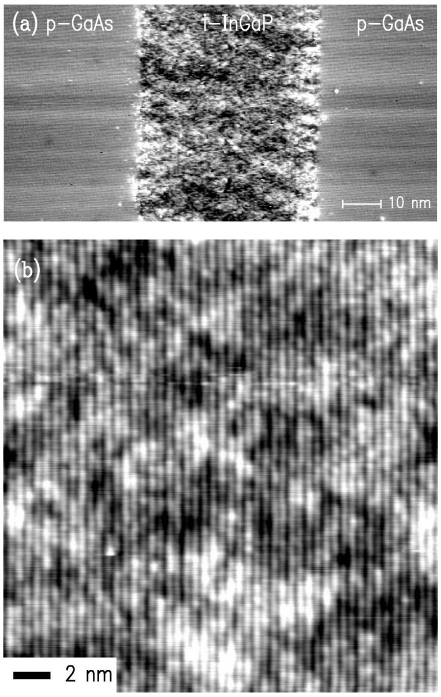

Figure 4.6: (a) STM topograph of p-GaAs/i-InGaP/p-GaAs heterostructure, acquired with sample voltage of 2.5 V. (b) High-resolution STM image of InGaP layer, acquired with sample voltage of -2.0 V. (filled states are imaged here). Growth direction is from right to left. *Courtesy: Y. Dong and R. M. Feenstra, Carnegie Mellon University.*

for samples grown by different methods/groups. It is known that properties of the interface depend sensitively on the detailed growth conditions (225; 226; 227; 228; 229). Prior experimental techniques used in this system are not spatially resolved and in order to better understand this material system a study of the atomic-scale structural and electronic properties of the junctions is useful.

A multilayer structure p-GaAs/i-InGaP/p-GaAs was grown on a p-type GaAs(001) substrate using GSMBE. The $\mathrm{In}_x\mathrm{Ga}_{1-x}\mathrm{P}$ was lattice matched to GaAs, with $x$=0.485 (growth temperature is 430 °C). GaAs layers are doped with Be at $1{\cdot}10^{18}$ $\mathrm{cm}^{-3}$, while the InGaP is not intentionally doped. The first GaAs layer growth is terminated with a 60 s purge of As. After 30 s venting, a short 3 s P exposure precedes the InGaP growth. An InGaP layer, nominally 500 Åthick, is grown, terminated with 30 s P soaking. Then, after 1 s venting, 5 s As exposure precedes the growth of second layer GaAs. An atomically flat $(1\bar{1}0)$ surface was exposed by cleavage in the STM chamber, under a background pressure of less than $5 \cdot 10^{-11}$ Torr. Commercial Pt-Ir probe tips are used.

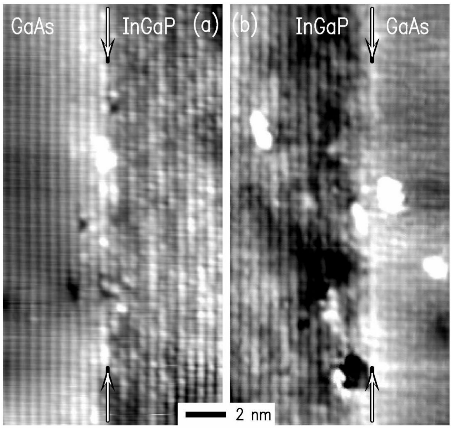

Figure 4.7: (a) STM topograph of GaAs-on-InGaP interface, acquired with sample voltage of -2.0 V. (b) STM topograph of InGaP-on-GaAs interface, acquired with sample voltage of -2.0 V. Growth direction is from right to left. *Courtesy: Y. Dong and R. M. Feenstra, Carnegie Mellon University.*

Topographic imaging is performed at a constant current of 0.1 nA and at sample voltages specified.

In the large-scale STM image of Fig. 4.6(a), the InGaP layer is seen in the center part of the image with GaAs layers seen on either side. Growth direction is from the right to the left for all images presented in this paper. The InGaP layer appears mottled due to compositional fluctuations in the alloy. A high-resolution image of the InGaP layer is shown in Fig. 4.6(b). At a sample bias of -2.0 V, filled states are imaged, i.e. localized on P atoms for InGaP. The pattern of different brightness for the P atoms reflects the distribution of neighboring In and Ga atoms. Because the cleaved surface is atomically flat, the observed contrast arises from a combination of electronic and strain effects, both associated with the presence in the alloy of clusters that are InP-rich or GaP-rich (230). Ordering of the alloy is an important phenomenon for InGaP. It has been found that, under certain growth conditions, the cations (Ga and In) are found to be ordered on $(\bar{1}11)$ or $(1\bar{1}1)$ planes (231; 232). From the STM images here, the InGaP layer does not display obvious ordering. Previous studies reveal that the 2K PL emission will change from 2.01 eV to 1.66 eV when InGaP layer goes from fully disordered to fully ordered (231). PL spectra at 2K from an InGaP sample with identical growth condition to the sample used here shows a peak energy of 1.97 eV. It is thus verified from PL that the InGaP layer studied here is very close to fully disordered.

Figures 4.7(a) and (b) show high-resolution images of inverted and normal InGaP/GaAs interfaces, respectively. Atoms on the group V sublattice are imaged here, i.e. revealing As atoms in GaAs and P atoms in InGaP. Arrows indicate the nominal position of the interfaces. The two interfaces display different features. For the GaAs-on-InGaP interface, the transition region is about 3-4 atomic bilayers (bilayer spacing is 5.65 Å) and most of it lies in the GaAs side. Some atom-size bright features are seen in the GaAs layer near the interface. We attribute these features to In atoms. The image of In atoms will appear brighter because In atoms are bigger than Ga atoms (also the band gap of InAs is smaller than that of GaAs, which would contribute to a larger tunnel current near In atoms (230)). Indium is known to segregate on InGaP surface (233; 234), and thus it will likely incorporate into following GaAs layer. It was proposed that the exchange of P atoms by As atoms is the main reason for degradation of interface abruptness, especially for GaAs-on-InGaP interfaces (225). Since the sizes of As atoms and P atoms along with the electronic structure of As-related and P-related compounds are different, the appearances of these atoms would be expected to be different in STM images. However it is difficult to observe As atoms inside InGaP layer since the InGaP layer is disordered here, showing a mottled image. Concerning P atoms on GaAs side, we would expect them to produce dark atomic-site features, but we do not observe a significant number of such features. We conclude that As/P interchange is not predominant at this interface. Turning to the InGaP-on-GaAs interface Fig. 4.7(b), the diffusion of atoms across the interface is not obvious. Large white features appearing in the image are cleavage-induced defects or residual surface contamination. A single atomic line just on the interface does appear brighter compared with its neighboring lines. That atomic line is probably InGaAs-like (a GaP-like interface would look dark). This result is consistent with our expectation from the growth conditions: The first GaAs layer growth is terminated with a 60 s purge of As. After 30 s venting, a short 3 s P exposure precedes the InGaP growth. It is unlikely that P atoms will replace As atoms during this time. This InGaP-on-GaAs interface is thus likely to be InGaAs-like rather than GaP-like.

To summarize, InGaP/GaAs heterostructures have been studied by cross-sectional scanning tunnelling microscopy and spectroscopy. A random InGaP alloy is observed. It is clearly seen that In atoms incorporate into the following GaAs layer. Both interfaces appear to be InGaAs-like for the growth sequence used here.

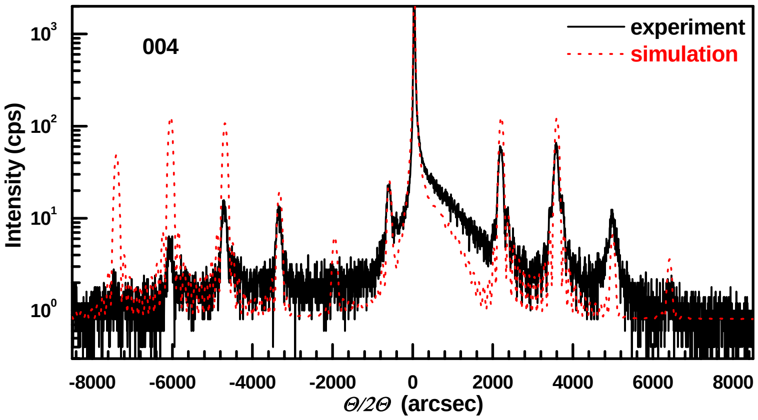

Figure 4.8: 004 reflection experimental DXRC of 10 period InGaAs-InGaP SL on GaAs, sample hub1105 (black solid line). Red dotted line is a simulated DXRC, assuming flat heterointerfaces.

### 4.1.3 Heterointerface profile in strain-compensated InGaP-InGaAs SL on GaAs

In subsection 4.1.1 we have already demonstrated, that even at low growth temperatures, 350-400 °C, As-P and P-As substitution on the InGaAs-InGaP and InGaP-InGaAs interfaces in strain-compensated SLs is significant. In this subsection we concentrate on the details of composition profile of $In_{0.32}Ga_{0.68}As$-$In_{0.32}Ga_{0.68}P$ interfaces, studied by the means of X-ray spectroscopy, transmission electron microscopy (TEM),and high-resolution (HR) TEM.

In following we will consider sample hub1105 grown at 400 °C on (001)GaAs substrates by GSMBE, as described in subsection 4.1.1. Used $AsH_3$ flux was 0.84 sccm, and $PH_3$ flux was 1.31 sccm. All the three steps of growth interruptions, addressed in subsection 4.1.1, were each 5 sec long.

Figure 4.8 depicts DXRC of sample hub1105 together with commercial software numerical simulation based on Dynamic Scattering Theory (BEDE Mercury). Intensity decay of high-order SL-satellites relatively the simulated DXRC-pattern indicates laterally nonhomogeneous heterointerface roughnesses/alloying. Similar problem with a fit of DXRCs was met for all the grown and analyzed strain-compensated InGaAs-InGaP structures. (In contrary, experimental DXRCs of common-anion strain–compensated InGaAs-InAlAs structures, see section 3.1, were almost perfectly simulated, indicating abrupt interfaces).

For deeper insight into the heterointerface properties we have performed TEM and HRTEM stusy of of the current two samples. Cross-

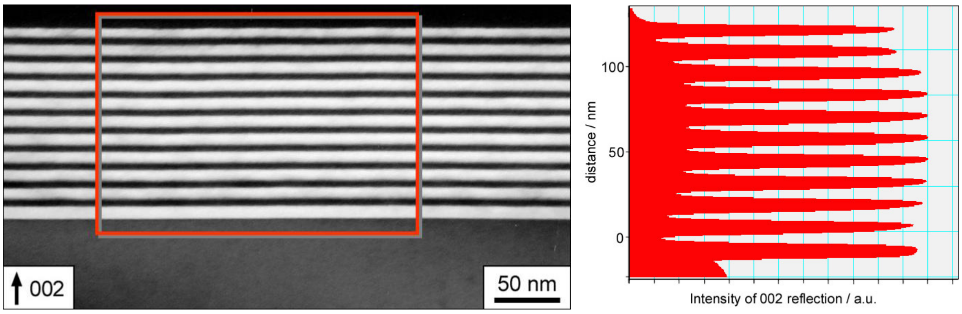

Figure 4.9: TEM dark-field image of superlattice hub1105 using the (002) reflection (left panel). Images were acquired capturing exclusively the (002) reflected beam within an aperture. Right panel shows vertical composition profile of the structure averaged over the 250nm×170nm area as indicated on the above photograph. Composition grading area is approximately 3 nm wide. *Courtesy: H. Kirmse and W. Neumann, Humboldt University Berlin, A. Klein, Ferdinand-Braun-Institut für Höchstfrequenztechnik.*

sectional samples are prepared by face-to-face gluing, followed by cutting of cylinders out of the stack perpendicular to the interfaces. The samples are mechanically subsequently thinned down to a thickness of about 30 $\mu$m. Finally, $Xe^+$ ion milling is applied using an accelerating voltage for the ions of 5 kV. The investigation of the structural properties of the SLs is performed on a TEM Hitachi H-8110 operating at 200 kV.

Figure 4.9 (left hand panel) shows a TEM dark-field image of hub1105 using the (002) reflection. For compound semiconductors having the sphalerite structure, the intensity of this reflection is mainly sensitive to the chemical composition. The brightness is proportional to the absolute difference between the mean atomic number of the cations and anions. Hence, the InGaP layers appear bright, whereas the InGaAs layers and the underlying GaAs look dark. The intensity inside the individual layers is almost constant, proving the almost homogeneous chemical composition. The interfaces between the layers of the SL show a high sharpness and the roughness tends to be smaller than 1 nm.

Figure 4.9 (right hand panel) shows the intensity profile in growth direction obtained by averaging over the indicated area on Fig. 4.9 (left hand panel). The interfaces between the layers of the SL show an approximately 3 nm wide compositional grading. Grading region is assumed to occur due to the P-As exchange during growth interruptions (as discussed in previous subsection). The (004) strain sensitive dark-field images of the SL structure (not shown here) show no dislocations in the structure.

An important detail, seen on fig. 4.9 is that the first InGaP barrier is slightly thicker, than the others; and the Last InGaP barrier is slightly thinner, than the others. However, growth time was kept the same for all. To discuss this feature, let us back into details of the growth procedure.

First, let us mention, that the (GaAs buffer)-(first InGaP layer) interface was grown differently, than the following interfaces of the InGaAs-InGaP SL (as was described in subsection 4.1.1). After GaAs growth was stopped and temperature was reduced below 500 °C, $AsH_3$ was vented out the MBE chamber during 2 min, which has resulted into transformation of arsenic-reach 2x1-reconstructed GaAs surface back into 2x4-reconstructed arsenic-stabilized surface. During the SL growth, however, only the 1x1-reconstructed surface was obtained, so we can not conclude what exactly was the arsenic/phosphor coverage. We can also *not* conclude if SL heterointerfaces were fully and uniformly terminated by the alternating anions during the growth interruptions.

Let us assume, that the growth front is not completely terminated by the next alternating anion during the interruptions during the SL growth. Then excess of previous anions interacting with incoming In and Ga cations will input into the thickness of previous layer because the (In,Ga)-composition is the same for InGaAs and InGaP. Such a scenario is not applied, however, for the fist GaAs-InGaP interface, because we are confident that GaAs buffer had a sub-monolayer arsenic coverage (2x4 reconstruction).

Finally, some cations from the every next alternating-anion layer make an input into the thickness of the previous layer all the way through the structure, except the very first interface between the GaAs buffer and the very first InGaP. Than the very last layer will bee indeed thinner, than others, because structure is uncapped. For the very first InGaP layer, its cations do not incorporate into GaAs buffer, but cations from the following InGaAs layer do input into the previous InGaP thickness. So, the very first InGaP will be indeed thicker.

Our tentative explanation of Fig. 4.9 has assumed up to now, that (In,Ga)-content is the same through all the SL. It is still possible, however, that there is preferable incorporation of Ga into InGaAs and In into InGaP, which if favorable for minimization of strain. But (In,Ga) composition gradient results into the weaker contrast (GaAs and InGaAs on Fig. 4.9), than P-As gradient (InGaP and InGaAs on Fig. 4.9), so it can not be analyzed yet.

Now we will go below the 1 nm scale, and into more detailed analysis of the interface profile by the means of HRTEM. We have performed HR-TEM scans on the same sample with (000), (002), and (004) reciprocal beams being integrated within the aperture. Figure 4.10 shows obtained high-resolution scan on the sample hub1105. Integrating over the the (000) specular beam reduces the contrast of picture, comparing

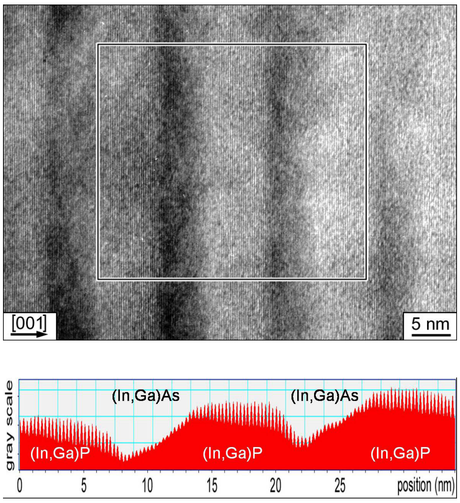

Figure 4.10: Dark field (002) material sensitive reflection of (a) hub 1105 and (b) hub 1111. Images were acquired integrating the three, (000), (002), and (004), reflected beams within an aperture. *Courtesy: H. Kirmse and W. Neumann, Humboldt University Berlin, A. Klein, Ferdinand-Braun-Institut für Höchstfrequenztechnik.*

the pure (002) reflection on Fig. 4.9. While integrating over the both (002) and (004) reflections gives us a combined picture of composition and strain relief. Both, the strain inhomogeneities and compositional inhomogeneities lead to the fluctuation of the material band gap, thus, both are important for consideration. Indeed, we observe on Fig. 4.10 lateral composition/strain inhomogeneities of 5 nm scale. In following we consider the influence of the heterointerface roughnesses on the properties of confined carriers.

To summarize, there are tree possible mechanisms leading into observed compositional grating and inhomogeneities on the InGaAs-InGaP interfaces:

(i) strain-driven segregation of In atoms out the compressively strained InGaAs with subsequent incorporation into the next tensile strained InGaP,

(ii) not the full As-termination of InGaP surface, and resulting strain-driven preferential gettering of In add-atoms by tensile strained InGaP,

(iii) residual As-P/P-As cross-contamination during the growth.

Obtained results convince us that all the three are relevant.

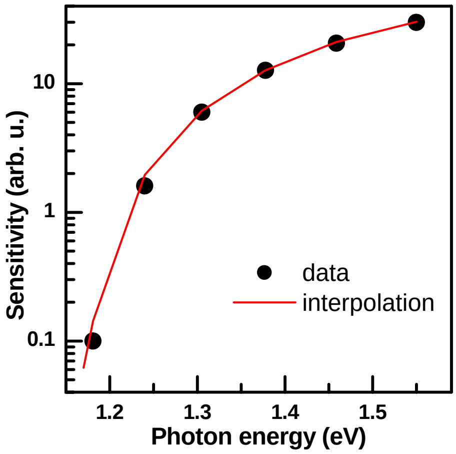

Figure 4.11: Spectral sensitivity of CCD detector array used in magnetoluminescence measurements.

### 4.1.4 Magnetoluminescence study of $In_{0.32}Ga_{0.68}As$-$In_{0.32}Ga_{0.68}P$ QWs

Goal of the experimental study, addressed in present subsection, is to determine an effective mass for pseudomorphically strained $In_{0.32}Ga_{0.68}As$ on GaAs. Magnetoluminescence measurements where carried out on the $In_{0.32}Ga_{0.68}As$-$In_{0.32}Ga_{0.68}P$ 26 period strain-compensated superlattice with 10 nm wells and 12 nm barriers, sample HUB1213. The structure is Si-doped in barriers. Low (20 K) temperature Hall measurements reveal $2 \cdot 10^{12}$ cm$-2$ sheet carrier concentration per well and $10^4$ cm$^2$/V·s mobility. Owing to thick barriers in this sample, it is pretty fair to treat it also as a multiple quantum well (MQW). Because the ground electron state in our 10 nm QW lays just ≈20 meV above the conduction band edge, we can treat obtained data as an approximation for the effective mass at the bottom of conduction band.

Measurements where done at two temperatures 10 K and 150 K. Magnetic field (0–14 T) was applied perpendicular to the epitaxial layers. The 514.5 nm $Ar^+$ laser line was used for PL excitation. Silicon array CCD camera was used as a detector. Figure 4.11 shows the normalized spectral sensitivity of the CCD camera. Sensitivity of used detector drops abruptly close to the PL in our structure. Therefore, all the spectra were corrected to account for the spectral shape of detector sensitivity. Such a processing of spectra has become as a source of partial distortion of PL lineshape (discussed below).

Figure 4.12 (a) shows the 10 K magnetoluminescence spectra of SL HUB1213 at various magnetic fields. Spectra do comprise characteristic

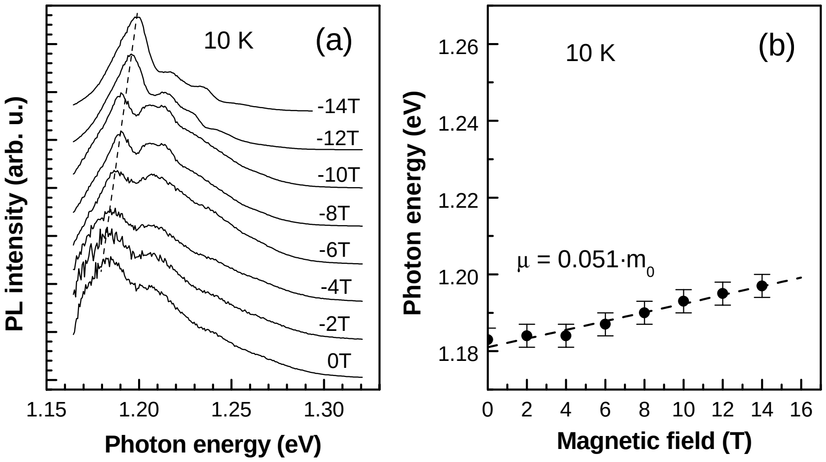

Figure 4.12: (a) 10 K magnetoluminescence spectra of 26 period 10 nm $\mathrm{In_{0.32}Ga_{0.68}As}$- 12 nm $\mathrm{In_{0.32}Ga_{0.68}P}$ SL, sample HUB1213, at various magnetic fields, as indicated. Dashed line tracks the spectral shift between zeroth Landau levels of electron and heavy hole with magnetic field. Transitions from higher Landau levels are hardly resolved. Dip at 1.198 eV in spectrum acquired at B=0T is an artifact due to the correction of spectra according to the spectral sensitivity of detector. (b) spectral position of the ground Landau level (solid circles) at 10 K vs magnetic field. Dashed line is calculated after eq. 2.39 spectral position of the ground Landau level, assuming a value of reduced mass for electron-hole pair $\mu = (0.051 \pm 0.001) \cdot m_0$.

Landau level splitting for degenerated electron gas due to the quantization of lateral motion in perpendicular magnetic field. Because of the pure the broadening of the individual transitions we reliably track (see Fig. 4.12) a spectral shift of the lowest energy transition solely (the transition between the electron and hole states with zero principal Landau index $N$).

Generally, due to selection rules (235) for the electron-hole transitions in the magnetic field, transitions are possible only between electrons and holes states with the same quantum numbers. Photoexcited holes relax to the topmost hole state usually within sub-picosecond time frame. This is of few order of magnitude faster than electron-hole recombination. Thus, holes are distributed in the very neighborhood of the zero momentum in $k$-space. At sufficiently high magnetic fields and low temperature the hole states with the non-zero Landau index will be not populated, and corresponding transitions will not take a place. The situation changes in the presence of localized hole states. Localization in real space spreads the carrier wavefunction in $k$-space (following the Heisenberg Uncertainty Principle). Then electron-hole transitions at non-zero values of $k$-vector becomes possible. (Note, that $k$-vector space of conduction band is populated up to $k_F = \sqrt{2\pi n_{2D}}$ at low temperature due to doping). Localization of holes can occur due to the heterointerface roughnesses in heterostructures, on on Coulomb potential of acceptors, on alloy fluctuations, so on. In case of the hole localization by acceptor, momentum selection rule brakes. In this case a series of "forbidden" transitions between electron and hole states with not equal Landau indexes take place (236; 237). Such a scenario usually develops at low temperatures. At high temperatures the high-Landau-index hole states will be thermally populated. Then the intensity of transitions between the electron and hole states with the same Landau indexes increase and overcome the intensity of momentum-indirect transitions. Due to the thermal broadening of states one resolve then only direct, $N_e = N_h$, transitions at high temperatures(237).

Indeed, at 150 K (see Fig. 4.13 (a)) the shape of the magnetoluminescence spectra changes, comparing the spectra acquired at 10 K (see Fig. 4.13 (a)). At 150 K transitions between the individual Landau levels are better resolved, likely, due to the thermal population of the high-Landau-index hole states (as discussed above). Here we can observe three different $N_e \rightarrow N_h$ transitions: $0 \rightarrow 0$, $1 \rightarrow 1$, and $2 \rightarrow 2$, where $N_e$ and $N_h$ are the principal Landau indexes for electron and hole correspondingly.

$$N = \frac{n + m_l}{2}, \tag{4.1}$$

where $n$ is a principle quantum number ($n = 1, 2, 3, \ldots$), $m_l$ is a magnetic

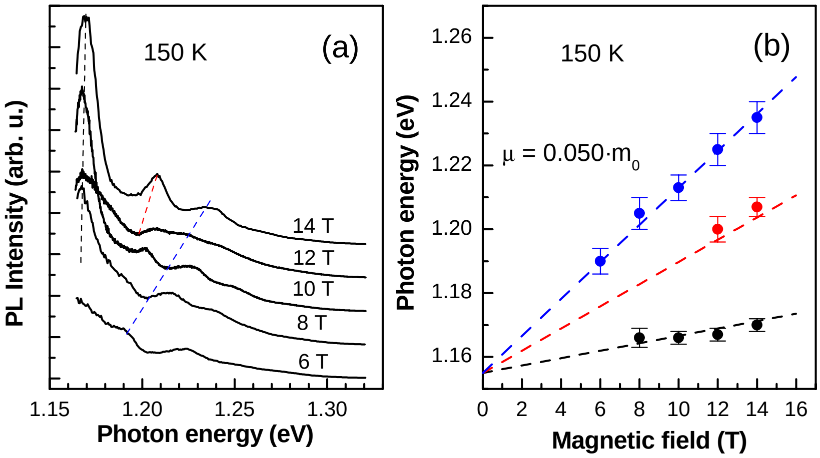

Figure 4.13: (a) 150 K magnetoluminescence spectra of HUB1213 sample (as on Fig. 4.12) at various indicated magnetic fields. Dashed lines track the first three Landau levels spectral shift with magnetic field. At B≤6T the spectral position from ground Landau level is out of the spectral range of experimental setup, therefore spectra at low magnetic field are not included. (b) spectral position of Landau levels (solid circles) at 150 K vs magnetic field. Dashed lines are calculated after eq. 2.39 spectral position of Landau levels, assuming a value of reduced mass for electron-hole pair $\mu = (0.050 \pm 0.001) \cdot m_0$.

quantum number ($m_l = -l, -l+1, \ldots, l$), and $l$ is an azimuthal quantum number ($l = 0, 1, 2, \ldots, n-1$).

Both 150 K and 10 K data do accomplish each other. High temperature measurements allow to observe the direct ($N_e = N_h$) transitions between the Landau levels. The low temperature measurements allow to observe the indirect ($N_e \neq N_h$) transitions between the Landau levels together with direct $0 \rightarrow 0$ transition (which is in the sensitivity range of detector in this case).

Now we consider the spectral shift of resolved transitions with magnetic field. Both data-sets were used to fit the spectral positions of transitions between the electron and holes Landau states. Figures 4.13 (b) and 4.12 (b) plot the experimental data (solid symbols) and calculated energies (dashed curves) of transitions between 0-th, 1-st, and 2-nd electron and hole Landau levels at different magnetic fields. By fitting the transition energy data with Eq. 2.39 we have determined the zero magnetic field transition energy of 1.181 eV at 10 K and 1.155 eV at 150 K. Best fit of 0 K and 150 K experimental data with eq. 2.39 was obtained with (0.051±0.001) × $m_0$ value of reduced mass of electron-hole pair at

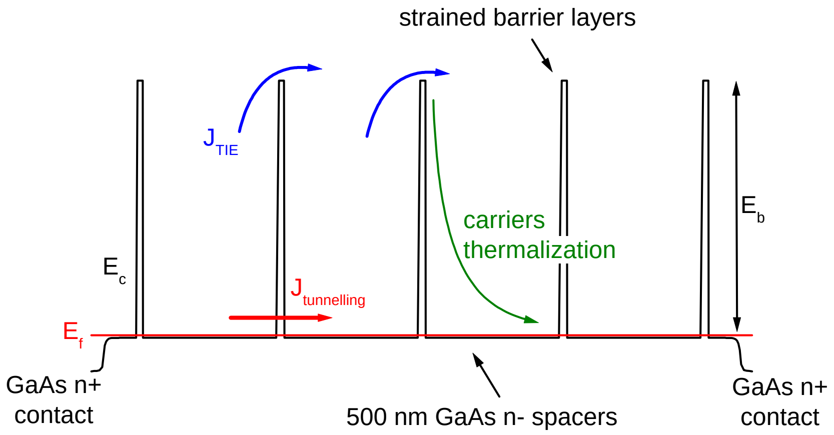

Figure 4.14: Conduction band profile of the vertical structure with five 10 nm thick intrinsic barriers within a bulk $n$-type GaAs, $n = 1 \cdot 10^{17} cm^{-3}$, and with $n+$ GaAs,$n = 5 \cdot 10^{18} cm^{-3}$, contacts at the sides.

10 K and $(0.050 \pm 0.001) \times m_0$ value of reduced mass of electron-hole pair at 150 K. We can fairly assume the hole mass to be in the range of $(0.350 - 0.550) \times m_0$, which will lead to $m_e^* = (0.058 \pm 0.003) \times m_0$ at low temperature.

To summarize, using magnetoluminescence data and theoretical modelling we have obtained the effective mass for pseudomorphically strained $In_{0.32}Ga_{0.68}As$ on GaAs, which is a crucial parameter for modelling of intersubband transitions in studied $In_{0.32}Ga_{0.68}As$-$In_{0.32}Ga_{0.68}P$ material system.

## 4.2 Conduction band offset determination for InGaP-GaAs and InAlP-GaAs interfaces

### 4.2.1 Determination of small conduction band offset in highly strained heterosystems

The conduction band offset (CBO) in heterostructures is often determined by measuring thermionic emission current in n-i-n structures as a function of temperature and voltage (238), see eq. 4.2.

$$J = A \cdot T^2 \cdot e^{\frac{E_b}{k_B T}}, \tag{4.2}$$

where $A$ is the Richardson constant, $k_B$ is the Boltzmann constant, $T$ is a carrier temperature, and $E_b$ is a height of potential barrier, which the carriers overcome.

The total resistance of such structures (say, for a given voltage) is determined by the mesa size, thickness of intrinsic layer, and the CBO (at other parameters being fixed). To obtain a reliable value, the intrinsic layer contribution to the total resistance should be significantly larger than the resistance of the ohmic contacts. And when the CBO is small, the determination of its value becomes challenging due to the huge thermionic emission current. Another challenging case we meet, when dealing with strained materials. Intrinsic layer thickness, than, should not overcome the *critical thickness* (163). In case of the high strain it leads into thin layers and, consequently, high tunnelling current.

The intrinsic resistance can be increased, however, by stacking a number of barrier-layers with a thick n-type spacer layers between them (see fig. 4.14). Spacer needs to be thick enough to let to thermalize again all the hot electrons, which came over the previous barrier. i.e. the electrons need to undergo a series of scattering events before they rich the next barrier layer. Otherwise the characteristics temperature of the electron gas in between the barriers will differ from the lattice temperature, and application of the thermionic emission model (in the way of Eq. 4.2) will be not valid. And the spacer should be properly uniformly doped to fix the Fermi level relatively the conduction band.

Such a design can have an additional advantage in case if strained barrier material is used. Then accurate determination of strained layer composition is possible (see fig. 4.17 for example) via X-ray rocking curves modelling (as increased overall volume of strained material induce the intensity of correspondent X-ray reflexes). Which provides a very useful feedback on design parameters.

### 4.2.2 Conduction band edge offset on $\mathrm{In_{0.32}Ga_{0.68}P}$-GaAs interface

We demonstrate the utility of this approach, measuring the CBO of $\mathrm{In_{0.32}Ga_{0.68}P}$ relatively to GaAs. A huge spread of conduction band offset (CBO) data for InGaP/GaAs heterointerface (181) reflects a high sensitivity of this material pair to the growth technique. Ordering effect in InGaP (239) allows to model CBO by just alternating the growth conditions (240). Possibility of As-P cross-contamination might introduce another degree of disagreement between available data. That is why control of CBO parameter for such a material grown at certain conditions, is important. Present $\mathrm{In_{0.32}Ga_{0.68}P}$ composition is of special interest, because close to this In content the $\Gamma$-X valleys crossover takes place (181).

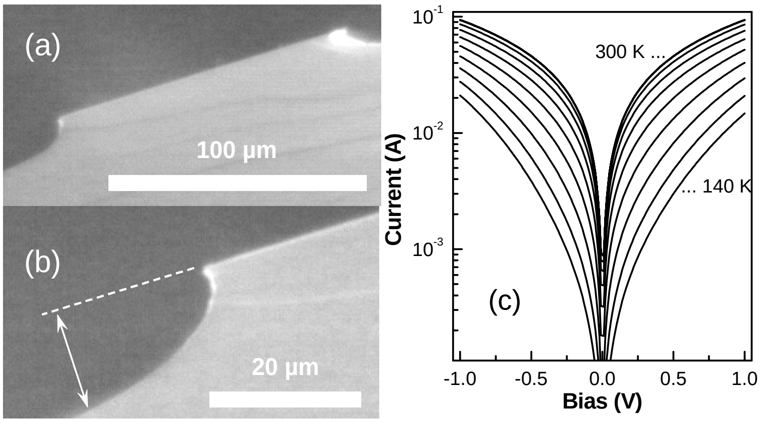

Figure 4.15: (a) and (b) optical microscope images of a cleave through the center of $\sim 100\mu$m diameter mesa of a InGaP-GaAs multi-barrier structure (hub1409). Arrow on (b) indicate the etching depth of $\approx 17\mu$m. (c) current-voltage characteristics of a 200 $\mu$m diameter mesa (of hub1409) acquired in the specified temperature range.

Chosen In content, meanwhile, let us utilize all the advantages of the new approach due to high mismatch to GaAs.

Sample, grown by gas source MBE, consist of 5 undoped 10 nm thick $In_{0.32}Ga_{0.68}P$ barriers. Thick 500 nm GaAs spacer layers, doped with Si to $n = 10^{17}$ cm$^{-3}$, are introduced in between the barriers to let to thermalize again all the hot electrons, which came over the previous barrier. Fermi level is calculated to be 8 meV above the GaAs conduction band. Such a superlattice is put between the two 300 nm GaAs doped with Si to $n = 10^{17}$ cm$^{-3}$ layers. Highly doped $n$-type GaAs:Si $5 \cdot 10^{18}$ cm$^{-3}$ substrate on one side and a 1300 nm GaAs:Si $5 \cdot 10^{18}$ cm$^{-3}$ layer on another side serve as contact regions.

Alloyed 400 nm thick Au:Ge Ohmic contacts were performed. 200 $\mu$m diameter round mesas where etched down to the substrate through all the barriers (all together $\sim 4\mu$m) with HF:HNO3:H2O (1:1:1) solution. This solution etches effectively both GaAs and InGaP, and allowed to obtain almost vertical sidewalls of mesas (see fig. 4.15 (a) and (b)). Approximately 17 $\mu$m etching depth depth was achieved during 60 sec (shown by arrow on fig. 4.15 (b)).

After mesa bonding and sample mounting in closed cycle cryostat the current voltage characteristics were acquired at the 140-300 K temperature range, fig. 4.15 (c).

The data fit the thermionic emission model in the 300 K - 180 K temperature range very well, fig. 4.16 (a), and the $In_{0.32}Ga_{0.68}P$-GaAs CBO is determined to be 90 meV. A similar experiment using a single

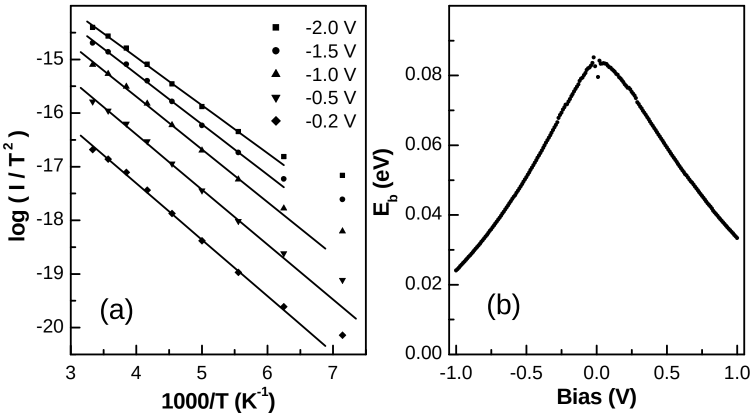

Figure 4.16: (a) Ahrenius plot of the current vs temperature at different biases for the 200 $\mu$m mesa of hub1409 (solid symbols). Solid lines are the best fit of the data-set following eq. 4.2 at given biases. Deduced from the fit barrier height, $E_b$, relatively the Fermi level vs bias is plotted on (b).

barrier does not, however, lead to consistent result on CBO.

### 4.2.3 Conduction band edge offset on $In_{0.58}Al_{0.42}P$-GaAs interface

Due to a small $In_{0.32}Ga_{0.68}P$-GaAs CBO obtained, exploiting of $In_{0.32}Ga_{0.68}P$ as a the only barrier material in GaAs-based QCL looks feasible. In particular, the problem appears to inject carriers from the GaAs waveguide into InGaAs-InGaP active region. Therefore, it becomes necessary to modify somehow the new material choice. One possibility is to include a third material, for example AlGaAs or InAlP. AlGaAs is lattice matched to GaAs at the whole Al-composition range. And band parameters of AlGaAs are very well known. InAlP is lattice matched to GaAs at 48% In-composition. Γ-X valley crossover in InAlP occurs at ≈ 56% of In composition (181). Therefore all the direct band gap InAlP alloys are compressively strained on GaAs. And band parameters for such alloys are usually determined by extrapolation of those for lattice-matched InAlP. There are no direct measurements reported, to the best of our knowledge, for the CBO between GaAs and strained InAlP. However, namely the strained $In_{0.56}Al_{0.44}P$ alloy satisfies the both: (i) maximum CBO relatively GaAs and (ii) direct band gap material conditions.

Farther we present our results on CBO determination for $In_{0.58}Al_{0.42}P$-GaAs interface using the same technique as in previous sub-

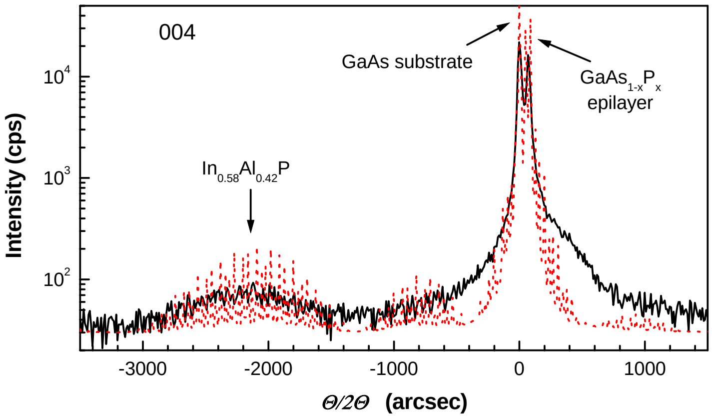

Figure 4.17: Experimental double crystal rocking curve, DXRC, black line, and dynamic scattering theory simulation of DXRC, red dots, of five $In_{0.58}Al_{0.42}P$ barrier structure (hub 1408). Through DXRC modelling the exact In-content of barriers is deduced. Splitting between the GaAs substrate peak and GaAs epilayer one occurs due to the background phosphor incorporation into the epilayer from the growth chamber.

section. Small deviation of the In composition from 56% towards the higher In content was chosen as a preferable to be more sure, that the alloy is a direct band gap material.

### 4.2.4 Conduction band edge offset on $In_{0.48}Ga_{0.52}P$-GaAs interface

$In_{0.48}Ga_{0.52}P$-GaAs band offset was measured using the same technique as above. However, processed mesas were low ohmic, and obtained I-V characteristics do not fit to the thermionic emission model. From this we assume the zero CBO on the $In_{0.48}Ga_{0.52}P$-GaAs interface. Independent study of similar structures by scanning tunnelling spectroscopy (241) has brought us to exactly the same conclusion.

### 4.2.5 Discussion of obtained CBO values

The 90 meV $In_{0.32}Ga_{0.68}P$-GaAs CBO is appeared to be of ≈240 meV smaller than one would expect from the model solid theory calculations (25). $In_{0.48}Ga_{0.52}P$-GaAs interface, however, revealed the negligible CBO, ≈0 meV, while the same theory gives the value of 230 meV (25). So, both results are approximately the same value, 230-240 meV, below those given by theory. At the same time 460 meV CBO between GaAs and $In_{0.58}Al_{0.42}P$ agrees well with the value of 480 meV deduced from

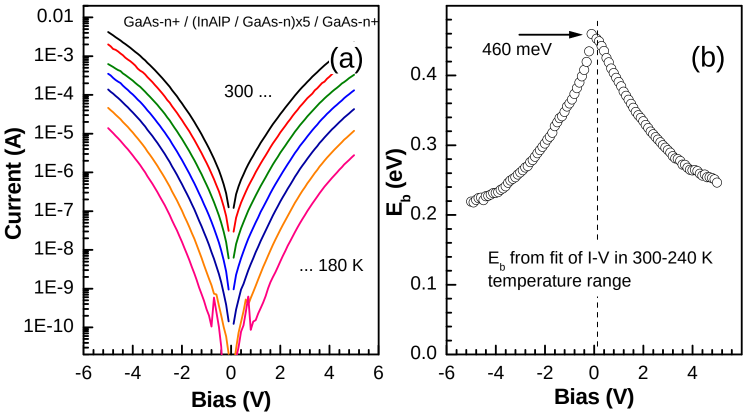

Figure 4.18: (a) current voltage characteristics of the InAlP-GaAs multibarrier structure, hub1408, acquired at specified temperatures. (b) barrier height, $E_b$, relatively the Fermi level vs the bias voltage, deduced from the temperature dependence of I-V characteristics following the thermionic emission model, eq. 4.2

the compilation of the experimental data (181). Because the growth conditions for InGaP and InAlP where the same (and CBO obtained on InAlP-GaAs structures agrees well with tabulated data (181)), we exclude any growth related artifacts, like the presence of the interface or the bulk charge. Despite of systematic deviation of obtained InGaP-GaAs CBO from the theoretical values (25), they, however, agree well with a number of reported experimental values, obtained on the MBE (242; 218) and MOCVD (219) grown samples. It might look somehow contradictive, that we did not compare at all our results with those, recommended by Vurgaftman's review, Ref. (181). Such a comparison, however, would make no sense, because Ref. (181) gives the averaged values over the MBE- and MOCVD-grown samples. We believe that in particular case of InGaP such a mixing of MBE and MOCVD results is dangerous, because in case of MOCVD InGaP properties are known to depend drastically on the growth conditions (240).

## 4.3 Mid-infrared intersubband absorption in InGaP-InGaAs superlattices on GaAs

In this section intersubband optical transitions in strain-compensated $In_{0.32}Ga_{0.68}As$- $In_{0.32}Ga_{0.68}P$ superlattices grown using gas-source molecular-beam epitaxy on (001)GaAs are investigated by means of mid-infrared absorption and low-temperature photoluminescence. Strong ab-

Table 4.1: Sample parameters.

| No. | $N_{2D}$ (cm$^{-2}$/well) | $\mu_{300K}$ (cm$^2$/V·s) | $L_W$ (nm) | $L_B$ (nm) | $\Delta a/a$ (ppm) | Periods |
|---|---|---|---|---|---|---|
| A13, hub1213 | $2 \times 10^{12}$ | 3900 | 10.0 | 12.4 | 2724 | 26 |
| A14, hub1214 | $1.4 \times 10^{12}$ | 2650 | 5.7 | 9.8 | 187 | 51 |
| A07, hub1207 | $6 \times 10^{11}$ | 2300 | 5.6 | 10.2 | -194 | 50 |
| A15, hub1215 | $1.45 \times 10^{12}$ | 1200 | 4.0 | 6.6 | 634 | 51 |
| A16, hub1216 | $6 \times 10^{11}$ | 690 | 3.2 | 4.5 | 1679 | 51 |
| A17, hub1217 | $4.8 \times 10^{10}$ | 530 | 2.2 | 3.2 | 1530 | 101 |
| A35, hub1235 | undoped | - | 1.2 | 1.6 | 2163 | 100 |

sorption corresponding to the transition from the first to second electronic subband is measured at wavelengths between 5.6 and 10.5 $\mu$m. The data indicate that the conduction band offset between the strained $In_{0.32}Ga_{0.68}As$ and the strained $In_{0.32}Ga_{0.68}P$ is 370 meV and the electron effective mass in the strained $In_{0.32}Ga_{0.68}As$ well is of $0.060m_0$. Obtained results indicate that this material system is an interesting GaAs-based candidate for applications in mid-infrared intersubband emitters and detectors.

### 4.3.1 Sample design

Superlattices composed of $In_{0.32}Ga_{0.68}P$- $In_{0.32}Ga_{0.68}As$ are grown using GSMBE in semi-insulating GaAs (001) substrates. Following a GaAs buffer layer, the growth temperature is reduced to nominally 350° C; a low growth temperature is important for maximizing the critical layer thickness for two-dimensional growth in this internally highly-strained system (153). The InGaP/InGaAs superlattice is then grown at 0.18 nm/s growth rate using cracked $AsH_3$ and $PH_3$ fluxes of 1.0 and 1.6 sccm, respectively. Because both the InGaP and the InGaAs have the same In and Ga composition, we use single Ga and In effusion cells. (For both the $In_yGa_{1-y}As$ and the $In_yGa_{1-y}P$, the In content is optimized for $0.25 \lesssim y \lesssim 0.35$ so that the barrier is direct, $\Delta E_c$ is maximized, and the InGaAs remains pseudomorphic.) During the growth of both materials, the RHEED shows a sharp elemental $1 \times 1$ surface reconstruction. To minimize As–P substitution, the switching time between $AsH_3$ and $PH_3$ is limited to 1.5 s.

The internal lattice mismatch values are $\Delta a/a = -1.4\%$ for $In_{0.32}Ga_{0.68}P$ compared to GaAs and $\Delta a/a = +2.4\%$ for $In_{0.32}Ga_{0.68}As$

compared to GaAs. The total mismatch of the strain-compensated structures is as low as 187 ppm. The required occupation of the lowest conduction subband in the InGaAs is achieved by doping the InGaP barriers with Si, resulting in sheet densities in the InGaAs wells of about $1 \times 10^{12}$ cm$^{-2}$ per well, as determined from Hall measurements. Parameters of the structures investigated are given in Table 4.1.

### 4.3.2 Intersubband absorption measurements

Intersubband absorption measurements are carried out using a Bio-Rad FTS-45A Fourier spectrometer with the samples in a 48° waveguide wedge geometry as described in Ref. (243). Figure 4.19 shows the room temperature absorption spectra of p-polarized incident light. (The s-polarization shows essentially no absorption.) Intersubband transitions between the first and second subbands are measured for samples with well thicknesses from 3.2 to 10 nm and cover the spectral range from 5.6 to 12 $\mu$m (100-220 meV). As the well width is decreased, the $E_1 - E_2$ transition energy gradually increases, reaching a maximum for well width of about 4 nm, and then again becomes smaller for well widths less than 4 nm as seen in Fig. 4.19. In our measurements, the width of the absorption peak is about 30 meV for samples with well width $> 4$ nm, but was somewhat larger (41 meV) for the structure with the 3.2-nm wells and reduced transition energy. No absorption line was detected in Sample A17 with 2.2-nm wells either because the wells are too narrow to allow a second subband or because the electron concentration is too low.

### 4.3.3 Theoretical analysis

To model the relationship between the band structure and the subband energies in our structures, we use the envelope function approximation model for superlattices (19). Non-parabolicity of the conduction band is included by way of an energy dependent effective mass, as described in Ref. (84). The effect of strain on the conduction and valence bands is calculated following Van de Walle (25). The conduction band offset $\Delta E_c$ is expected to be between 300 and 500 meV based on the model-solid theory (and corrected based on InGaP/GaAs experimental results (244; 242)) and is treated as a fitting parameter. Interdiffusion at the heterointerfaces is included by adding a linearly graded $\mathrm{In_{0.32}Ga_{0.68}As}_y\mathrm{P}_{1-y}$ layer at each interface. The presence of a thin intermediate layer is consistent with preliminary high-resolution transmission electron microscopy investigations (245). The interdiffusion layer thickness is a second fitting parameter and is necessary to allow the simultaneous fit of interband photoluminescence and intersubband absorption data.

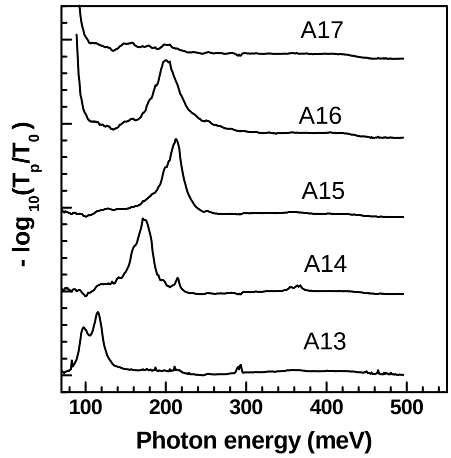

Figure 4.19: Room temperature mid-infrared absorption spectra of the samples listed in Table 4.1. Spectra are vertically shifted for clarity. The FWHM for A13, A14, A15, and A16 are 29, 27, 28, and 41 meV, respectively.

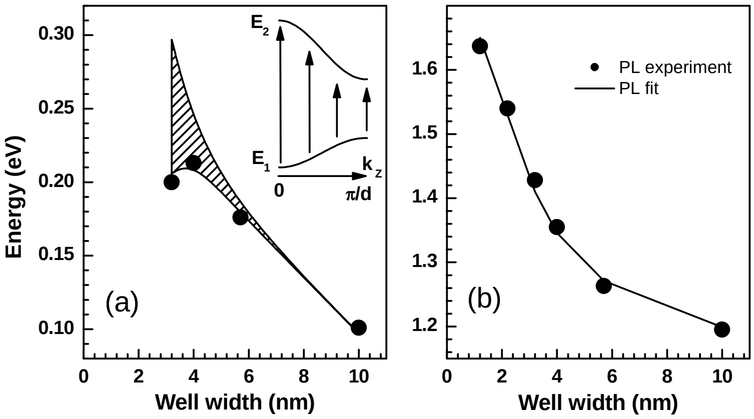

Figure 4.20: (a) Energy of room temperature intersubband absorption maxima for samples A13-A16 and A07. The cross-hatched area is the range of the calculated $E_1 - E_2$ transition energies for different $k_z$ as described in the text. (b) Energies of the $E_1 - HH_1$ transition energies determined from 10-K photoluminescence. The solid curve is the calculated $E_1 - HH_1$ transition energy including As-P intermixing at the heterointerfaces.

Figure 4.20(a) depicts the calculated range of $E_1 - E_2$ transition energies $E_{1-2}$ as a function of well width for the $\mathrm{In_{0.32}Ga_{0.68}P/In_{0.32}Ga_{0.68}As}$ superlattices listed in Table 4.1 together with the experimental positions of the interminiband absorption maxima. The top of the energy range corresponds to $k_z = 0$ and the bottom to $k_z = \pi/d$, where $d$ is the superlattice period. The doping level is sufficient to ensure that the Fermi level is always above the first electron miniband. The exact energy $E_{1-2}$ is determined by using a line-shape analysis of intersubband absorption (54) which indicates that the peak energy lies slightly above the $E_1 - E_2$ transition at $k_z = \pi/d$ in the case of the ground electron miniband being filled. (The transition oscillator strength at $k_z = \pi/d$ dominates that at $k_z = 0$ because the electron effective mass in the $k_z$ direction is negative near the edge of the superlattice mini-Brillouin zone (54).) Including the conduction band non-parabolicity, and As-P interdiffusion, the intersubband absorption data can be fit with a $\Delta E_c = 400 \pm 50$ meV for realistic degrees of interdiffusion.

Requiring that the interband photoluminescence data also be fit further constrains the values of the two fitting parameters. Figure 2(b) shows the measured ground electron to heavy-hole state transitions for the investigated samples together with calculated values again including non-parabolicity and interdiffusion. The values of the $E_1 - HH_1$ transitions were determined from the low-temperature photoluminescence using the line-shape analysis of Ref. (246). The simultaneous fit of both the intersubband absorption and the low-temperature photoluminescence is only possible for $\Delta E_c = 370$ meV and an interdiffusion of 1.4 monolayer per heterointerface.

The value of the electron effective mass at the bottom of the conduction band in the quantum wells is taken to be $m_e^*(\text{well}) = 0.060 m_0$ based on magnetoluminescence (210). This value is also consistent with the measured value in strained $\mathrm{In_{0.2}Ga_{0.8}As}$ of $0.063 m_0$ (247) extrapolated to $y = 0.32$. The electron effective mass in the barrier material is taken to be $m_e^*(\text{barrier}) = 0.097 m_0$ and the heavy-hole mass was taken as $m_{hh}^* = 0.80 m_0$ in both materials. The fit is rather insensitive to $m_e^*(\text{barrier})$ and $m_{hh}^*$. As noted above, the non-parabolicity of the conduction band was included (84) and the resulting conduction band non-parabolicity parameters are $3.9 \times 10^{-19}\mathrm{m}^2$ in the wells and $1.5 \times 10^{-19}\mathrm{m}^2$ in the barriers. The model calculation allows us to describe the intersubband transition energies in terms of the band alignment, strain- and energy-dependent effective masses, and interdiffusion in this heterojunction system. Thus, we expect to be able to use the same model with the same input parameters to design more complicated structures required for intersubband detectors and emitters.

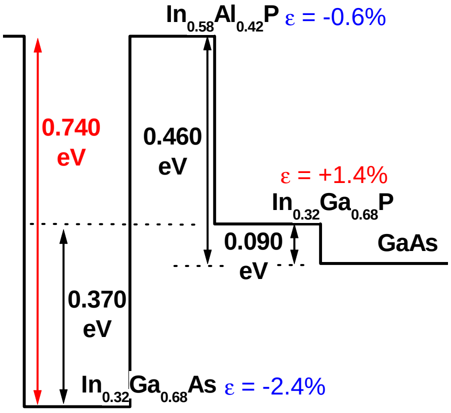

Figure 4.21: Conduction band edge alignment of $In_{0.32}Ga_{0.68}As$, $In_{0.58}Al_{0.42}P$, $In_{0.32}Ga_{0.68}P$, and GaAs.

### 4.3.4 Summary of ISB absorption and CBO study

To summarize, we have grown and studied strain-compensated $In_{0.32}Ga_{0.68}P/In_{0.32}Ga_{0.68}As$ superlattices with a high degree of internal strain, but on average lattice-matched to GaAs. Intersubband transition energies between 100 and 220 meV have been demonstrated in this system. The intersubband absorption along with the low-temperature photoluminescence data are fit using a model incorporating the non-parabolicity of the conduction band, the effects of strain, and As-P interdiffusion. This investigation indicates that the conduction band edge discontinuity is about 370 meV, which is comparable to that of $Al_{0.45}Ga_{0.55}As/GaAs$. The present study provides a set of input parameters for calculating the band structure and emission or absorption energies in similar, but more complicated structures. These data further indicate that this strain-compensated system is an interesting candidate for applications based on intersubband emission or absorption such as quantum cascade lasers or quantum well infrared photodetectors.

Finally fig. 4.21 summarizes obtained CBO results. Given values are obtained with a ±10 meV tolerance.

## 4.4 Intersubband relaxation dynamics in InGaAs-InGaP-InAlP model samples

In previous section we have proposed the strain-compensated $In_{0.32}Ga_{0.68}As$ -$In_{0.32}Ga_{0.68}P$ material system as an interesting GaAs-

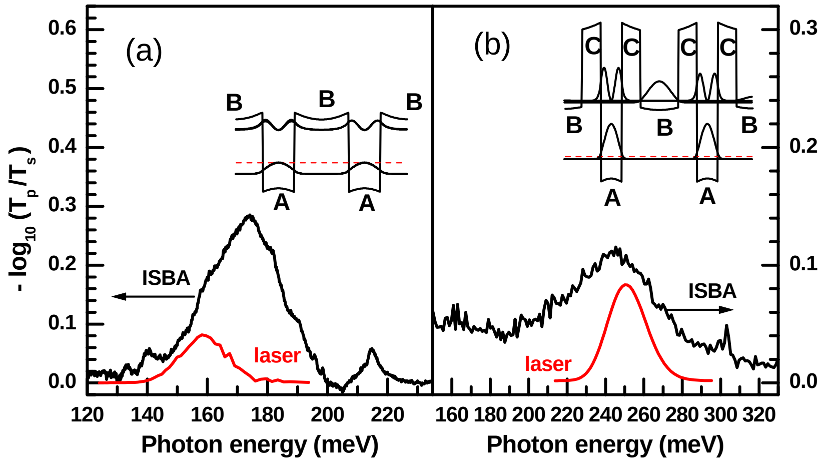

Figure 4.22: Intersubband absorption spectra measured at room temperature for the samples (a) A14 and (b) A33. Insets show the real space conduction band edge profile and confined states wavefunctions. A, B, and C indicate respectively $In_{0.32}Ga_{0.68}As$, $In_{0.32}Ga_{0.68}P$, and $In_{0.58}Al_{0.42}P$. Dotted lines: spectra of femtosecond mid-infrared pulses used in the time-resolved experiments shown in Fig. 2.

based candidate for applications in mid-infrared intersubband emitters and detectors. Its 370-meV conduction band offset (CBO) and effective electron mass of $0.060 \times m_0$ allow engineering of intersubband transitions even slightly shorter than 6 $\mu$m. With an Al-containing barrier, the CBO for the $In_{0.32}Ga_{0.68}As$- $In_{0.58}Al_{0.42}P$ interface can be increased to 700 meV, suggesting the $In_{0.32}Ga_{0.68}As$- $In_{0.32}Ga_{0.68}P$- $In_{0.58}Al_{0.42}P$ three component strain-compensated material system (where all the three are direct band gap materials) on GaAs as a new material for quantum cascade lasers (QCLs) with emission down to 3–4 $\mu$m. In the present section, we investigate the carrier dynamics in this system using femtosecond time-resolved pseudo-two-color pump-probe measurements. The time-resolved data show a complex dynamics governed by stimulated emission from excited subbands, recovery of ground state population, and carrier redistribution within the subbands involved.

## 4.4.1 Experimental details

Figure 4.22 shows the intersubband absorption spectra of samples (a) A14 and (b) A33 together with the spectra of the femtosecond laser pulses, used in pump-probe experiment. Note, that in both cases ISB absorption is broader than the laser spectrum. Thus we do resonantly excite only the part of the carriers within the lower subband (only in a certain $k$-space

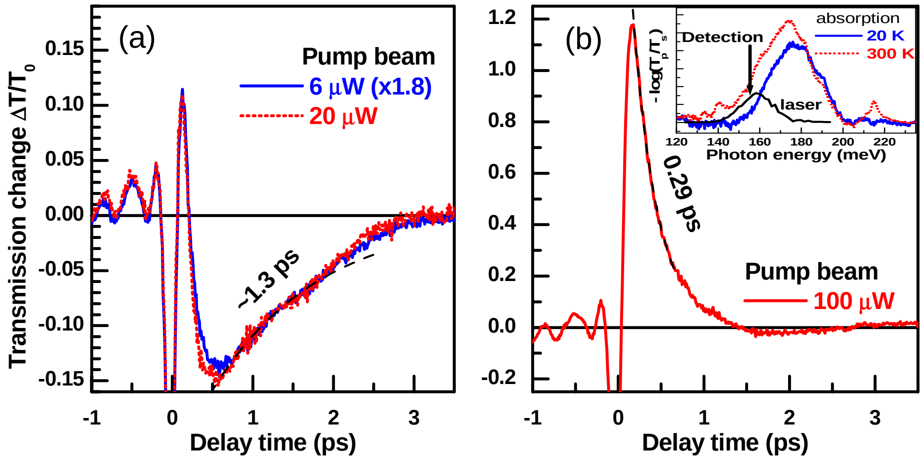

Figure 4.23: Time evolution of the nonlinear transmission changes for sample A14 at $\lambda_{pump} = \lambda_{probe} = \lambda det$= 8.0 $\mu$m. The experiments were performed at room temperature for an excitation power of 6 and 20 $\mu$W (a) and 100 $\mu$W (b).

range). Thus we do not collect a partial information about intersubband dynamics within the single experiment. One should bare it in mind, when giving the interpretation of the following results. Sample A14, a simple InGaAs/InGaP superlattice, consists of 50 periods, each with 5.7 nm $In_{0.32}Ga_{0.68}As$ and 9.8 nm $In_{0.32}Ga_{0.68}P$ (see also table 4.1 for more details). The Al-containing sample A33 consists of 20 periods, each with 4.4 nm $In_{0.32}Ga_{0.68}As$, 3.9 nm $In_{0.58}Al_{0.42}P$, 8.0 nm $In_{0.32}Ga_{0.68}P$, and 3.9 nm $In_{0.58}Al_{0.42}P$. Structure A33 is designed with attempt to couple the first excited electronic state in the InGaAs with the ground electronic state in the InGaP (see insets on Fig. 4.22(b)), similar to designs used in 3-QW QCL active region.

The 250-meV absorption peak for A33 agrees well with the 283 meV calculated with a 700-meV CBO and $0.060\times m_0$ effective mass in the well.

We have performed pseudo-two-color pump-probe experiments (as in Ref. (248)) on both samples for various excitation densities, pump frequencies ($\lambda_{pump} = \lambda_{probe}$), and detection frequencies $\lambda_{det}$.

### 4.4.2 Results

Figure 4.23 (a,b) shows transient normalized transmission change of the probe beam as a function of pump-to-probe beams delay time for sample A14. After interaction with sample the probe beam was spatially separated from the pump beam and spectrally resolved. Afterwards detection was done at $\lambda_{det}$=8.00 $\mu$m (155 meV), which corresponds to the

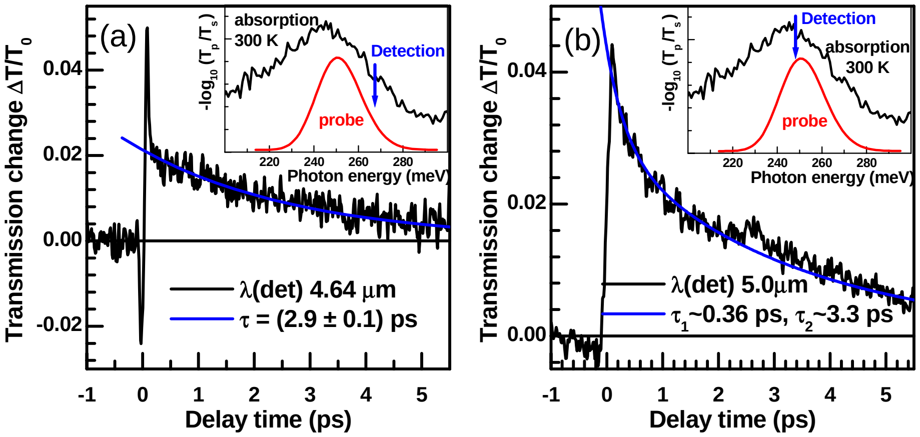

Figure 4.24: Time evolution of the nonlinear transmission changes for sample A33 at (a) $\lambda_{pump} = \lambda_{probe} = \lambda det = 4.64$ $\mu$m and (b) $\lambda_{pump} = \lambda_{probe} = \lambda det = 5.0$ $\mu$m. The experiments were performed at room temperature for an excitation power of 20 $\mu$W.

low energy wing of the room temperature absorption of the sample A14, as indicated on the inset of Fig. 4.23 (b). Transient spectra shown at the (a) and (b) panels are acquired at the different pump beam powers: 6, 20, and 100 $\mu$W. At the low excitation power (6 and 20 $\mu$W, Fig. 4.23 (a)) normalized transition change shows almost the same temporal evolution dominated by induced absorption over the fist 2.5 ps after the pump beam pulse excitation. This induced absorption decays exponentially with the rate of approximately (1.3 ps)$^{-1}$. (High frequency spikes are result of coherent coupling of the pump and probe beams, and has nothing to do with carrier dynamics in the sample.) Only with a high pump pulse excitation power of 100 $\mu$W, Fig. 4.23 (b), we have obtained for the sample A14 a domination of induced transmission (bleaching). It decays exponentially with approximately 0.29 ps time constant.

Figure 4.24 (a,b) shows transient normalized transmission change of the probe beam as a function of pump-to-probe beams delay time for sample A33. After interaction with sample the probe beam was spatially separated from the pump beam and spectrally resolved. Afterwards detection was done at $\lambda_{det}$=4.64 $\mu$m, panel (a) and $\lambda_{det}$=5.0 $\mu$m, panel (b), which corresponds to the high energy wing or the center of the room temperature absorption of the sample A33, as indicated on the insets of Fig. 4.23 (a,b). Transient spectra shown at the (a) and (b) panels are both acquired at the low pump beam power of 20 $\mu$W. In both cases we observe induced transmission of the probe beam. But, when detection is done at the shorter wavelength (4.64 $\mu$m, Fig. 4.24 (a)) the induced

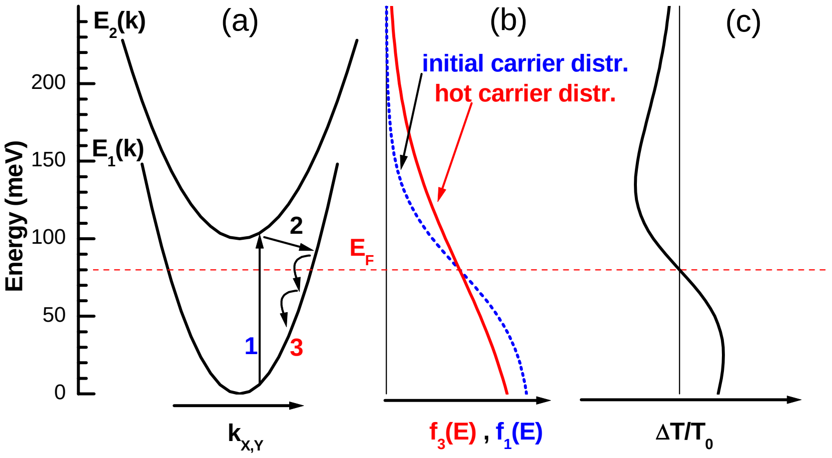

Figure 4.25: (a) Schematic representation of the elemental processes taking place due to the resonant carrier excitation: 1-resonant carrier transfer into the upper subband, 2-intersubband scattering, and 3-intrasubband relaxation. (b) Thermal carrier distribution within the lower subband vs the energy before excitation (dashed line) and after the excitation with subsequent thermalization of electron plasma vie electron-electron interaction (solid line). (c) Correspondent normalized transmission change due to the carrier plasma heating in the lower subband vs the energy

transmission decays monoexponentially with the time constant of approximately 2.9 ps. While detecting at the longer wavelength (5.0 $\mu$m, Fig. 4.24 (b)), we observed biexponential decay of induced transmission. Fit gave us the time constants of approximately 3.3 ps and 0.36 ps.

### 4.4.3 Discussion

Let us now consider the basic transient processes in a two level system. After the ultrafast excitation a portion of electrons from the lower subband $E_1$ undergoes a resonant intersubband transition (1 on the Fig. 4.25 (a)) with a subsequent resonant LO-phonon intersubband scattering (2 on the Fig. 4.25 (a)). Other portion of electrons from the lower subband $E_1$ can undergo an intrasubband transition with emission of the LO-phonon (not indicated on the picture). Fast electron-electron scattering (which dominates at high carrier concentrations) leads to the "hot" thermal distribution of carriers within the subbands, in particular, within the lower subband $E_1$ (solid curve on the Fig. 4.25 (b)). Then electrons do interact with the crystal lattice by the means of electron-LO-phonon scattering, and restore the initial "cold" carrier distribution within (dashed curve

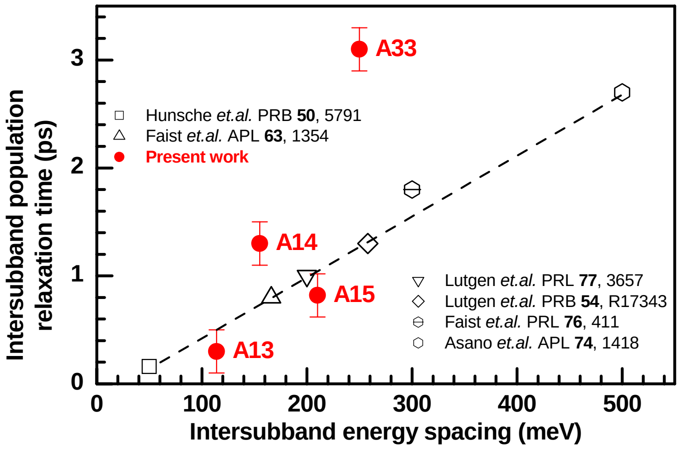

Figure 4.26: Map of intersubband carrier population relaxation (electron plasma "cooling") times obtained on $In_{32}Ga_{68}As$-$In_{32}Ga_{68}P$ samples in present work (solid circles) in comparison to some recent experimental results from literature (hollow symbols) (120; 115; 121; 122; 119) .

on the Fig. 4.25 (b)). Last process is usually refereed as a carrier plasma cooling.

Due to the band nonparabolicity effect (different curvature of the $E_1$ and $E_2$ dispersions) the probe beam of different energies does sense the carriers distribution in different $k$-space locations (lower ISB transition energy corresponds to higher momentum $k$ and vice versa).

Hot carrier distribution (Fig. 4.25 (b)) depletes the low $k$-space region of lower subband, below $k_F$, and populates the high $k$-space region, above $k_F$. Therefore, when probing energy is at the low energy wing of the ISB absorption spectrum (high momentum region) we observe induced absorption. This is the case on Fig. 4.23 (a). When probing energy is at the high energy wing of the ISB absorption spectrum (low momentum region) we observe induced absorption. This is the case on Fig. 4.24 (a). Those were effects, connected with carrier plasma heating and cooling.

Now, depending on particular experimental conditions (say, detection wavelength, excitation power) one can resolve in the transient probe beam transmission the particular scattering event connected with the carrier transfer between the subbands (intersubband scattering). This is the case on the Figs. 4.23 (b) and 4.24 (b). Because it is a single LO-phonon scattering event, intersubband scattering is considerably faster than the overall carrier plasma cooling scenario, consisting of a number of scattering events. Varying the experimental conditions we were able to extract intersubband scattering times for samples A14 and A33 of 0.29 ps and 0.36 ps correspondingly.

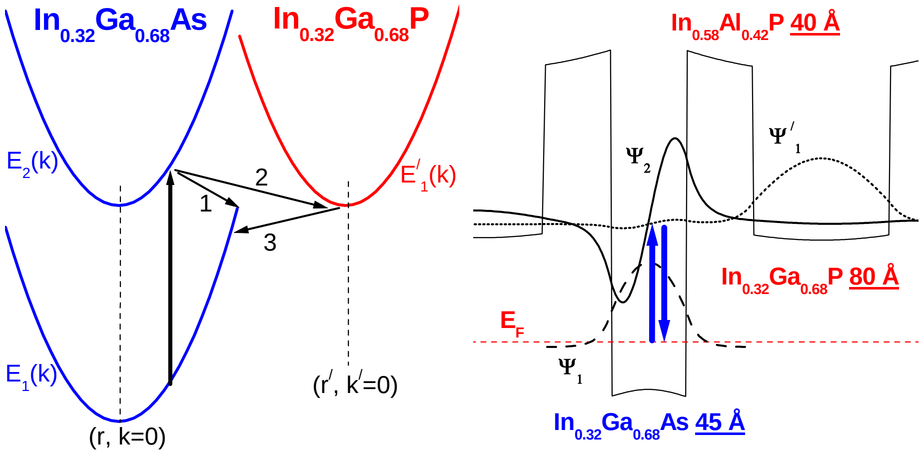

Figure 4.27: Sketch of relevant carrier scattering processes in $k$-space (left hand panel) and real space (right hand panel). Blue arrows are the resonant excitation and intersubband scattering within the InGaAs well. Red arrow represent the real space carrier transfer between the coupled states within InGaAs and InGaP.

Slow transient components on Figs. 4.23 (a) and 4.24 (a,b) are governed with the thermal carrier distribution dynamics and reflect the cooling rate of carrier plasma.

Now, let us consider obtained values of carrier plasma cooling rates, comparing them to some recent literature data on $In_{0.53}Ga_{0.47}As$-$In_{0.52}Al_{0.48}As$ and GaAs- (Al,Ga)As QWs. Strictly speaking, direct comparison of scattering times in our $In_{0.32}Ga_{0.68}As$ QWs is not valid with either $In_{0.53}Ga_{0.47}As$ or GaAs material. But on the other hand, there is no literature data on the same material as we do study here. Beside, the carrier plasma cooling times in both $In_{0.53}Ga_{0.47}As$- $In_{0.52}Al_{0.48}As$ and GaAs- (Al,Ga)As QWs follow a similar trend vs the intersubband energy spacing (115) (see Fig. 4.26, hollow symbols). On Fig. 4.26 (solid circles) we have plot electron plasma cooling times, obtained for samples A13, A14, A15, and A33 at low pump pulse powers. One see, that for SL samples A13-A15 obtained data do fit to the range of literature data for GaAs-(Al,Ga)As and $In_{0.53}Ga_{0.47}As$- $In_{0.52}Al_{0.48}As$ QWs. While the carrier cooling time in multiple double quantum wells (MDQWs) A33 is ≈3 times longer than the literature data obtained for the multiple quantum wells with similar intersubband spacing.

Now we discuss a sharp difference in cooling of carrier plasma in SL samples A13-A15 and in MDQW A33. We can distinguish three parameters, which differ in MDQW and SL designs. First one is different doping level. Second one is different barrier material in SL and MDQW samples. And the third is different spatial overlap of the ground state and excited state wavefunctions.

Different doping level in considered samples can affect the carrier-carrier scattering rates. But the carrier-carrier interaction, however, is an ultrafast process with decays within ≈100 fs time range. So, the doping density variation over the set of our samples should not affect the slow ($\tau \approx 1 - 3$ ps) normalized transmission decays connected with carrier plasma cooling.

A relevant process for carrier plasma cooling is electron-lattice interaction. And the most effective electron-lattice scattering event is scattering of carriers on lattice polarizations due to the longitudinal optical (LO) phonons (so called Fröhlich interaction (249)). Generally speaking, different materials are characterized with different strength of electron-phonon interaction. And thus, different barrier material is of matter. But carriers do reside mostly the well material, which is the same for all the samples considered here. Therefore, the only way, we see, the different barrier material can affect the overall scattering rate of confined carriers is through the introducing the different interface-localized LO phonons (250). The interface phonon potential depends on the step of the dielectric constant on the well/barrier interface and therefore strongly depends on the barrier material choice. The $In_{0.32}Ga_{0.68}As/In_{0.58}Al_{0.42}P$ interface has a higher step of dielectric function then the $In_{0.32}Ga_{0.68}As/In_{0.32}Ga_{0.68}P$ interface. Therefore the impact of the interface phonons on the electron scattering in the $In_{0.32}Ga_{0.68}As$-$In_{0.58}Al_{0.42}P$-$In_{0.32}Ga_{0.68}P$ multiple quantum wells (sample A33) is expected to be higher then in the $In_{0.32}Ga_{0.68}As$-$In_{0.32}Ga_{0.68}P$ superlattices. However, introduction of an additional scattering scenario (i.e. the increased electron–interface-phonon interaction) should lead to the higher overall scattering rates. And thus, introduction of InAlP material itself in sample A33 should lead to the opposite effect of what is observed experimentally.

As one can see from Eqs. 2.87-2.91, the e–LO scattering rate depends on spatial overlap of electron wavefunctions in initial and final states (before and after scattering). Penetration of the wavefunction $\Psi_2$ into $In_{0.32}Ga_{0.68}P$ well (see Fig. 4.27 right hand panel) due to the coupling of states 2 and $1^{/}$, reduces the spatial overlap between $\Psi_2$ and $\Psi_1$, and thus, decreases the scattering rate, $1/\tau_{2,1}$, between state 2 and 1.

In another words, spatial overlap of the ground and excited state functions (and so $1/\tau_{2,1}$) reduces if carrier meets different barriers, when being in ground or excited state. And this happens only in the case of sample A33, but not in other samples. Thus the intersubband population relaxation time in sample A33 is increased comparing the MQW samples, likely, due to the coupling of states 2 and $1^{/}$.

The same effect one can describe in terms of inter-well tunnelling events. In addition to the intersubband scattering "channel" (arrow 1) of the carrier escape from the state 2 (see Fig. 4.27 left hand panel), in A33 there is also possibility to tunnel out the $In_{0.32}Ga_{0.68}As$ well (arrow 2) into $In_{0.32}Ga_{0.68}P$ well and back (arrow 3). Inter-well tunnelling rates depend strongly on coupling of states 2 and $1^{/}$ (see Eqs. 2.87-2.91). Because of relatively thick, 4 nm $In_{0.58}Al_{0.42}P$ barrier it is likely that this process will be significantly slower, than direct intra-well scattering (arrow 1). And thus, the intersubband scattering in the $In_{0.32}Ga_{0.68}As$-$In_{0.58}Al_{0.42}P$-$In_{0.32}Ga_{0.68}P$ multiple quantum wells (sample A33) is slower then the intersubband scattering in the $In_{0.32}Ga_{0.68}As$-$In_{0.32}Ga_{0.68}P$ superlattices.

## 4.5 Design and characterization of InGaAs-InGaP cascade test-structure

### 4.5.1 InGaAs-InGaP/GaAs test-structure

The average barrier-to-well thickness ratio of 1.7 (required for the overall strain compensation) together with relatively small (≈370 meV) CBO make the QCL active region design in $In_{0.32}Ga_{0.68}As$-$In_{0.32}Ga_{0.68}P$ material system quite complicated. On another hand, the As-P cross-contamination during the layer deposition makes it challenging to produce a uniform QCL structure (with typically 300-to-1000 individual layers within the active region.)

As a test-structure, we have grown 35 $In_{0.32}Ga_{0.68}As$-$In_{0.32}Ga_{0.68}P$ chirped-superlattice cascades sandwiched first in between two 250-nm-thick GaAs:Si ($n = 1.5 \times 10^{17}$ cm$^{-3}$) layers, and then between two 2100-nm-thick $In_{0.48}Ga_{0.52}P$:Si ($n = 3 \times 10^{17}$ cm$^{-3}$) cladding layers. Structure was grown on GaAs:Si ($n = 5 \times 10^{18}$ cm$^{-3}$) substrate and capped with 20-nm-thick GaAs:Si ($n = 1 \times 10^{19}$ cm$^{-3}$) contact layer.

Figure 4.28 plots conduction band profile and moduli square of Wannier-Stark wavefunctions within two cascades of $In_{0.32}Ga_{0.68}As$-$In_{0.32}Ga_{0.68}P$ test-structure at 60 kV/cm electric field. Layer thicknesses are adjusted so, that the ground states in active region are aligned into miniband at actual electric field. Thus quick depopulation of state ***1*** is assured via the miniband transport. Presence of a narrow well in active region next to injection barrier displaces slightly states ***1*** and ***3*** in real space. This leads to increase of the carrier lifetime on the upper state ***3***. The only factor which acts against the achievement of the population inversion in the structure is a weak confinement of the upper state ***3***.

States ***3*** and ***1*** are spaced by 211 meV, which agrees well with intersubband absorption data on the superlattices with 4 nm thick $In_{0.32}Ga_{0.68}As$ wells (see section 4.3). Therefore the expected emission

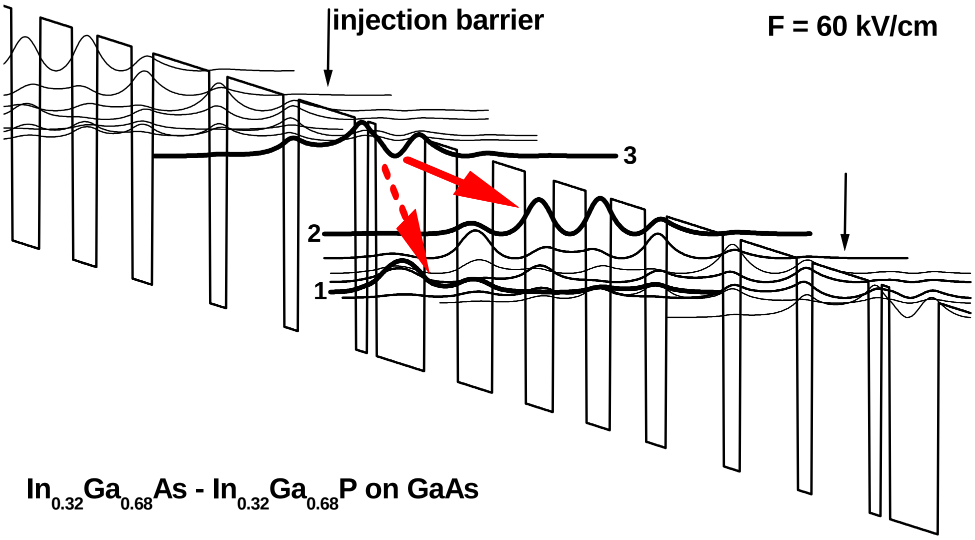

Figure 4.28: Conduction band profile and moduli square of electron wavefunctions of $In_{0.32}Ga_{0.68}As$-$In_{0.32}Ga_{0.68}P$ QC test-structure at 60 kV/cm electric field. The layer thickness in nm from left to right starting from the injection barrier (indicated by vertical arrows) are: **4.7**/1.0/**0.7**/4.0/**2.7**/2.9/**2.7**/2.3/**2.7** /2.0/**2.9**/1.7/**4.7**/1.4/**4.7**/1.2. $In_{0.32}Ga_{0.68}P$ layers are in bold, $In_{0.32}Ga_{0.68}As$ layers are in roman. Underlined layers are doped to $3{\cdot}10^{17}$ $cm^{-3}$. The highest values of dipole matrix element are obtained for 3-to-2 transition (0.147 nm) and for 3-to-1 transition (0.144 nm).

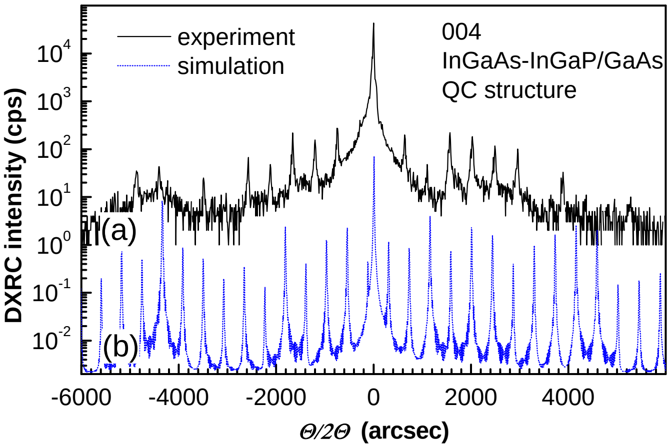

Figure 4.29: 004 reflection experimental DXRC of a 23 periods cascade structure, hub1300, (black solid line). Blue dotted line is a simulated DXRC, assuming absolutely flat heterointerfaces.

wavelength would be in the range of 5.8–6.0 $\mu$m. It has turned out, however, that dipole matrix element for *3*-to-*2* transition is almost the same as one for *3*-to-*1* transition (0.147 nm against 0.144 nm).

On another hand states *1* and *2* might be populated differently. Assuming the thermal energy distribution of the carriers within the injector miniband and a 300 K of the carrier characteristic temperature, one ends up with the ratio of the population of states *1* and *2* equal

$$\frac{f_1}{f_2} = \frac{e^{\frac{E_2 - E_F}{k_B T}} + 1}{e^{\frac{E_1 - E_F}{k_B T}} + 1} \simeq e^{\frac{E_2 - E_1}{k_B T}} \simeq 7. \tag{4.3}$$

Since the state *2* is factor 7 less populated than the state *1*, the *3*-to-*2* transition (121 meV, 10 $\mu$m) should dominate over the *3*-to-*1* transition in emission spectrum.

### 4.5.2 InGaAs-InGaP/GaAs QC-structure characterization

Figure 4.29 shows a DXRC (curve (a)) of a whole $In_{0.32}Ga_{0.68}As$-$In_{0.32}Ga_{0.68}P/GaAs$ cascade structure, grown at 350 °C substrate temperature by GSMBE. Short growth interruptions and other conditions we used as described in section 4.3. Curve (b) is the rocking curve simulation. A series of sharp satellites is an evidence of reproducible 2D growth

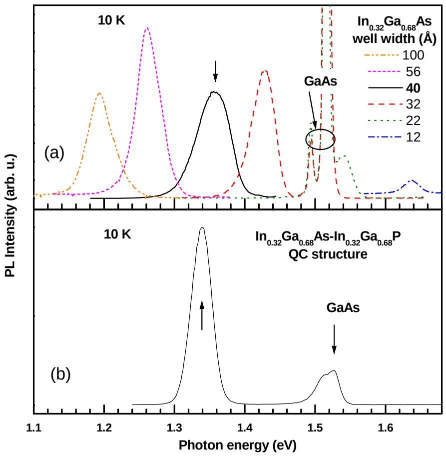

Figure 4.30: 10 K PL (a) from a number of $n$-type $In_{0.32}Ga_{0.68}As$-$In_{0.32}Ga_{0.68}P$ SLs with different $In_{0.32}Ga_{0.68}As$ well thicknesses (as indicated), grown on undoped GaAs substrates; and (b) from a $In_{0.32}Ga_{0.68}As$-$In_{0.32}Ga_{0.68}P$ QC structure, grown on GaAs:Si substrate, $n \approx 1 \cdot 10^{18}$ cm$^{-3}$.

mode through all the 23 cascades of strain-compensated $In_{0.32}Ga_{0.68}As$-$In_{0.32}Ga_{0.68}P$ active region. While damping of high order satellite intensities (as in subsection 4.1.3) indicates some lateral inhomogeneities in the structure.

Figure 4.30 (a) shows a 10 K PL from a number of $n$-type $In_{0.32}Ga_{0.68}As$-$In_{0.32}Ga_{0.68}P$ SLs (see table 4.1) with different $In_{0.32}Ga_{0.68}As$ well thicknesses, grown on GaAs substrates. And figure 4.30 (b) shows a 10 K PL from $In_{0.32}Ga_{0.68}As$-$In_{0.32}Ga_{0.68}P$ QC structure, grown on GaAs:Si substrate doped up to $n = 5 \times 10^{18}$ cm$^{-3}$. Spectral region of PL from the 40 Å $In_{0.32}Ga_{0.68}As$ well almost coincides with those from $In_{0.32}Ga_{0.68}As$-$In_{0.32}Ga_{0.68}P$ QC structure.

Sharp DXRC pattern and narrow, FWHM $\approx$ 20 meV, low temperature PL from $In_{0.32}Ga_{0.68}As$-$In_{0.32}Ga_{0.68}P$ QC structure demonstrate good crystalline and optical quality of grown structure. We should keep in mind, however, that satellite intensity distribution still indicate the presence of interface roughnesses (as analyzed in subsection 4.1.3).

### 4.5.3 Performance of InGaAs-InGaP/GaAs QC-structure

$In_{0.32}Ga_{0.68}As$-$In_{0.32}Ga_{0.68}P$ QC test-structure was processed into the ridges of the width ranging from 10 $\mu$m to 20 $\mu$m. Approximately 2 mm long devices we cleaved and tested under 100ns×5kHz pulsed cur-

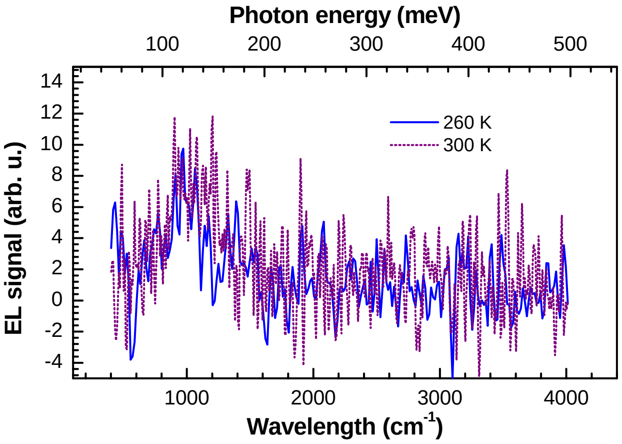

Figure 4.31: Electroluminescence spectra of 35 periods $In_{0.32}Ga_{0.68}As$-$In_{0.32}Ga_{0.68}P$ QC test-structure.

rent drive conditions.

Figure 4.31 presents electroluminescence spectra of 35 periods $In_{0.32}Ga_{0.68}As$-$In_{0.32}Ga_{0.68}P$ QC structure. Spectra are centered at 1050 cm$^{-1}$ (≈130 meV), and are 500 cm$^{-1}$ (≈62 meV) wide. Coherent generation was not achieved with up to 1 A (≈4 kA/cm$^2$ for 10$\mu$m wide ridge) current pulses.

Behind this range of current densities the $I - V$ characteristics (see Fig. 4.32) becomes symmetric in both polarities. Such a behavior occurs, likely, due to a domination of thermionic emission transport in the active region over the miniband transport.

### Discussion

Electroluminescence peaked around 130 meV is, likely, an experimental evidence that *3*-to-*2* transition (see Fig. 4.28) in the active region dominates. Therefore, to expect the shorter intersubband emission (in the range of 6 $\mu$m) one should redesign the structure. Achieving the coherent emission in this material system meats the challenge of proper confining the upper lasing state *3*. Within the $In_{0.32}Ga_{0.68}As$-$In_{0.32}Ga_{0.68}P$ material it is difficult to make due to the small CBO. So, the achieving of a coherent intersubband emission, apparently, requires a modification of the material system itself. Adding a third component (either InAlP or AlGaAs) into the system might add more flexibility to the active region design procedure together with increase of the available CBO.

## 4.6 Summary of chapter 4

To summarize chapter 4, we have

(i) demonstrated high growth quality of a non-standard $In_{0.32}Ga_{0.68}As$- $In_{0.32}Ga_{0.68}P$- $In_{0.58}Al_{0.42}P$ structures strain-compensated on GaAs;

(ii) provided basic study of this material system under post-growth annealing;

(iii) performed a consistent study of material parameters in this system: conduction band offsets, and effective mass;

(iv) demonstrated for the first time short-wavelength intersubband transitions up to 5 $\mu$m in $In_{0.32}Ga_{0.68}As$- $In_{0.32}Ga_{0.68}P$ short period superlattices and $In_{0.32}Ga_{0.68}As$- $In_{0.32}Ga_{0.68}P$- $In_{0.58}Al_{0.42}P$ multiple quantum wells;

(v) performed a study of dynamics of intersubband transitions in $In_{0.32}Ga_{0.68}As$- $In_{0.32}Ga_{0.68}P$ short period superlattices and $In_{0.32}Ga_{0.68}As$- $In_{0.32}Ga_{0.68}P$- $In_{0.58}Al_{0.42}P$ multiple quantum wells;

(vi) proposed QCL design, based on $In_{0.32}Ga_{0.68}As$- $In_{0.32}Ga_{0.68}P$- $In_{0.58}Al_{0.42}P$ material system.

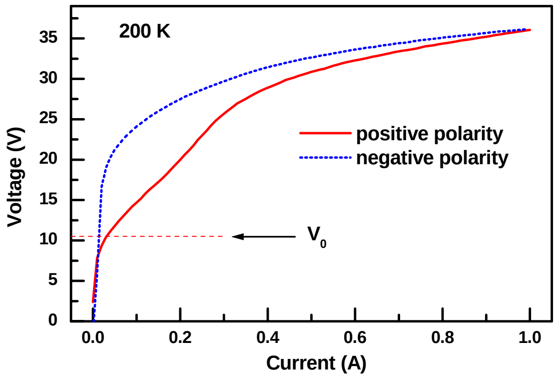

Figure 4.32: Current-voltage characteristics (left panel) and differential resistance at "positive bias" (right panel) of 35 periods $In_{0.32}Ga_{0.68}As$- $In_{0.32}Ga_{0.68}P$ QC test-structure. $V_0$ indicates the calculated "turn-on" bias, which corresponds to 60 kV/cm electric field.

# Chapter 5

# Conclusions

The thesis is devoted to study of novel semiconductor materials (they combination) for the application in short-wavelength 3-5 $\mu$m QCLs. Neither InGaAs-InGaP/GaAs nor InGaAs-AlAs/InP was never implemented in QCLs before the present study. While the InGaAs-AlAs/InP material system is a strain-compensated extension of the generic InGaAs-InAlAs/InP QCL material, the second material system, InGaAs-InGaP/GaAs is a completely novel effort among the family of QCL material systems. Both systems impose a lot of difficulties either on QCL-design faze (because of the lack of reliable material parameters for strained ternary semiconductors) or on QCL realization faze (because of the necessity for QCL layer thicknesses to lay well beyond the critical thickness of coherent epitaxial growth). Therefore, successful realization of QCLs on such a material systems is a physical and technological challenge.

The main results of present research can be naturally split in two parts, and summarized as follows.

On InGaAs-AlAs/InP material system we have

- demonstrated an excellent fabrication of extremely strained InGaAs-AlAs heterostructures on InP;
- carried out a systematic study of short-wavelength intersubband transitions in InGaAs-AlAs/InP material system (i.e. QWs, DQWs, and short period SLs); demonstrated intersubband transitions at the wavelengths as short as 1.74 $\mu$m;
- invented our specific design of QCL active region for InGaAs-AlAs/InP material;
- demonstrated the first experimental implementation of $In_{0.73}Ga_{0.27}As$-AlAs strain-compensated material combination on InP for quantum cascade lasers;

- achieved above room temperature operation for the first time for quantum cascade lasers in 3.5-4.5 $\mu$m spectral range;
- demonstrated for the first time the multi-wavelength QCL operation in 3.9-4.2 $\mu$m spectral range.

On InGaAs-InGaP/GaAs material system we have

- performed the first systematic study and demonstrated the high-performance gas-source MBE fabrication of particular InGaAs-InGaP material combination on GaAs;
- carried out a comprehensive investigation of conduction band offsets on variety of semiconductor heterointerfaces, relevant for InGaAs-InGaP QCL realization (i.e. InGaAs-InGaP, GaAs-InGaP, GaAs-InGaP, and GaAs-InAlP);
- carried out the first experimental study of intersubband transitions in InGaAs-InGaP superlattices on GaAs;
- carried out the first experimental study of intersubband dynamics in InGaAs-InGaP superlattices and InGaAs-InAlAs-InGaAs QWs on GaAs;
- designed, grown, and analyzed InGaAs-InGaP quantum cascade structure.

The experimental research summarized in this thesis is clearly application- and device-oriented. However, behind the spectacular features and performance of studied test-structures and QCLs themselves there is a systematic study of novel semiconductor materials and deep insight into fascinating physics of intersubband transitions in semiconductor heterostructures.

# References

[1] R. F. Kazarinov and R. A. Suris, Sov. Phys. Semicond. **5**, 207 (1971).

[2] J. Faist, F. Capasso, D. L. Sivco, C. Sirtori, A. L. Hutchinson, and A. Y. Cho, Science **264**, 553 (1994).

[3] C. Sirtori, P. Kruck, S. Barbieri, P. Collot, J. Nagle, M. Beck, J. Faist, and U. Oesterle, Appl. Phys. Lett. **73**, 3486 (1998).

[4] K. Ohtani and H. Ohno, Jpn. J. Appl. Phys **41**, L1279 (2002).

[5] J. Faist, F. Capasso, D. L. Sivco, A. L. Hutchinson, S.-N. G. Chu, , and A. Y. Cho, Appl. Phys. Lett. **72**, 680 (1998).

[6] G. Scalari, L. Ajili, J. Faist, H. Beere, E. Linfield, D. Ritchie, and G. Davies, Appl. Phys. Lett. **82**, 3165 (2003).

[7] C. Gauer, J. Scriba, A. Wixforth, J. P. Kotthaus, C. R. Bolognesi, C. Nguyen, B. Brar, and H. Kroemer, Semicond. Sci. Technol. **9**, 1580 (1994).

[8] K. Ohtani and H. Ohno, Appl. Phys. Lett. **82**, 1003 (2003).

[9] C. Becker, I. Prevot, X. Marcadet, B. Vinter, and C. Sirtori, Appl. Phys. Lett. **78**, 1029 (2001).

[10] D. Hofstetter, J. Faist, M. Beck, and U. Oesterle, Appl. Phys. Lett. **75**, 3769 (1999).

[11] D. Hofstetter, J. Faist, M. Beck, A. Müller, and U. Oesterle, Phys. E **7**, 25 (2000).

[12] V. M. Apalkov and T. Chakraborty, Appl. Phys. Lett. **78**, 1820 (2001).

[13] M. P. Semtsiv and W. T. Masselink, “Quantentopfstruktur (Realization of in-plane polarized transitions in quantum-well intersubband devices),” Invention disclosure **DE 103 35 443.3** (31 July, 2003).

[14] F. Bloch, Zeits. f. Physik **52**, 555 (1928).

[15] G. H. Wannier, Phys. Rev. **52**, 191 (1937).

[16] J. C. Slater, Phys. Rev. **76**, 1592 (1949).

[17] J. M. Luttinger and W. Kohn, Phys. Rev. **97**, 869 (1955).

[18] G. Bastard, Phys. Rev. B **24**, 4714 (1981).

[19] G. Bastard, Phys. Rev. B **24**, 5693 (1981).

[20] G. Bastard, Phys. Rev. B **25**, 7584 (1982).

[21] M. Altarelli, in *Heterjunctions and Semiconductor Superlattices*, (eds. G. Allan, G. Bastard, N. Boccora, and M. Voos) (Springer-Verlag, Berlin, 1986).

[22] J. Thomsen, G. T. Einevoll, and P. C. Hemmer, Phys. Rev. B **39**, 12 783 (1989).

[23] R. A. Morrow, Phys. Rev. B **36**, 4836 (1987).

[24] G. Bastard, *Wave Mechanics Applied to Semiconductor Heterostructures* (Halstead Press,, New York, 1988).

[25] C. G. V. de Walle, Phys. Rev. B **39**, 1871 (1989).

[26] J. M. Hinckley and J. Singh, Phys. Rev. B **41**, 2912 (1990).

[27] J. M. Hinckley and J. Singh, Phys. Rev. B **42**, 3546 (1990).

[28] G. L. Bir and G. E. Pikus, *Symmetry and Strain-Induced Effects in Semiconductors* (John Wiley and Sons, New York, 1974).

[29] H. Noguchi, H. Sakaki, T. Takamasu, and N. Miura, Phys. Rev. B **45**, 12 148 (1992).

[30] J. K. Maan, in *Springer Series in Solid State Sciences* (Springer, Berlin, 1984), vol. 53, p. 183.

[31] J. K. Maan, Festkörperprobleme **27**, 137 (1987).

[32] S. J. A. Jr., in *Electronic Properties of Multilayers and Low-Dimensional Semiconductor Structures*, (eds. J. M. Chamberlain, L. Eaves, and J. Portal) (Plenum, New York, 1990), vol. 231 of NATO ASI Series B, p. 117.

[33] Y. C. Chang and R. B. James, Phys. Rev. B **39**, 12 672 (1989).

[34] B. F. Levine, S. D. Gunapala, J. M. Kuo, S. S. Pei, and S. Hui, Appl. Phys. Lett. **59**, 1864 (1991).

[35] R. P. G. Karunasiri, J. S. Park, and K. L. Wang, Appl. Phys. Lett. **61**, 2434 (1992).

[36] S. K. Chun, D. S. Pan, and K. L. Wang, Phys. Rev. B **47**, 15 638 (1993).

[37] K. L. Wang and R. P. G. Karunasiri, in *Semiconductor Quantum Wells and Superlattices for Long-Wavelength Infrared Detectors*, (ed. M. O. Manasreh) (Artech House, Boston, 1993), p. 139.

[38] R. People, J. C. Bean, C. G. Bethea, K. S. Sputz, and L. J. Petricolas, Appl. Phys. Lett. **61**, 1122 (1992).

[39] P. Man and D. S. Pan, Appl. Phys. Lett. **61**, 2799 (1992).

[40] E. R. Brown and S. J. Eglash, Phys. Rev. B **41**, 7559 (1990).

[41] X. Wenlan, Y. Fu, and M. Willander, Phys. Rev. B **48**, 11 477 (1993).

[42] X. Wenlan, M. Willander, and S. C. Shen, Phys. Rev. B **49**, 13 760 (1994).

[43] J. Katz, Y. Zhang, and W. I. Wang, Appl. Phys. Lett. **61**, 1687 (1992).

[44] H. Xie, J. Katz, and W. I. Wang, Appl. Phys. Lett. **61**, 2694 (1992).

[45] C. Lee and K. L. Wang, Appl. Phys. Lett. **60**, 2264 (1994).

[46] J. Khurgin, Appl. Phys. Lett. **62**, 1390 (1993).

[47] E. Gornik and R. A. Höpfel, in *Heterojunctions and Semiconductor Superlattices*, (eds. G. Allan, G. Bastard, N. Boccara, M. Lannoo, and M. Voos) (Springer, Berlin, 1985), p. 84.

[48] M. Cardona (Academic, New York, 1969).

[49] K. H. Seeger, *Semiconductor Physics* (Springer, Berlin, 1985), p. 342.

[50] J. J. Song, P. S. Jung, Y. S. Yoon, H. Chu, Y. Chang, and C. W. Tu, Phys. Rev. B **39**, 5562 (1989).

[51] B. Deveaud, A. Chomette, F. Clérot, A. Regreny, J. C. Maan, R. Romestain, G. B. H. Chu, and Y. Chang, Phys. Rev. B **40**, 5802 (1989).

[52] K. Moore, G. Duggan, A. Raukema, and K. Woodbridge, Phys. Rev. B **42**, 1326 (1990).

[53] K. Fujiwara, K. Kawashima, T. Yamamoto, N. Sano, R. Cingolani, H. T. Grahn, and K. Ploog, Phys. Rev. B **49**, 1809 (1994).

[54] M. Helm, Semicond. Sci. Technol. **10**, 557 (1995).

[55] R. P. G. Karunasiri and K. L. Wang, Superlatt. Microstruct. **4**, 661 (1988).

[56] T. Ando, A. B. Fowler, and F. Stern, Rev. Mod. Phys. **54**, 437 (1982).

[57] W. Bloss, J. Appl. Phys. **66**, 3639 (1989).

[58] M. Zaluzny, Phys. Rev. B **43**, 4511 (1991).

[59] F. Szmulowicz, M. O. Manasreh, C. E. Stutz, and T. Vaughan, Phys. Rev. B **50**, 11 618 (1994).

[60] S. J. Allen, D. C. Tsui, and B. Vinter, Solid State Commun. **20**, 425 (1976).

[61] M. Zaluzny, Appl. Phys. Lett. **60**, 1486 (1992).

[62] R. A. Kaindl, S. Lutgen, M. Woerner, T. Elsaesser, B. Nottelmann, V. M. Axt, T. Kuhn, A. Hase, and H. Künzel, "Ultrafast Dephasing of Coherent Intersubband Polarizations in a Quasi-Two-Dimensional Electron Plasma," Phys. Rev. Lett. **80**, 3575 (1998).

[63] R. A. Kaindl, K. Reimann, M. Woerner, T. Elsaesser, R. Hey, and K. H. Ploog, Phys. Rev. B **63**, 161 308(R) (2001).

[64] T. Elsaesser and M. Woerner, Phys. Rep. **321**, 253 (1999).

[65] U. Ekenberg, Phys. Rev. B **36**, 6152 (1987).

[66] Z. Ikonic, V. Milanovich, D. Tjapkin, and S. Pajevic, Phys. Rev. B **37**, 3097 (1988).

[67] E. B. Dupont, D. Delacourt, D. Papillon, J. P. Schnell, and M. Papuchon, Appl. Phys. Lett. **60**, 2121 (1992).

[68] D. H. Ehlers, Phys. Rev. B **38**, 9706 (1988).

[69] G. D. A. Pinczuk, J. P. Valladares, L. N. Pfeiffer, K. W. West, and C. W. Tu, Phys. Rev. B **39**, 5512 (1989).

[70] A. Pinczuk, S. Schmitt-rink, G. Danan, J. P. Valladares, L. N. Pfeiffer, and K. W. West, Phys. Rev. Lett. **63**, 1633 (1989).

[71] S. L. Chuang, M. S. C. Luo, S. Schmitt-Rink, and A. Pinczuk, Phys. Rev. B **46**, 1897 (1992).

[72] G. Brozak, B. V. Shanabrook, D. Gammon, D. A. Broido, R. Beresford, and W. I. Wang, Phys. Rev. B **45**, 11 399 (1992).

[73] M. S. C. Luo, S. L. Chuang, S. Schmitt-Rink, and A. Pinczuk, Phys. Rev. B **48**, 11 086 (1993).

[74] M. Zaluzny, Phys. Rev. B **49**, 2923 (1994).

[75] V. Anjos, L. Ioriatti, and L. A. O. Nunes, Phys. Rev. B **49**, 7805 (1994).

[76] J. Wagner, Schmitz, F. Fuchs, J. D. Ralston, and P. Koidl, Phys. Rev. B **51**, 9786 (1995).

[77] T. Ando, Solid State Commun. **21**, 133 (1977).

[78] K. M. S. V. Bandara, D. D. Coon, O. Byungsung, Y. F. Lin, and M. H. Francombe, Appl. Phys. Lett. **53**, 1931 (1988).

[79] R. J. Warburton, K. Weilhammer, J. Kotthaus, M. Thomas, and H. Kroemer, Phys. Rev. Lett. **80**, 2185 (1998).

[80] R. J. Warburton, K. Weilhammer, C. Jabs, J. Kotthaus, M. Thomas, and H. Kroemer, Phys. E **7**, 191 (2000).

[81] H. Ehrenreich and M. H. Cohen, Phys. Rev. **115**, 786 (1959).

[82] M. Ramsteiner, J. D. Ralston, P. Koidl, B. Dischler, H. Beibl, J. Wagner, and H. Ennen, J. Appl. Phys. **67**, 3900 (1990).

[83] M. O. Manasreh, F. Szmulowicz, T. Vaughan, K. R. Evans, C. E. Stutz, and D. W. Fischer, Phys. Rev. B **43**, 9996 (1991).

[84] D. F. Nelson, R. C. Miller, and D. A. Kleinman, Phys. Rev. B **35**, 7770 (1987).

[85] M. P. Semtsiv, G. G. Tarasov, W. T. Masselink, H. Kissel, and M. Woerner, Appl. Phys. Lett. **82**, 3418 (2003).

[86] M. Semtsiv, M. Ziegler, S. Dreßler, W. Masselink, N. Georgiev, T. Dekorsy, and M. Helm, Appl. Phys. Lett. **85**, 1478 (2004).

[87] G. Bastard, in *Molecular Beam Epitaxy and Heterostructures*, (eds. L. L. Chang and K. Ploog), Proceedings of the NATO Advanced Study Institute on Molecular Beam Epitaxy and Heterostructures (Nijhoff, Amsterdam, 1983), p. 381.

[88] K. H. Yoo, L. R. Ram-Mohan, and D. F. Nelson, Phys. Rev. B **39**, 12 808 (1989).

[89] R. Q. Yang, J. M. Xu, and M. Sweeny, Phys. Rev. B **50**, 7474 (1994).

[90] L. C. L. Y. Voon, M. Willatzen, and L. R. Ram-Mohan, J. Appl. Phys. **78**, 295 (1995).

[91] M. E. Flatte, P. M. Young, L.-H. Peng, and H. Ehrenreich, Phys. Rev. B **53**, 1963 (1996).

[92] G. Karunasiri, J. S. Park, J. Chen, R. Shih, J. F. Scheihing, and M. A. Dodd, Appl. Phys. Lett. **67**, 2600 (1995).

[93] S. Y. Wang and C. P. Lee, Appl. Phys. Lett. **67**, 2600 (1995).

[94] R. Q. Yang, Appl. Phys. Lett. **66**, 959 (1995).

[95] R. Q. Yang, Phys. E **7**, 220 (2000).

[96] L. Esaki and R. Tsu, IBM J. Res. Develop. **14**, 61 (1970).

[97] K. Leo, P. H. Bolivar, F. Brüggemann, S. Schwedler, and K. Köhler, Solid State Commun. **84**, 943 (1992).

[98] J. Feldmann, K. Leo, J. Shah, D. A. B. Miller, J. E. Cunningham, T. Meier, G. von Plessen, A. Schulze, P. Thomas, and S. Schmitt−Rink, Phys. Rev. B **46**, 7252 (1992).

[99] C. Waschke, H. G. Roskos, R. Schwedler, K. Leo, H. Kurz, and K. Köhler, Phys. Rev. Lett. **70**, 3319 (1993).

[100] A. M. Bouchard and M. Luban, Phys. Rev. B **52**, 5105 (1995).

[101] E. E. Mendez, F. Agullo-Rueda, and J. M. Hong, Phys. Rev. Lett. **60**, 2426 (1988).

[102] A. Sibille, J. F. Palmier, H. Wang, and F. Mollot, Phys. Rev. Lett. **64**, 52 (1990).

[103] H. T. Grahn, K. von Klitzing, K. Ploog, and G. H. Döhler, Phys. Rev. B **43**, 12 094 (1991).

[104] S. Rott, P. Binder, N. Linder, and G. H. Döhler, Phys. Rev. B **59**, 7334 (1999).

[105] A. Wacker, Phys. Rep. **357**, 1 (2002).

[106] M. Saitoh, J. Phys. C: Solid State Phys. **5**, 914 (1972).

[107] M. Saitoh, J. Phys. C: Solid State Phys. **6**, 3255 (1973).

[108] J. Bleuse, G. Bastard, and P. Voisin, Phys. Rev. Lett. **60**, 220 (1988).

[109] G. H. Wannier, Phys. Rev. **117**, 432 (1960).

[110] J. Zak, Phys. Rev. Lett. **20**, 1477 (1968).

[111] P. Voisin, J. Bleuse, C. Bouche, S. Gaillard, C. Alibert, and A. Regreny, Phys. Rev. Lett. **61**, 1639 (1988).

[112] R. Tsu and G. Döhler, Phys. Rev. B **12**, 680 (1975).

[113] S. Rott, N. Linder, and G. H. Döhler, Superlattices Microstruct **21**, 569 (1997).

[114] F. Capasso, K. Mohammed, and A. Y. Cho, Appl. Phys. Lett. **48**, 478 (1986).

[115] T. Asano, S. Noda, and K. Tomoda, Appl. Phys. Lett. **74**, 1418 (1999).

[116] R. Ferreira and G. Bastard, Phys. Rev. B **40**, 1074 (1989).

[117] A. Bonvalet, J. Nagle, V. Berger, A. Migus, J. L. Martin, and M. Joffre, Phys. Rev. Lett. **76**, 4392 (1996).

[118] M. C. Tatham, J. F. Ryan, and C. T. Foxon, Phys. Rev. Lett. **63**, 1637 (1989).

[119] S. Lutgen, R. A. Kaindl, M. Woerner, T. Elsaesser, M. Gulia, D. Meglio, P. Lugli, A. Hase, and H. Künzel, Phys. Rev. Lett. **77**, 3657 (1996).

[120] S. Hunsche, K. Leo, H. Kurz, and K. Köhler, Phys. Rev. B **50**, 5791 (1994).

[121] J. Faist, F. Capasso, C. Sirtori, D. L. Sivco, A. L. Hutchinson, S. N. G. Chu, and A. Y. Cho, Appl. Phys. Lett. **63**, 1354 (1993).

[122] S. Lutgen, R. A. Kaindl, M. Woerner, T. Elsaesser, A. Hase, and H. Künzel, Phys. Rev. B **54**, R17 343 (1996).

[123] C. Gmachl, F. Capasso, A. Tredicucci, D. L. Sivco, A. L. Hutchinson, S. N. G. Chu, and A. Y. Cho, Appl. Phys. Lett. **73**, 3830 (1998).

[124] D. Hofstetter, M. Beck, T. Aellen, and J. Faist, Appl. Phys. Lett. **78**, 396 (2001).

[125] J. Faist, F. Capasso, C. Sirtori, D. L. Sivco, A. L. Hutchinson, and A. Y. Cho, Appl. Phys. Lett. **66**, 538 (1995).

[126] J. Faist, F. Capasso, C. Sirtori, D. L. Sivco, A. L. Hutchinson, and A. Y. Cho, Appl. Phys. Lett. **67**, 3057 (1995).

[127] J. Faist, F. Capasso, C. Sirtori, D. L. Sivco, A. L. Hutchinson, M. S. Hybertsen, and A. Y. Cho, Phys. Rev. Lett. **76**, 411 (1996).

[128] J. Faist, F. Capasso, C. Sirtori, D. L. Sivco, J. N. Baillargeon, A. L. Hutchinson, S.-N. G. Chu, and A. Y. Cho, Appl. Phys. Lett. **68**, 3680 (1996).

[129] M. Beck, D. Hofstetter, T. Aellen, J. Faist, U. Oesterle, M. Ilegems, E. Gini, and H. Melchior, Science **295**, 301 (2002).

[130] C. Sirtori, J. Faist, F. Capasso, D. L. Sivco, A. L. Hutchinson, S. N. G. Chu, , and A. Y. Cho, Appl. Phys. Lett. **68**, 1745 (1996).

[131] D. Hofstetter, M. Beck, T. Aellen, J. Faist, U. Oesterle, M. Ilegems, E. Gini, and H. Melchior, Appl. Phys. Lett. **78**, 1964 (2001).

[132] F. Capasso, J. Faist, C. Sirtori, and A. Y. Cho, Sol. State Commun. **102**, 231 (1997).

[133] J. Faist, M. Beck, T. Aellen, and E. Gini, Appl. Phys. Lett. **78**, 147 (2001).

[134] J. Faist, F. Capasso, C. Sirtori, D. L. Sivco, A. L. Hutchinson, and A. Y. Cho, Nature **387**, 777 (1997).

[135] G. Scamarcio, F. Capasso, C. Sirtori, J. Faist, A. L. Hutchinson, D. L. Sivco, and A. Y. Cho, Science **276**, 773 (1997).

[136] A. Tredicucci, F. Capasso, C. Gmachl, D. L. Sivco, A. L. Hutchinson, and A. Y. Cho, IEEE Photonics Technol. Lett. **12**, 260 (2000).

[137] G. Scamarcio, M. Troccoli, F. Capasso, A. L. Hutchinson, D. L. Sivco, and A. Y. Cho, Electron. Lett. **37**, 295 (2001).

[138] G. Strasser, S. Gianordoli, L. Hvozdara, W. Schrenk, K. Unterrainer, and E. Gornik, Appl. Phys. Lett. **75**, 1345 (1999).

[139] A. Tredicucci, F. Capasso, C. Gmachl, D. L. Sivco, A. L. Hutchinson, and A. Y. Cho, Appl. Phys. Lett. **73**, 2101 (1998).

[140] C. Becker, C. Sirtori, H. Page, G. Glastre, V. Ortiz, X. Marcadet, M. Stellmacher, and J. Nagle, Appl. Phys. Lett. **77**, 463 (2000).

[141] J. Faist, D. Hofstetter, M. Beck, T. Aellen, M. Rochat, and S. Blaser, IEEE J. Quantum. Electron. **38**, 533 (2002).

[142] A. A. Grinberg and S. Luryi, Phys. Rev. Lett. **65**, 1251 (1990).

[143] A. S. Vengurlekar, F. Capasso, A. L. Hutchinson, and W. T. Tsang, Appl. Phys. Lett. **56**, 262 (1990).

[144] F. Capasso, C. Sirtori, J. Faist, D. L. Sivco, S.-N. G. Chu, and A. Y. Cho, Nature **358**, 565 (1992).

[145] C. Sirtori, J. Faist, F. Capasso, D. L. Sivco, and A. Y. Cho, Appl. Phys. Lett. **62**, 1931 (1993).

[146] M. Zahler, I. Brener, G. Lenz, J. Salzman, E. Cohen, and L. Pfeiffer, Appl. Phys. Lett. **61**, 949 (1992).

[147] M. Giehler, R. Hey, H. Kostial, S. Cronenberg, T. Ohtsuka, L. Schrottke, , and H. T. Grahn, Appl. Phys. Lett. **82**, 671 (2003).

[148] J. Faist, F. Capasso, D. L. Sivco, A. L. Hutchinson, C. Sirtori, S. N. G. Chu, and A. Y. Cho, Appl. Phys. Lett. **65**, 2901 (1994).

[149] Y. Hirayama, J. H. Smet, L. H. Peng, C. G. Fonstad, and E. P. Ippen, Appl. Phys. Lett. **63**, 1663 (1993).

[150] J. H. Smet, L. H. Peng, Y. Hirayama, and C. G. Fonstad, Appl. Phys. Lett. **64**, 986 (1994).

[151] K. T. Lai, M. Missous, R. Gupta, and S. K. Haywood, J. Appl. Phys. **93**, 6065 (2003).

[152] S. Izumi, Y. Kouji, N. Hayafuji, and K. Sato, J. Cryst. Growth **201/202**, 8 (1999), and references therein.

[153] C. H. Yan and C. W. Tu, J. Cryst. Growth **164**, 276 (1996).

[154] T. Anan, S. Sugou, K. Nishi, and T. lchihashi, Appl. Phys. Lett. **63**, 1047 (1993).

[155] J.-S. Liu, J.-S. Wang, K. Y. Hsieh, and H.-H. Lin, J. Cryst. Growth **206**, 15 (1999).

[156] K. Y. Cheng, A. Y. Cho, W. R. Wagner, and W. A. Bonner, J. Appl. Phys. **52**, 1015 (1981).

[157] A. Cho, D. Sivco, H. Ng, C. Gmachl, A. Tredicucci, A. Hutchinson, S. Chu, and F. Capasso, J. Cryst. Growth **227-228**, 1 (2001).

[158] N. Georgiev, T. Dekorsy, F. Eichhorn, M. Helm, M. Semtsiv, and W. Masselink, Appl. Phys. Lett. **83**, 210 (2003).

[159] E. Tournie, O. Brandt, and K. H. Ploog, Appl. Phys. Lett. **60**, 2877 (1992).

[160] E. Tournie and K. H. Ploog, Appl. Phys. Lett. **62**, 858 (1993).

[161] E. Tournie, H.-P. Schönherr, K. H. Ploog, C. Giannini, and L. Tapfer, Appl. Phys. Lett. **61**, 846 (1992).

[162] J. M. Millunchick, R. D. Twesten, D. M. Follstaedt, S. R. Lee, E. D. Jones, Y. Zhang, S. P. Ahrenkiel, and A. Mascarenhas, Appl. Phys. Lett. **70**, 1402 (1997).

[163] J. W. Matthews and A. E. Blakeslee, J. Cryst. Growth **27**, 118 (1974).

[164] G. A. Vawter and D. R. Myers, J. Appl. Phys. **65**, 4769 (1989).

[165] in *Semiconductors and Semimetals*, (eds. H. C. Liu and F. Capasso) (Academic Press, New York, 2000), vol. 62 and 66.

[166] T. Asano, M. Tamura, S. Yoshizawa, and S. Noda, Appl. Phys. Lett. **77**, 19 (2000).

[167] T. Akiyama, N. Georgiev, T. Mozume, A. V. Gopal, and O. Wada, IEEE Photon. Technol. Lett. **14**, 495 (2002).

[168] C. Gmachl, H. M. Ng, S.-N. G. Chu, and A. Y. Cho, Appl. Phys. Lett. **77**, 3722 (2000).

[169] J. D. Heber, C. Gmachl, H. M. Ng, and A. Y. Cho, Appl. Phys. Lett. **81**, 1237 (2002).

[170] N. Iizuka, K. Kaneko, and N. Suzuki, Appl. Phys. Lett. **81**, 1803 (2002).

[171] K. Kishino, A. Kikuchi, H. Kanazawa, and T. Tachibana, Appl. Phys. Lett. **81**, 1234 (2002).

[172] R. Akimoto, K. Akita, F. Sasaki, and T. Hasama, Appl. Phys. Lett. **81**, 2998 (2002).

[173] H. C. Chui, E. L. Martinet, M. M. Fejer, and J. J. S. Harris, Appl. Phys. Lett. **64**, 736 (1994).

[174] B. Sung, H. C. Chui, M. M. Fejer, and J. S. H. Jr., Electron. Lett. **33**, 818 (1997).

[175] J. M. Jancu, V. Pellegrini, R. Colombelli, F. Beltram, B. Mueller, L. Sorba, and A. Franciosi, Appl. Phys. Lett. **73**, 2621 (1998).

[176] T. Asano, S. Noda, T. Abe, and A. Sasaki, J. Appl. Phys. **82**, 3385 (1997).

[177] L. C. L. Y. Voon, M. Willatzen, M. Cardona, and L. R. Ram-Mohan, J. Appl. Phys. **80**, 600 (1996), and references therein.

[178] H. C. Liu, M. Buchanan, and Z. R. Wasilewski, Appl. Phys. Lett. **72**, 1682 (1998), and references therein.

[179] A. Neogi, H. Yoshida, T. Mozume, N. Georgiev, T. Akiyama, and O. Wada, Phys. E **7**, 183 (2000).

[180] A. V. Gopal, H. Yoshida, T. Simoyama, N. Georgiev, T. Mozume, and H. Ishikawa, IEEE J. Quantum Electron. **39**, 299 (1993).

[181] I. Vurgaftman, J. R. Meyer, and L. R. Ram-Mohan, J. Appl. Phys. **89**, 5815 (2001).

[182] V. Drouot, M. Gendry, C. Santinelli, X. Letart, J. Tardy, P. Viktorovitch, G. Holliger, M. Ambri, and M. Pitaval, IEEE Trans. Electron. Dev. **43**, 1326 (1996).

[183] M. Helm, W. Hilber, T. Fromberz, F. M. Peeters, K. Alavi, and R. N. Pathak, PRB **48**, 1601 (1993).

[184] R. J. Warburton, C. Gauer, A. Wixforth, J. P. Kotthaus, B. Brar, and H. Kroemer, Phys. Rev. B **53**, 7903 (1996).

[185] M. Ziegler, Diplomarbeit an der Humboldt-Universität zu Berlin (2004).

[186] C. Gmachl, F. Capasso, D. Sivco, and H. Ng, Rep. Prog. Phys. **64**, 1533 (2001).

[187] S. Dressler, M. P. Semtsiv, W. T. Masselink, J. Böttcher, H. Künzel, M. Giehler, H. T. Grahn, and H. Kostial, in *AKF-Frühjahrstagung Dresden 2003* (Dresden, Germany, 2003), vol. 38 of Verhandl. DPG, p. 195.

[188] S. Dressler, Diplomarbeit an der Humboldt-Universität zu Berlin (2002).

[189] V. B. Gorfinkel and S. Luryi, IEEE J. Quantum. Electron. **32**, 1995 (1996).

[190] H. Willenberg, G. H. Döhler, and J. Faist, Phys. Rev. B **67**, 085 315 (2003).

[191] J. Faist, C. Sirtori, F. Capasso, D. L. Sivco, J. N. Baillargeon, A. L. Hutchinson, and A. Y. Cho, IEEE Photon. Technol. Lett **10**, 1100 (1998).

[192] B. S. Williams, S. Kumar, H. Callebaut, Q. Hu, and J. L. Reno, Appl. Phys. Lett. **83**, 2124 (2003).

[193] R. Köhler, C. Gmachl, A. Tredicucci, F. Capasso, D. L. Sivco, S. N. G. Chu, and A. Y. Cho, Appl. Phys. Lett. **76**, 1092 (2001).

[194] M. R. D. H. M. Beck and J. Faist, Appl. Phys. Lett. **79**, 4271 (2001).

[195] Q. K. Yang, C. Mann, F. Fuchs, R. Kiefer, K. Köhler, N. Rollbühler, H. Schneider, and J. Wagner, Appl. Phys. Lett. **80**, 2048 (2002).

[196] L. R. Wilson, D. A. Carder, M. J. Steer, J. W. Cockburn, M. Hopkinson, C. K. Chia, G. Hill, and R. Airey, Phys. E **13**, 835 (2002).

[197] R. Diniz, J. Smoliner, E. Gornik, U. Meiners, H. Brugger, P. Wisniewski, and T. Suski, Semicond. Sci. Technol. B **8**, 1352 (1993).

[198] A. Müller, M. Beck, J. Faist, U. Oesterle, and M. Ilegems, Appl. Phys. Lett. **75**, 1509 (1999).

[199] G. P. Luo, C. P. H. Q. Le, S. S. Pei, W.-Y. Hwang, B. Ishaug, J. Um, J. N. Baillargeon, and C.-H. Lin, Appl. Phys. Lett. **78**, 2834 (2001).

[200] C. Peng, H. L. Zhang, and H. Q. Le, Appl. Phys. Lett. **83**, 4098 (2003).

[201] B. Ishaug, W.-Y. Hwang, J. Um, B. Guo, H. Lee, and C.-H. Lin, Appl. Phys. Lett. **79**, 1745 (2001).

[202] J. Wagner, C. Mann, M. Rattunde, and G. Weimann, Appl. Phys. A **78**, 505 (2004).

[203] R. Q. Yang, C. J. Hill, B. Yang, and J. K. Liu, Appl. Phys. Lett. **83**, 2109 (2003).

[204] Z. Shi, M. Tacke, A. Lambrecht, and H. Böttner, Appl. Phys. Lett. **66**, 2537 (1995).

[205] B. F. Levine, J. Appl. Phys. **74**, R1 (1993).

[206] G. Strasser, S. Gianordoli, W. Schrenk, E. Gornik, A. Mücklich, and M. Helm, J. Cryst. Growth **227-228**, 197 (2001).

[207] W.-S. Lour, Y.-W. Wu, S.-W. Tan, M.-K. Tsai, and Y.-J. Yang, Appl. Phys. Lett. **80**, 3436 (2002).

[208] H. Page, C. Becker, A. Robertson, G. Glastre, V. Oritz, and C. Sirtori, Appl. Phys. Lett. **78**, 3529 (2001).

[209] L. R. Wilson, J. W. Cockburn, M. J. Steer, D. A. Carder, M. S. Skolnick, M. Hopkinson, and G. Hill, Appl. Phys. Lett. **78**, 413 (2001).

[210] M. P. Semtsiv, O.Bierwagen, W. T. Masselink, and F. Eickemeyer, in *44th Electronic Material Conference 2002* (St. Barbara, USA, 2002).

[211] P. Mounaix, P. Delobelle, X. Mélique, L. Bornier, and D. Lippens, Materials Science and Engineering B **51**, 258 (1998).

[212] S. J. Pearton, Materials Science and Engineering B **44**, 1 (1997).

[213] Y. K. Chen, M. C. Wu, J. M. Kuo, M. A. Chin, and A. M. Sergent, Appl. Phys. Lett. **59**, 2929 (1991).

[214] M. Usami, Y. Matsushima, and Y. Takahashi, J. Cryst. Growth **150**, 1344 (1995).

[215] D. K. S. et al., Appl. Phys. Lett. **69**, 3209 (1996).

[216] M. S. et al., Electron. Lett. **30**, 1410 (1994).

[217] M. F. Whitaker, D. J. Dunstan, M. Missous, and L. Gonzalez, Phys. Stat. Sol. B **198**, 349 (1996).

[218] M., M. L. Fille, B. Gil, J. P. Landesman, and J. C. Garcija, Phys. Rev. B **47**, 6465 (1993).

[219] T. Kobayashi, K. Taira, F. Nakamura, and M. Kawai, J. Appl. Phys. **65**, 4898 (1989).

[220] J. H. Kim and J.-I. Song, Solid-State Electron. **45**, 1571 (2001).

[221] A. Ponchet, A. L. Corre, A. Godefroy, S. Salaün, and A. Poudoulec, J. Cryst. Growth **153**, 71 (1995).

[222] O. Shuler, O. Dehaese, X. Wallart, and F. Mollot, J. Appl. Phys. **84**, 765 (1998).

[223] B. Grandidier, R. Feenstra, C. Silfvenius, and G. Landgren, J. Vac. Sci. Technol. A **17**, 2251 (1999).

[224] H. Kroemer, J. Vac. Sci. Tech. B **1**, 126 (1983).

[225] K. Ouchi and T. Mishima, J. Cryst. Growth **209**, 242 (2000).

[226] C. Cai, M. I. Nathan, and T. H. Lim, Appl. Phys. Lett. **74**, 720 (1999).

[227] T. W. Lee, P. A. Houston, R. Kumar, X. F. Yang, G. Hill, M. Hopkinson, and P. A. Claxton, Appl. Phys. Lett. **60**, 474 (1992).

[228] J. H. Chen, J. R. Sites, I. L. Spain, M. J. Hafich, and G. Y. Robinson, Appl. Phys. Lett. **58**, 744 (1991).

[229] M. O. Watanabe and Y. Ohba, Appl. Phys. Lett. **50**, 906 (1987).

[230] H. A. McKay, H. Chen, R. M. Feenstra, and P. J. Poole, J. Vac. Sci. Technol. B **21**, 18 (2003).

[231] C. Nozaki, Y. Ohba, H. Sugawara, S. Yasuami, and T. Nakanisi, J. Cryst. Growth **93**, 406 (1988).

[232] N. Liu, C. K. Shih, J. Geisz, A. Mascarenhas, and J. M. Olson, Appl. Phys. Lett. **73**, 1979 (1998).

[233] M. Mesrine, J. Massies, E. Vanelle, N. Grandjean, and C. Deparis, Appl. Phys. Lett. **71**, 3552 (1988).

[234] C. Y. Tsai, M. Moser, C. Geng, V. Harle, T. Forner, P. Michler, A. Hangleiter, and F. Scholz, J. Cryst. Growth **145**, 786 (1994).

[235] C. Kittel, *Quantum theory of solids* (Wiley, New York, 1963), p. 298.

[236] S. K. Lyo, E. D. Jones, and J. F. Klem, Phys. Rev. Lett. **61**, 2265 (1988).

[237] Y. I. Mazur, G. G. Tarasov, Z. Y. Zhuchenko, H. Kissel, U. Müller, V. P. Kunets, and W. T. Masselink, Phys. Rev. B **66**, 035 308 (2002).

[238] T. W. Hickmot, P. M. Solomon, R. Fischer, and H. Morkoc, J. Appl. Phys. **57**, 2844 (1985).

[239] S.-H. Wei and A. Zunger, Phys. Rev. B **49**, 14 337 (1994).

[240] J. K. Shurtleff, R. T. Lee, C. M. Fetzer, G. B. Stringfellow, S. Lee, and T. Y. Seong, J. Cryst. Growth **234**, 327 (2002).

[241] Y. Dong, R. Feensra, M. Semtsiv, and W. Masselink, Appl. Phys. Lett. **84**, 227 (2004).

[242] W. T. Masselink, M. Zachau, T. W. Hickmott, and K. Hendrickson, J. Vac. Sci. Technol. B **10**, 966 (1992).

[243] F. Eickemeyer, R. A. Kaindl, M. Woerner, T. Elsaesser, S. Barbieri, P. Kruck, C. Sirtori, and J. Nagle, Appl. Phys. Lett. **76**, 3254 (2000).

[244] S. D. Gunapala, B. F. Levine, R. A. Logan, T. Tanbun-Ek, and D. A. Humphrey, Appl. Phys. Lett. **57**, 1802 (1990).

[245] H. Kirsme, private communication .

[246] S. K. Lyo and E. D. Jones, Phys. Rev. B **38**, 4113 (1988).

[247] G. Hendorfer, M. Seto, H. Ruckser, W. Jantsch, M. Helm, G. Brunthaler, W. Jost, H. Obloh, K. Köhler, and D. J. As, Phys. Rev. B **48**, 2328 (1993).

[248] R. A. Kaindl, M. Wurm, K. Reimann, M. Woerner, T. Elsaesser, C. Miesner, K. Brunner, and G. Abstreiter, Phys. Rev. Lett. **86**, 1122 (2001).

[249] M. Stroscio and M. Dutta, *Phonons in nanostructures* (Cambridge University Press, Cambridge, 2001), p. 271.

[250] F. Compagnone, A. D. Carlo, and P. Lugli, Phys. Rev. B **65**, 125 314 (2002).

# Acknowledgments

Present work was done within the framework of the Forschergruppe FOR 394 "Lichtemitter auf der Basis von Intersubband-Übergängen" funded by Deutche Forschungsgemeinschaft, which support I gratefully acknowledge.

I feel indebted to many people from our scientific team within the Humboldt University, to the colleagues from the Forschergruppe, and to our external collaborators from other institutions, who made significant contribution into success of presented work.

At fist, I would like to thank Prof. W. T. Masselink for opportunity to participate in the work on the particular Forschergruppe project A3 "Spannungskompensierte (In,Ga)As-Strukturen für Lichtemitter auf der Basis von Intersubband- Ubergängen". I am thankful for the experience that he shared with me, for his guiding at all the stages of investigations, and critical reading of the manuscript.

I deeply appreciate the experience that I have acquired from Vasyl Kunets and Dr. F. Hatami in field of the crystal growth. They contribution in my understanding of gas source MBE technique can hardly be overestimated. They also have helped me to ramp up with various characterization techniques of semiconductors, like RHEED, X-ray analysis, so on.

Special thanks to Dr. U. Müller, Dr. H. Kissel, and Dr. L. Schrottke for very fruitful discussions of many optical effects and providing photoluminescence results.

Significant support of my investigations was provided by Mr. A. Klein and Dr. H. Kirmse, who did extensive TEM study of related structures.

I appreciate extremely fruitful cooperation, which was established with Prof. M. Helm, Dr. N. Georgiev, Dr. T. Dekorsy, Dr. M. Wörner, and Dr. Z. Wang in a field of intersubband transitions study in InGaAs/InAlAs and InGaAs/InGaP material systems. Obtained results become to be a valuable experimental part of the present manuscript. It is necessary to mention, that initial idea of exploiting the pseudomorphic AlAs barriers, and relevant sample designs for achieving the short ($\sim 2\mu$m) intersubband absorption belong to Dr. Georgiev.

Quantum cascade laser action was obtained on our samples thanks

to cooperation with Dr. H. Künzel, S. Dressler, Prof. H. Grahn, Dr. H. Kostial, Dr. M. Giehler, and D. T. Ohtsuka, Prof. M. Helm, Dr. N. Georgiev, Dr. T. Dekorsy, M. Ziegler who did help with processing and spectroscopy.

I appreciate the help of Dr. C. Gmachl (Ball Labs for Lucent Tachnologies), who provided the electroluminescence results on our first InP-based laser samples. She also has helped a lot advising different steps in laser design and processing the structures with InP cladding.

I thank to Prof. G. G. Tarasov for helpful discussions, good introduction into many body effects, and critical reading of the manuscript.

I am grateful to Dr. R. M. Feenstra and Dr. Y. Dong for providing an outstanding insight in morphology of (In,Ga)As-(In,Ga)P heterointerfaces by STM measurements.

I am thankful to Dr. A. Kawaharazuka, Dr. M. Ramsteiner, and Dr. H. T. Grahn for the opportunity to measure and fruitful discussions of magnetoluminescence spectra on $In_{0.32}Ga_{0.68}As$-$In_{0.32}Ga_{0.68}P$ superlattices.

Spacial thanks for extended cooperation to Dr. J. Tomm, A. Gerhardt, T. Tran, and Dr. V. Talalajev in a field of time-resolved spectroscopy and infrared FTIR-spectroscopy.

I am thankful to other members of our group in Humboldt University and within the Forschergruppe: Dr. Hoerstel, frau Hermann, Dr. Weinert, G. Müssler, O. Bierwagen, R. Pomränke, M. Ziegler, and J. Dobert, A. Laws, J. Sölle, Dr. R. Hey, Prof. K. Reinman, Mr. K. Biermann, Dr. F. Eickemeier for all kind of help, which I have always got when I needed it, and for a nice friendly working atmosphere.

Very special thanks to Sebastian Dreßler for processing the QCLs, to Mathias Ziegler for the input in the modelling of the QCL active region and FTIR spectroscopy of the QCLs, and to Dr. Uve Müller for the advanced FTIR spectroscopy of the QCLs.

# Publications in conjunction with this thesis

[1] M. P. Semtsiv, G. G. Tarasov, W. T. Masselink, H. Kissel, and M. Woerner, "Midinfrared intersubband absorption in strain-compensated InGaP/InGaAs superlattices on (001) GaAs," Appl. Phys. Lett. **82**, 3418–3420 (2003).

[2] N. Georgiev, T. Dekorsy, F. Eichhorn, M. Helm, M. Semtsiv, and W. Masselink, "Short-wavelength intersubband absorption in strain compensated InGaAs/AlAs quantum well structures grown on InP," Appl. Phys. Lett. **83**, 210–212 (2003).

[3] M. P. Semtsiv and W. T. Masselink, "Quantentopfstruktur (Realization of in-plane polarized transitions in quantum-well intersubband devices)," Invention disclosure **DE 103 35 443.3** (filed 31 July, 2003).

[4] N. Georgiev, M. Semtsiv, T. Dekorsy, F. Eichhorn, A. Bauer, M. Helm, and T. Masselink, "Intersubband transitions in strain compensated $In_xGa_{1-x}As/AlAs$ quantum well structures grown on InP," Inst. Phys. Conf. Ser. **No. 174**, 109–112 (2003).

[5] M. Semtsiv, M. Ziegler, S. Dreßler, W. Masselink, N. Georgiev, T. Dekorsy, and M. Helm, "Above room temperature operation of short wavelength ($\lambda = 3.8\mu$m) strain-compensated $\mathrm{In}_{0.73}\mathrm{Ga}_{0.27}$As-AlAs quantum-cascade laser," Appl. Phys. Lett. **85**, 1478–1480 (2004).

[6] Y. Dong, R. Feensra, M. Semtsiv, and W. Masselink, "Cross-sectional scanning tunneling microscopy and spectroscopy on InGaP/GaAs heterojunctions," Appl. Phys. Lett. **84**, 227–229 (2004).

[7] M. Semtsiv, M. Ziegler, S. Dreßler, W. Masselink, N. Georgiev, T. Dekorsy, and M. Helm, "Quanten-Kaskaden-Laser-Struktur (Intersubband laser for ambient temperature 4 $\mu$m emission)," Invention disclosure **DE 10 2004 009 531.0** (filed 20 February, 2004).

# Conference contributions in conjunction with this thesis

[1] M. P. Semtsiv, N. Georgiev, T. Dekorsy, M. Helm, and W. T. Masselink, "Near infrared intersubband transitions in InGaAs-AlAs-InAlAs double quantum wells," in *7th International Conference on Intersubband Transitions in Quantum Wells, ITQW 2003* (Evolène, Swiss, 2003).

[2] M. P. Semtsiv, Z. Wang, M. Woerner, and W. T. Masselink, "Excited electron lifetime engeneering in InGaAs-InGaP-InAlP/(001)GaAs quantum wells," in *7th International Conference on Intersubband Transitions in Quantum Wells, ITQW 2003* (Evolène, Swiss, 2003).

[3] N. Georgiev, T. Dekorsy, M. Helm, M. P. Semtsiv, W. T. Masselink, K. Biermann, and H. Künzel, "Short-wavelength intrsubband absorption in InP-based material systems," in *7th International Conference on Intersubband Transitions in Quantum Wells, ITQW 2003* (Evolène, Swiss, 2003).

[4] Y. Dong, R. M. Feenstra, M. P. Semtsiv, and W. T. Masselink, "Cross-Sectional Scanning Tunneling Microscopy and Spectroscopy of InGaP/GaAs Heterojunctions," in *45th Electronic Materials Conference 2003* (Salt Lake City, USA, 2003).

[5] R. M. Feenstra, Y. Dong, R. Hey, G. Meyer, K. H. Ploog, M. P. Semtsiv, W. T. Masselink, F. Moresco, and K. Rieder, "Probing potential distributions in semiconductors with the scanning tunneling microscope, Invited Presentation," in *Proceedings of 2002 MRS Fall Meeting* (Boston, USA, 2002), to be printed in MRS Proceedings, Volume 738.

[6] N. Georgiev, M. Semtsiv, T. Dekorsy, F. Eichhorn, A. Bauer, M. Helm, and T. Masselink, "Intersubband transitions in strain compensated $In_xGa_{1-x}As/AlAs$ quantum well structures grown on InP substrates," in *29th International Symposium on Compound Semiconductors, ISCS, Abstracts* (Lausanne, Swiss, 2002).

[7] M. P. Semtsiv, O.Bierwagen, W. T. Masselink, and F. Eickemeyer, "Intersubband and interband optical absorption study of strain-compensated InGaAs-InGaP superlattices grown on GaAs," in *44th Electronic Materials Conference 2002* (St. Barbara, USA, 2002).

[8] M. P. Semtsiv, G. G. Tarasov, H. Kissel, F. Eickemeyer, and W. T. Masselink, "Intersubband and interband optical absorption study of strain-compensated InGaAs-InGaP superlattices grown on GaAs," in *14th Indium Phosphide and Related Materials Conference*, Conference Proceedings (IEEE Catalog 02CH37307) (Stockholm, Sweden, 2002), pp. 529–532, iSBN:0-7803-7320-0.

# Curriculum Vitae

*Surname:* Semtsiv
*Fist name:* Mykhaylo

*Date of Birth:* April 1$^{st}$, 1973
*Place of Birth:* Laskiwtsi, the Ukraine
*Nationality:* Ukrainian

| | |
|---|---|
| 1980-1987 | School №1, Terebovlya, the Ukraine |
| 1987-1990 | Phys.-Math. School-Internat №2, Kyiv, the Ukraine |
| 1990-1995 | Physical department of "Taras Schevchenko" National University, Kyiv, the Ukraine<br>Master thesis: *"Application of optical and $\gamma$-spectrometric methods for determination and identification of radioactive components in soils"*<br>Thesis advisor: Dr. Yu. Kononenko |
| 1996-2000 | Ph.D. student in research group Prof. Ye. F. Venger, Institute of Semiconductor physics, National Academy of Science of Ukraine, Kyiv, the Ukraine |
| 2000-present | Ph.D. student in the group of Prof. W. T. Masselink, Institute für Physik, Humboldt Universität, Berlin, Germany<br>Ph.D. Thesis: *"InGaAs-based strain-compensated intersubband emitters for the mid-infrared spectral range"*<br>Thesis Advisor: Prof. W. T. Masselink |

Belin, ........... 2004 ........................... M. P. Semtsiv

# Selbstständigkeitserklärung

Hiermit erkläre ich, die vorliegende Arbeit selbstständig angefertigt und keine weiteren als die angegebenen Hilfsmittel verwendet zu haben.

Berlin, den 04. Mai 2004 Mykhaylo Semtsiv